Doctorate course in:

"Energy and Environment Engineering Science"

XXXIV° cycle

Thesis Title

# "Novel Catalysts for $CO_2$ and $CH_4$ Valorization/$H_2$ Production Prepared *via* Mechanochemical Synthetic Approach"

Dottorando

Rudy Calligaro

Supervisore

Prof. Alessandro Trovarelli

Co-supervisore

Prof. Marta Boaro

**Anno 2022**

*Non è vera né buona legge quella che non ha per madre la Sofia e per padre l'intelletto razionale.*

Giordano Bruno, Spaccio de la bestia trionfante, 1584.

# Index

# Abstract

Nowadays, anthropogenic global warming and the resulting climate change have become a crucial issue to be addressed, and societies must take some drastic measures to face the tough challenges of the coming years in the most effective way. The most important continental and world institutions finally recognized the importance of concrete actions in short times. The roadmap traced with the "European green new deal" in 2019 is an important step. The Sars-COV 2 pandemic created such a prospect of economic disaster that the European Commission has hasted to define the so called "Next Generation EU" plan containing the principal goals of "green new deal". This put the basis for an encouraging development of a new industrial paradigm based on green technologies for environmental protection and the production of green energy from renewable sources. Catalysis will play a key role in this transformation. The development of novel catalysts obtained with green synthetic techniques and without Platinum Group Materials (PGMs) will be important in order to address an industrial implementation of cheap materials produced without formation of any chemical waste.

The scope of this PhD work was to investigate the use of a novel mild-energy ball milling technique, which gave promising results in previous studies carried out by our research group, for the synthesis of cheap novel catalysts for environmental applications. In particular we studied $Ni/CeO_2$ catalysts for the Dry Reforming of Methane and inverse $CeO_2/CuO$ catalysts for the activation of methane at low temperature. Both materials do not employ PGMs and are attractive from and industrial standpoint,

We have synthesized $Ni/CeO_2$ catalysts by varying parameters such as the nature of the metal precursor and the milling time. Two different hydrated Ni salts were used: $NiCl_2 \cdot 6H_2O$ and $Ni(NO_3)_2 \cdot 6H_2O$ and two different series of catalysts were prepared from each precursor by increasing the milling time. The catalysts were tested in Methane Dry Reforming and characterized by means of XRD, BET, TPR and HRTEM in order to obtain some comprehensive findings which could be, in principle, valid for the synthesis of a wider class of ceria or ceria-based materials with this approach and utilizing low-cost precursors. For the two series of catalysts we found that the best performing catalysts in terms of activity and stability were the ones milled at short milling times (10 minutes), thus establishing that a mild mechanical action is useful to obtain very strong Ce-Ni interactions responsible for increased catalytic activity.

In particular, for the nitrate sample milled for 10 minutes, the HRTEM analysis revealed a rugosity diffused on the surface of the ceria crystallites in which the presence of some sub-nanometric Ni entities was detected. More detailed XPS studies performed on the same materials revealed the presence of a localized interaction between cerium and nickel. The nature of this interaction is related to the formation of localized Ni-O-Ce solid solution-type surface arrangements. The low-to-medium milling times proved optimal for the

creation of such nano-structures. On the other hand a prolongated milling action is responsible for their incorporation in the bulk of the crystallites. This had an effect in the catalytic performance of the long-time milled catalysts, which demonstrated to be less active compared to the ones milled for shorter times.

We also prepared a series of $CeO_2$-CuO milled composites by varying Cerium molar ratio. The purpose of this study was to promote the redox exchange between the surface $Ce^{3+}$ sites of a high surface area ceria and the $Cu^{2+}$ sites of the CuO with the gentle mechanical energy provided by the ball milling technique. The synthesized materials together with a reference analogue material synthesized via impregnation method, were characterized by means of XRD, BET, TPR, in-situ DRIFT and operando NEXAFS. We studied the materials with a multi analytical approach (*in situ*-DRIFT/*operando*-NEXAFS) which helped us in the understanding of the mechanism of methane activation at low temperature. A careful in-situ DRIFT analysis demonstrated that the synthesized composites were able to activate methane at 250°C in contrast to the reference materials.

Through operando-NEXAFS experiments, we showed that this activity was related to the formation of a stable and reversible $Ce^{4+}/Cu^{+}$ couple generated from the mechanical action provided by the synthesis. The analysis of products which was carried out during the operando measurements in a low ceria content sample, identified traces of formaldehyde and methanol. This candidates these materials to be promising catalysts for the partial oxidation of methane to oxygenates. In addition, the reversible and cyclable nature of their redox behavior make them suitable catalysts in other environmental and energy applications such as chemical looping processes. We think that these results might be useful for developing a more general green and easily scalable approach to the preparation of a wide class of mixed-oxides composites with peculiar surface redox properties generated from the controlled use of mechanical energy involved in the milling process,.

In order to promote the surface interaction between ceria and the transition metal we have employed for the above studies samples of commercial high surface area ceria, utilizing the presence of $Ce^{3+}$ sites to promote the redox exchange with Cu/Ni particles. As a part of this study we have also developed an hydrothermal synthetic procedure for the preparation in house of a High Surface Area cerium oxide material. We have obtained ceria supports with a specific surface area of more than 300 $m^2/g$ after calcination at 350°C for 6h and stable at high temperatures (specific surface of 40 $m^2/g$ after calcination at 900°C for 6h). We believe that the chemistry of $CeO_2$ in colloidal suspension form might be at the origin of the formation of very high surface area material. Although we did not investigate with sufficient detail the mechanism of formation of this high surface area ceria, these preliminary studies might offer a good starting point for the development of a synthetic procedure capable to design rare-earth mixed oxides materials with improved surface and thermal resistance properties.

In conclusion, this PhD thesis explored the effect of milling process on the preparation of ceria based catalysts that has been characterized and tested in two different reactions. We found that the mild shear stresses provided by the mechano-synthesis were functional to the creation of metastable arrangements responsible of improved catalytic activity compared to reference materials synthesized via the well-established impregnation method. The formation of these arrangements demonstrated to be favored by low milling times and confined on the surface of the ceria crystallites. This synthetic technique also demonstrated to promote redox exchanges between metal ions of different transition metal oxides, creating active catalytic sites. The characterization presented in this PhD thesis work provided also a few insights useful for the development of robust and environmental friendly catalysts for the above described applications.

# Acknowledgements

I would like to thank Prof. Alessandro Trovarelli and Prof. Marta Boaro for giving me the opportunity to build this important piece of my scientific education. I thank them for having guaranteed me everything I needed, starting from the instrumentation up to the important scientific advices, which have been of fundamental importance for the final quality of this work.

I would like to thank also all the members of the group, in particular my closest colleagues, Dr. Maila Danielis, Dr. Andrea Mussio and Dr. Andrea Felli with whom I shared professional aspects and important moments of lightness.

This work is also the result of the important contributions of Prof. Jordi Llorca from Universidad Politecnica de Catalunya and of Dr. Piero Torelli, Dr. Luca Braglia and Dr. Silvia Mauri from the APE-HE beamline of Elettra Sincrotrone Trieste. The quality of this work would not be the same without their help and assistance.

A particular thanks goes to Silvia Mauri, my life partner, who makes me grow every day as a person and with whom I am proud to have been able to share part of this professional path.

Last but not least, I would like to thank my family and my friends which supported me every time in these three years. Your support was fundamental. Thank you.

# 1. Introduction

## 1.1 Overview

The times in which this thesis has been written (2021) will be remembered as crisis times because of the Sars-Cov 2 pandemic breakthrough and the more and more evident effects of the climate change. These two situations can be associated to an unsustainable model of economic growth that characterized the development of the major world economies. This model started with the Industrial revolutions of XVIII and XIX centuries, and it is based on the combustion of fossil fuels whose most important drawback is represented by the production of $CO_2$, the major greenhouse gas whose levels of emissions followed the same trend of the human population growth.

In the last 30 years, the Intergovernmental Panel on Climate Change (IPCC) produced a series of worrying assessments reports that led to the promulgation of some international agreements such as the Kyoto Protocol and the Paris agreement[1,2]. The latest IPCC report[3] confirmed the necessity of limiting the average world temperature increase to 1.5°C within the next decades and evidenced unambiguously the necessity of rapid actions to hold temperatures at the levels which could manage the most extreme risks since the global mean surface temperature is already 1.1°C above that of the end of 19$^{th}$ century. This difference in the global surface temperature led to a series of macroscopic effects such as unprecedented temperatures, severe flooding, sea level rises, hurricanes and typhoons that influenced the life of many people around the world and it is likely that there could be much worse to come[4].

The abovementioned considerations led to an increase in the population's collective awareness of the need of concrete actions against climate change, with the "Fridays for future" initiative representing a good example of this awareness. The Sars-COV 2 pandemic has created such a prospect of economic disaster that the European Commission quickly set out a road map called 'Next Generation EU', containing the main objectives for the development of a new industrial paradigm based on green technologies for environmental protection and the production of green energy from renewable sources. This implies an important energetic transition in which methane will have an important role since its composition ($CH_4$) allows a cleaner combustion compared to other fossil fuels such as coal and oil which have been protagonists until this time[5,6] by virtue of its higher H:C ratio. In other words, the $CO_2$ emissions produced from a mole of methane combustion are lower with respect to the emission produced per mole of other fossil fuels (Figure 1).

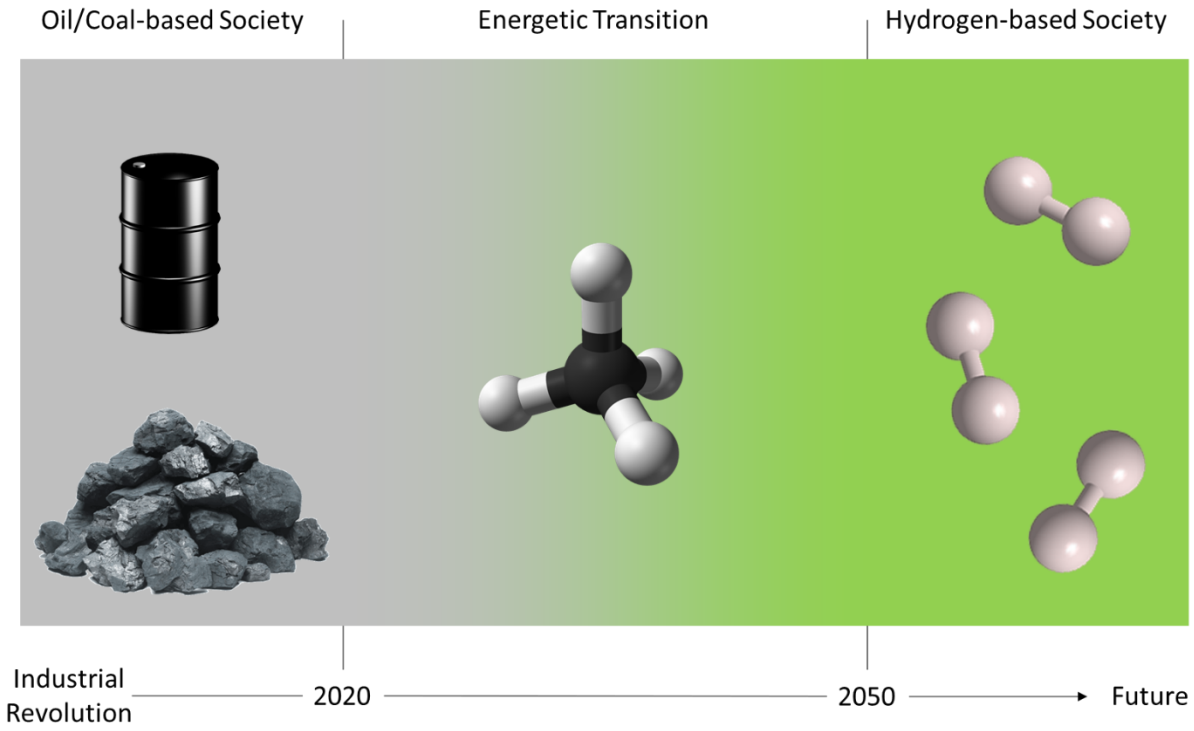


**Figure 1:** Schematic representation of the energetic transition to run in the next decades.

However, $CH_4$ is also a powerful greenhouse gas with a global warming potential ranging between 28 and 36 times higher than $CO_2$ on a 100-year time window[7] and its emissions caused by the processes of extraction and transportation[8,9] represents a huge problem.

For these reasons it is quite clear that in order to reach the goal of keeping the temperature increase around 1.5°C by the half of this century, enormous efforts must be done in the reducing of greenhouse emissions deriving from $CH_4$ and $CO_2$. In order to manage the emissions of these two gases several strategies can be adopted such as the capture, the storage and the reuse as carbon source for the production of higher value chemicals and fuels such as hydrogen through the use of catalytic technologies. Catalysis historically represented a useful technology for environmental purposes[10–12] and, considering the abovementioned statements, will be an important protagonist in the future decades. Much efforts have been conducted in order to develop efficient catalysts[13–17], however the main drawback is represented by the scarce scalability at industrial level of these synthetic methods. Moreover, these methods usually need the use of organic molecules such as solvents and surfactants that need to be managed as waste by products, thus increasing the cost production of the catalytic materials and making them less attractive. In this contest, it is important to study and develop industrial favorable synthetic strategies for the synthesis of highly active catalyst for the valorization of $CH_4$ and $CO_2$ in order to minimize the overall environmental impact of these molecules by transforming them into higher value products and thus favoring a circular economy model.

## 1.2 Cerium Oxide: an evergreen material for energy and environmental processes.

Cerium oxide ($CeO_2$, ceria) is amongst the most studied rare-earth oxides because of its relative abundance[18] and peculiar physical-chemical properties that make this material very interesting in a broad range of applications, ranging from catalytic[10,19] to biomedical[20]. The most relevant and established property of ceria lies in the rapid oxygen release or uptake trough the following reaction, leaving it with extraordinary capability for oxygen storage/release[19,21].

$$CeO_2 \rightleftarrows CeO_{2-x} + x/2\ O_2 \quad \text{Equation 1}$$

The crystal structure (Figure 2) consists of a face-centered unit cell (fcc), where Ce cations are bonded to eight nearest equivalent oxygen atoms, while the O anions are tetrahedrally bonded to four Ce nearest neighbors. In other words, a cubic close packing of cerium (ccp) atoms with oxygen atoms filling the tetrahedral sites[10,19,21].

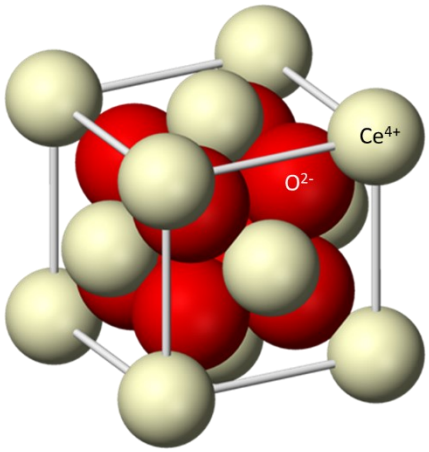


**Figure 2:** fluorite-type crystal structure of $CeO_2$.

The capability of being progressively reduced from $CeO_2$ to $Ce_2O_3$ brings to the formation of oxides with intermediate composition, depending on the oxygen partial pressure[19,21]. The reduction of $CeO_2$ into $CeO_{2-x}$ does not affect the fluorite structure even after the loss of important amounts of oxygen and subsequent formation of oxygen vacancies[22]. The formation of defects in the form of $Ce^{3+}$ sites and oxygen vacancies[19,21] is responsible for the mixed-conductor character of ceria and for its well-known oxygen storage/release properties. This latter property is often evaluated with the Oxygen Storage Capacity (OSC) experiments. A rapid reoxidation of $CeO_{2-x}$ occurs after exposure to oxygen.

The reducible behavior, with the presence of oxygen vacancies, is at the base of the close intimacy, known as Strong Metal-Support Interactions (SMSI), between ceria and numerous supported metal particles[17,19,20]. Strong Metal Support Interactions revealed the pivotal role of the interfaces between metal and support in the enhanced catalytic activity of these systems since they represent the preferential sites for oxygen exchange due to the formation of oxygen vacancies associated with the presence of reduced ceria sites in the vicinity of metal particles[22,17,23,24].

The poor thermal stability of cerium oxide represents an important issue in the total OSC, since the high temperatures cause a growth of the particles and a subsequent loss of surface area which lead to an important reduction of the oxygen storage and release properties[25]. To avoid this problem several strategies can be adopted. One of these is the formation of solid solutions with tetravalent cations such as $Zr^{4+}$, $Hf^{4+}$, $Tb^{4+}$ and $Pr^{4+}$, which, besides improving the thermal stability, cause an improvement of the total OSC compared to that of pure $CeO_2$[22,26,27]. Among these, $CeO_2$-$ZrO_2$ solid solutions are the most used in commercial applications[22].

Concerning pure ceria, an important strategy to improve the formation of oxygen vacancies is the reduction of the particle size at a nanometer scale. At this scale the shape of the crystallites revealed to have an important role on the redox properties of ceria, with nanoshapes such as nanocubes and nanorods which demonstrated to show higher OSC performances compared to spheroidal particles[28,29]. These results have been attributed to the predominant presence of the (100) and (110) surfaces in nanorods and nanocubes[22,30]

The enhanced OSC of these nanoshapes is at the base of the enhanced catalytic performance in several catalytic reactions such as CO oxidation[31], soot combustion[30] and $CO_2$ reforming of methane[32]. From the comparison of catalytic activity in soot combustion of polycrystalline ceria and ceria nanocubes and nanorods, Aneggi et.al.[30] evidenced that, considering the samples in the same range of surface area, the best catalytic results were achieved in the nanoshaped cerium oxides. However, the drop of surface area after thermal aging affected negatively the overall catalytic activity.

Together with the shape of the nanocrystals other geometrical factors such as the particle size and the surface area heavily affect the total OSC of ceria and ceria-based materials[22]. In particular surface area demonstrated to be directly linked with the OSC of ceria and ceria-zirconia[33,34]. By virtue of the enhanced OSC, the utilization of High Surface Area (HSA) oxides demonstrated to be of great importance in the increasing of catalytic activity in a broad range of catalytic reactions[35–37]. There are mainly two reasons at the base of the enhanced activity of HSA supports 1) the above-mentioned abundant presence of surface defects which is linked to the oxygen mobility on the surface and 2) the better dispersion of the supported active

metal catalyst, thus preventing its sintering during the reaction and maximizing the presence of interfacial metal/support sites[38].

In this PhD work we used High Surface Area (HSA) cerium oxide. Recently, Fink et. al.[39] reviewed several synthetic strategies for obtaining HSA ceria, including urea gelation, microemulsion, sol-gel, precipitation, surfactant templating and solvothermal/hydrothermal methods[40–47]. Some of the best results in terms of surface area and thermal stability are reported in Table 1.

**Table 1:** some examples of High Surface Area ceria synthetic approaches from ref. 39.

| Preparation Method | Starting Precursor | Calcination Temperature (°C) | BET Surface Area ($m^2/g$) | Reference |
|---|---|---|---|---|
| Urea Gelation | $(NH_4)_2Ce(NO_3)_6$ | 450 | 215 | 40 |
| Microemulsion | $Ce(NO_3)_3 \cdot 6H_2O$ | 400 | 187 | 41 |
| Alkoxide Sol-Gel | $Ce(OH)_4$ | 400 | 180 | 42 |
| Precipitation | $Ce(NO_3)_3 \cdot 6H_2O$ | 400 | 170 | 43 |
| Precipitation | $(NH_4)_2Ce(NO_3)_6$ | 600 | 200 | 44 |
| Surfactant Templating | $CeCl_3 \cdot 7H_2O$ | 350 | 230 | 45 |
| Solvothermal | $(NH_4)_2Ce(NO_3)_6$ | 500 | 160 | 46 |
| Hydrothermal | $CeCl_3 \cdot 7H_2O$ | Not reported | 211 | 47 |

Among the various reported methods, the ones reported by Bumajdad[41] and Terribile[45] required the use of surfactants which increase the costs of the overall processes, thus making them unattractive from an industrial standpoint. Moreover, keeping in consideration the development of green synthetic techniques based in the reduction of organic solvents and/or molecules in favor of harmless solvents such as water[48], also the urea gelation[40] and alkoxide sol gel methods[42] can result less attractive.

The precipitation method reported by Bruce at.al.[43] is the one which led to the better results, since a specific surface area of 200 $m^2/g$ was achieved after calcination at 600°C for 2h. However, this synthetic procedure demonstrated to be successful starting from diluted solutions of precursor (0.005 to 0.016M), i.e. starting from 1 liter of 0.005M solution of cerium ammonium nitrate they obtained 0.69g of final product. Clearly, these conditions make the reported procedure unfavorable at a higher scale.

From these considerations, the hydrothermal methods result to be the most suitable methods since they represent an easier-to-scale up procedure compared to the other reported above. Moreover, hydrothermal/solvothermal methods have additional important advantages such as the fact of being a single-step low-temperature synthesis which gives highly crystallized nanomaterials thanks to a better control of composition and morphology[49]

The discussed oxygen transport/mobility properties of cerium oxide[19] have a key role in the catalytic applications of this material, whose historical application are represented by Three Way Catalysts (TWCs) and Fluid Catalytic Cracking (FCC)[50–54] .These two processes represented historically the most important commercial catalytic processes in terms of economic relevance and tonnage. Moreover, they represent two examples of cerium oxide applications in the field of energy and environmental engineering. The progressive introduction through the years of more stringent rules in diesel engine emissions required an even larger utilization of ceria based materials since they are among the most studied component in the exhaust emission system of diesel engines[55,56].

Another well established and relevant environmental application of ceria and ceria-based materials is represented by its use in the water purification treatments in which, once again, the role of the surface properties and the oxygen vacancies is pivotal as reviewed by Kurian[57].

As discussed in Section 1.1. of this chapter the climate change action must proceed through the progressive reduction of fossil fuels and through a major utilization of greener energy carriers such as hydrogen, with natural gas ($CH_4$) that surely will have an important role. In the context of this transition, also the reduction/transformation of greenhouse gases such as $CH_4$ and $CO_2$ into higher value products will have a crucial impact. The present and future scenario of energetic transition would likely imply the progessive introduction in the next decades of electric and hybrid engines, with a loss in the market share of traditional internal combustion engines. As a consequence, it is very likely that the auto exhaust catalyst industry will be heavily affected. Nonetheless, while these technologies will progressively become obsolete, ceria and ceria-based materials will continue to be appealing protagonists in the future of energy and environmental transition due to their use in several processes such as methane oxidation[58,59], methane partial oxidation[60–62], $CO_2$ hydrogenation[63–65] and Reforming reactions from hydrocarbons[66,67] and renewable sources such as biomass and alcohols[36,68–70]. Moreover, the transport properties and the electrical conduction of ceria based materials make them interesting for applications as electrolytes in solid oxide fuel cells (SOFC)[71,72] , but also in the emerging fields of photocatalysis, electrocatalysis and phototermocatalysis[73,74].

# 1.3. Methane: ways of valorization

## 1.3.1. Sources of methane and Geopolitical considerations

As pointed out previously, an important prerequisite to implement green technologies lies in the efficient use of nonrenewable sources of hydrocarbons, with methane that represents the election hydrocarbon for the energetic transition because of its cleaner combustion and its abundance in the form of natural gas reserves. Natural gas is a mixture of gaseous hydrocarbons with methane as the main component (>80%) followed by other heavier hydrocarbons such as ethane and propane[75–77]. Natural gas reserves are abundant but they are not located homogenously around the world, with some countries and/or geographic regions that possess the major quantities[78].

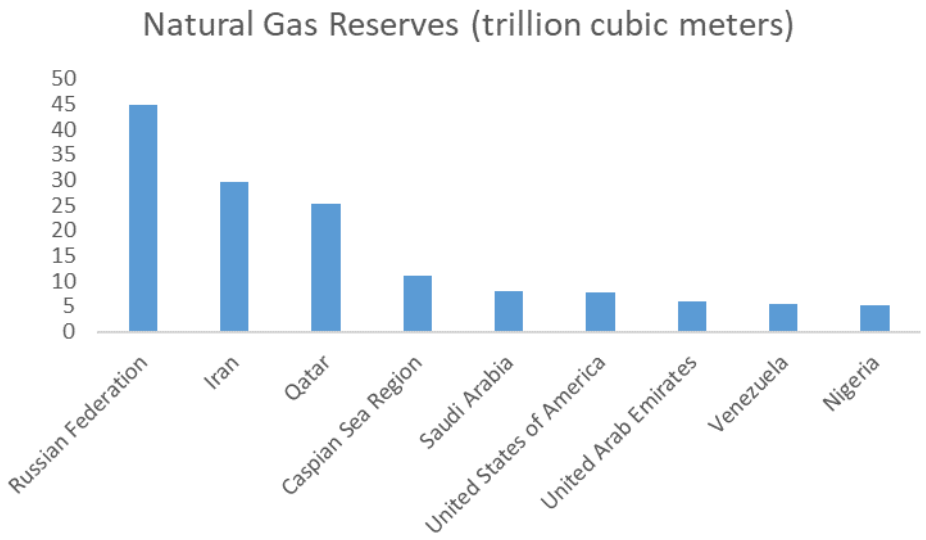


**Figure 3:** Major Natural reserves by country accordingly to ref. 78.

This inhomogeneity made the utilization of natural gas subjected to geopolitical equilibria that are likely to become more delicate in the next years. Thus, an energetic policy more independent from the natural gas is of fundamental importance also from a strategical standpoint. For these reasons, exploring alternative, environmentally benign and energy efficient systems has become the focus of governmental policies, industry, as well as academic research[79–82].

In this sense the biogas originated from the anaerobic digestion of biomasses constitutes an attractive alternative since it represents an established sustainable technology for the simultaneous generation of renewable energy from the treatment of organic wastes[83]. The origin of biomass can be various, some examples are represented by food, animal and agricultural waste[84,85]. The increasing interest of utilizing biogas as substitute to natural gas or its exploitation as transport fuel opened new avenues in the development of biogas upgrading techniques.

The major constituent of biogas is methane whose concentration is in a range of 55-75%, followed by carbon dioxide (25-45%), nitrogen (1-5%) together with traces of impurities such as hydrogen, hydrogen sulfide ($H_2S$) and oxygen whose composition varies from the biogas source (Figure 4).

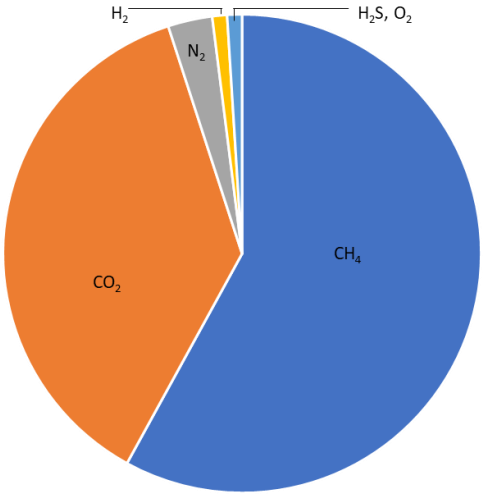


**Figure 4:** typical biogas composition from Ref. 85.

The EU made important efforts on the production of energy from biomasses[86,87] and further efforts must be made in order to achieve an efficient energetic transition and a major independence from fossil fuel imports from other countries.

## 1.3.2 Reforming Processes

Oil, coal, natural gas, and electrolysis are four chief sources for hydrogen production, which account for 30%, 18%, 48%, and 4% of the world's hydrogen production, respectively. With the depletion of coal and oil, methane will represent the main source of industrially produced hydrogen[88]. The reforming processes are thermochemical technologies of transformation of methane which entails the use of thermal energy and catalytic materials for the conversion of methane to various products.

Reforming of hydrocarbons are interesting and established processes for the production of syngas, a mixture of hydrogen and carbon monoxide, which can be exploited for the synthesis of methanol, Fisher-Tropsch fuels and other valuable chemicals or it can be used directly for the feeding of a Solid Oxide Fuel Cell (SOFC)[89–91]. The two components of syngas can be separated, thus obtaining clean hydrogen and carbon monoxide which is an important building block for the synthesis of a wide class of chemicals[92,93]. Methane reforming can be carried out using different oxidant agents such as steam, carbon dioxide and oxygen.

The most important reforming processes is the Steam Reforming of Methane (SRM, Eq. 2), which represents the most established process at the industrial level for hydrogen production since 4 moles of hydrogen can be produced from 1 mole of methane if the produced CO is transformed into $H_2$ and $CO_2$ with the Water Gas Shift reaction (Eq.3)[67,94,95].

$$CH_4 + H_2O \rightarrow 3H_2 + CO \quad (\Delta H^0_{298K} = 206 \text{ kJ/mol}) \quad \text{Equation 2}$$

$$CO + H_2O \rightarrow H_2 + CO_2 \quad (\Delta H^0_{298K} = -41 \text{ kJ/mol}) \quad \text{Equation 3}$$

---

$$CH_4 + 2H_2O \rightarrow 4H_2 + CO_2 \quad \text{Equation 4}$$

Despite its lower cost of production, the grey hydrogen produced *via* SRM can be upgraded to blue hydrogen by capturing of the emitted $CO_2$ [96] and affecting negatively the production costs. Moreover, the overall cost of production will be linked to the natural gas price which is, in the present days, constantly increasing. For these reasons, other emerging reforming technologies using carbon dioxide and oxygen as oxidants are receiving attention due to their perceived advantages over the well-established steam methane reforming. One of such advantages is the prospect of the Dry Reforming of Methane (DRM) to help mitigate greenhouse

gases through the simultaneous utilization of methane and carbon dioxide (Eq. 5). Besides, it is a potential technological route for producing syngas used as chemical intermediates for Fischer Tropsch synthesis.

$$CH_4 + CO_2 \rightarrow 2H_2 + 2CO \quad (\Delta H^0_{298K} = 247\ kJ/mol) \quad \text{Equation 5}$$

While SRM depends mainly from fossil sources (methane from natural gas), DRM can be performed from renewable sources, that is biogas. In this sense DRM represents a more virtuous process since it allows the production of green hydrogen, contrarily to the gray hydrogen produced from SRM[97–99] (Figure 5).

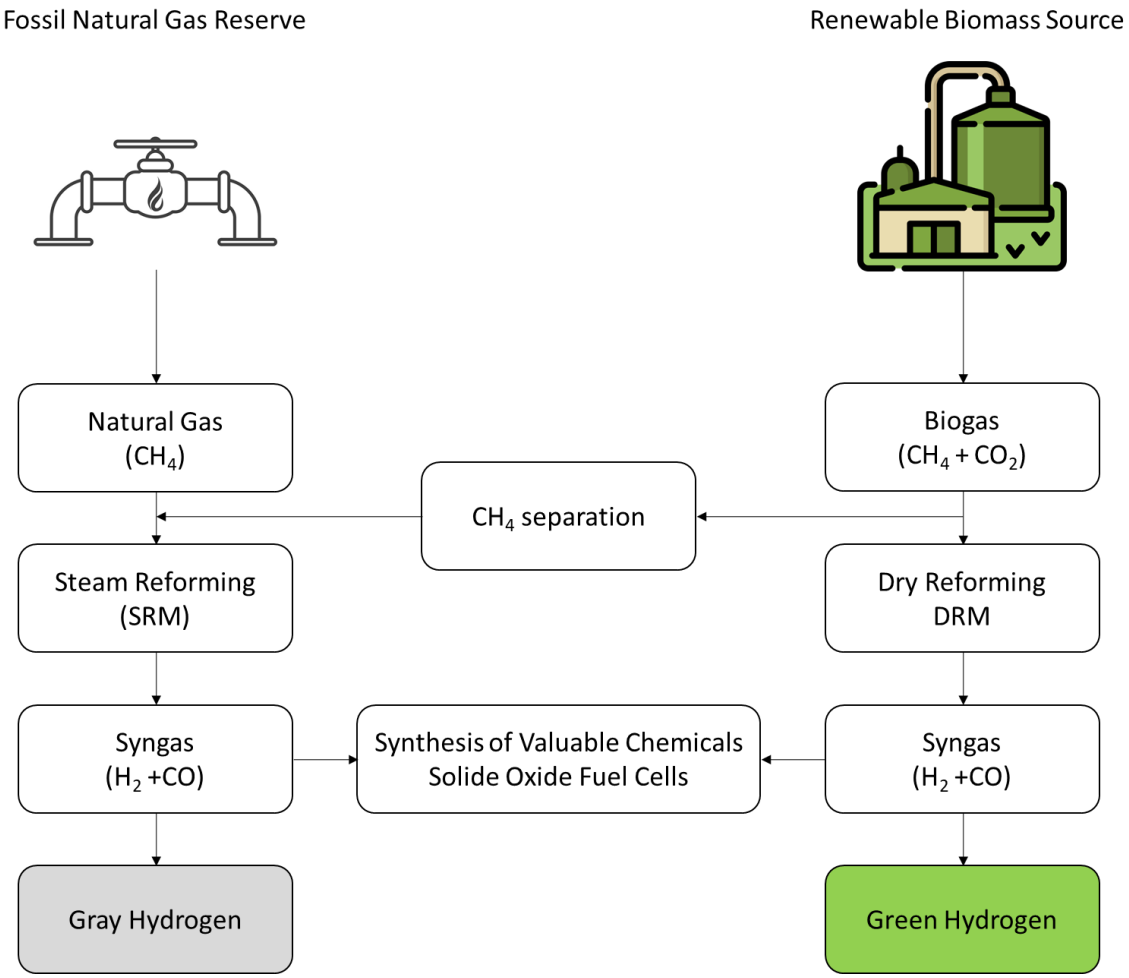


**Figure 5:** schematic representation of the reforming processes starting from different methane sources.

Like SRM, DRM presents some drawbacks due to the high temperatures required[100] which can cause the sintering of the active phase of the catalysts and the occurrence of several parallel reactions such as the reverse water gas shift (RWGS, Eq. 6), methane cracking (Eq. 7) and the Boudouard reaction (Eq. 8).

$$CO_2 + H_2 \rightarrow CO + H_2O \quad (\Delta H^0_{298K} = 41 \text{ kJ/mol}) \quad \text{Equation 6}$$

$$CH_4 \rightarrow C + H_2 \quad (\Delta H^0_{298K} = 171 \text{ kJ/mol}) \quad \text{Equation 7}$$

$$2CO \rightarrow C + CO_2 \quad (\Delta H^0_{298K} = 75 \text{ kJ/mol}) \quad \text{Equation 8}$$

While RWGS affects the overall $H_2$/CO ratio, Eq. 7 and 8 have the major drawback of producing solid carbon which deactivates the catalysts. For these reasons DRM is not considered an industrially mature process[101]; hence, research focused its attention on the development of catalysts capable to overcome these drawbacks. Several catalysts have been developed for reforming reactions and nickel supported catalysts are amongst the most promising candidates because nickel, contrarily to other noble metals[102], is an economic and a relatively abundant element which has a good activity in DRM[103,104], although it is not immune to deactivation[105–107]. To avoid this drawback the choice of the support is of great importance and several oxides have been investigated[108]. Cerium oxide and ceria based materials revealed to be very promising candidates thanks to the peculiar oxygen transfer properties, useful in order to limit the carbon buildup, thus improving stability[36,100,109,110].

## 1.3.3. Low temperature methane activation.

Many efforts have been done to find new strategies for methane valorization[111,112]. Methane activation under mild conditions represents one of the most challenging reactions that the catalysis community faces nowadays. For decades, the production of small carbon based molecules followed a top-down approach starting from long oil molecules. Since oil will be gradually phased out, a change of paradigm is needed in this sector, and the use of small molecules containing carbon as building blocks, thus a transition trough a bottom-up approach, needs the formulation of novel catalysts for this purpose[111].

In current industrial practices, various chemicals have already been produced from methane via the synthesis of syngas(CO/H2) through the reforming processes described in the last paragraphs, followed by additional reaction processes[113,114]. However, the high energy requirements and the multistep reactions, are disadvantages that need to be addressed. Direct conversion of methane, by contrast, is a promising alternative and has already gained much interest[115,116].

Considering the potential of methane as building block for the synthesis of valuable chemicals, its transformation into more useful products is of pivotal importance and its activation still represents the "Holy Grail" from a catalytic standpoint[117,118]. The reason of this challenging activation lies on the extreme stability of this appealing molecule due to its high stability, symmetry and the absence of polarized bonds or functionalities that could allow a chemical reaction. Moreover, this challenge is also related to the molecular orbital configuration of methane, with the low energy Highest Occupied Molecular Orbital (HOMO) and the high energy of the Lowest Unoccupied Molecular Orbital (LUMO) (Figure 6), which make methane rather inert towards the most common organic chemistry strategies of functionalization[111].

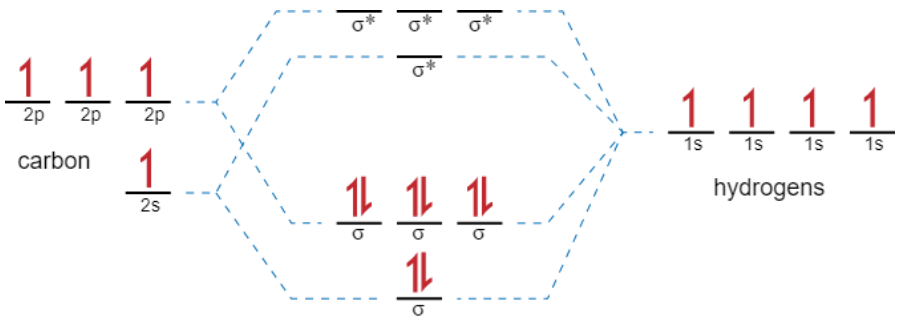


**Figure 6:** Molecular orbitals of methane.

These characteristics made the dissociation of the C-H bond, which is a fundamental prerequisite for the direct conversion of methane into value added products, very difficult due to the high dissociation energy (435 kJ/mol). However, the activation of the C-H bond does not represent the only obstacle for methane functionalization. In fact, also the activation of the oxidant species is a key step for the completion of the catalytic site (Figure 7).

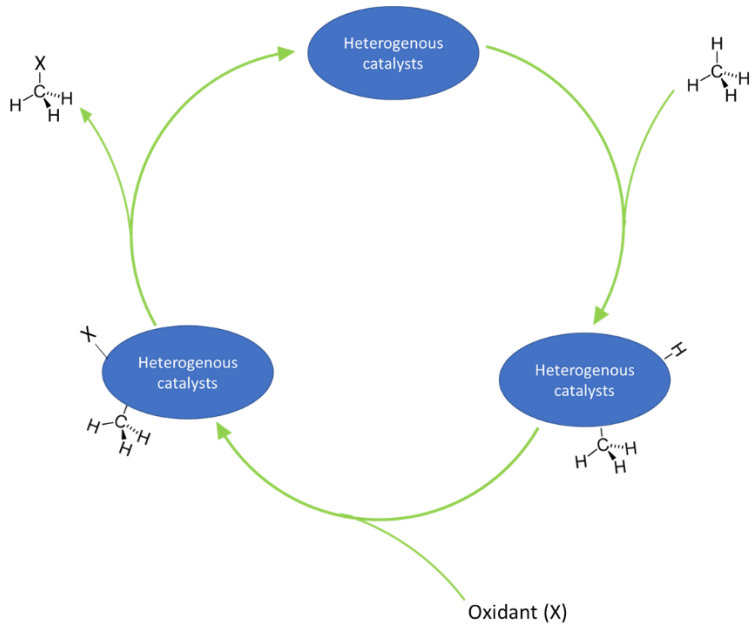


**Figure 7:** Schematic representation of the main steps of the Catalytic Cycle for Methane Functionalization.

Many efforts have been made in order to understand the mechanism of the C-H bonds cleveage[119,120]. Two types of mechanisms have been proposed and the difference between these two mechanisms lies on the atom in which methane is activated. In the so called "true activation" the cleavage of the C-H bond is promoted through the direct interaction with the metal at the catalytic site, with the formation of a metal-carbon bond[111]. The other proposed mechanism is the so called "Fake Activation" in which the activation occurs via interaction with the surrounding basic ligands of a metal center, which, in the case of metal oxides, are represented by the oxygen atoms of the surface of a heterogenous catalyst. These oxygen atoms are responsible for the hydrogen atom abstraction from methane, resulting in its activation and on the formation of a methyl radical[111,121]. This mechanism based on electrophilic oxygens have been observed in several homogenous, heterogenous and enzymatic catalytic systems[111] dedicated to methane partial oxidation. Because of the abundance of Fe-based enzymes for the hydroxylation reaction many efforts have been made

on Fe-base catalysts[122,123]. However, there are no reasons for not extending the research to other late 3d transition metals such as copper, which seems to have a pivotal role in the particulate Methane Mono Oxygenase enzymes[124,125].

Figure 8 summarizes the discussed strategies for methane valorization.

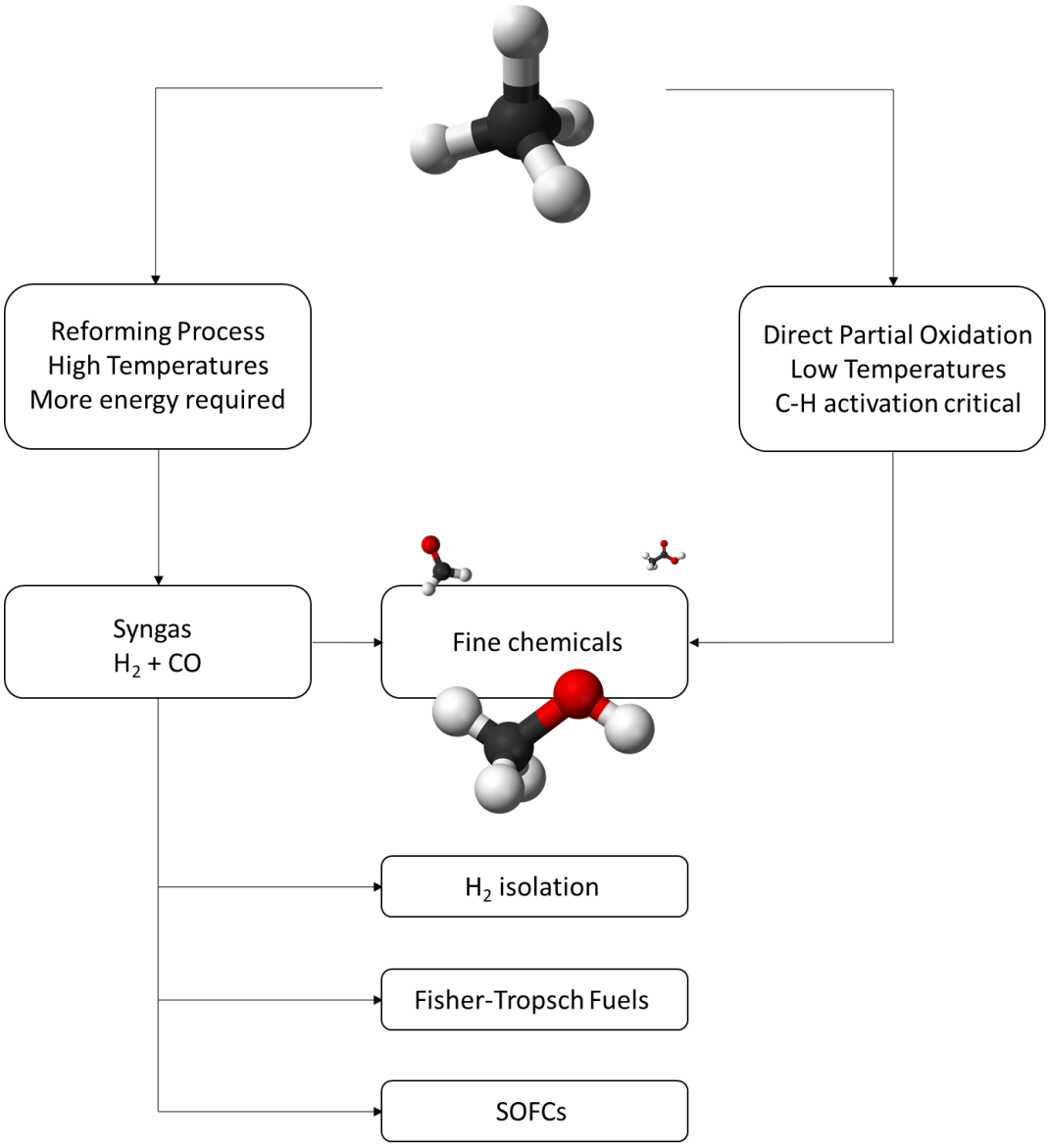


**Figure 8:** schematic representation of the discussed methane valorization routes.

# 1.4. Carbon Dioxide: ways of valorization

Among the main strategies which have been considered to minimize $CO_2$ atmospheric emissions, its capture and storage is one of the most studied[126–128]. This process involves the separation of $CO_2$ from the industrial source and a subsequent compression and transportation. The utilization of the separated $CO_2$ for the synthesis of fuels and as a building block for the synthesis of fine chemicals represents a useful approach for a true valorization of this molecule[126,129–131]. However, $CO_2$ represents the most oxidized form of carbon, hence the thermodynamic and stability of this molecule are the main reasons of its kinetic inertness. Thus, also for this molecule the activation and consequent transformation represent a great challenge in the heterogenous catalysis field. The achieving of this challenge will represent an important step in the sense of a carbon-free footprint circular economy since $CO_2$ should substitute fossil carbon as feedstock for the production of fuels and fine chemicals, while the renewable resources such as solar, wind, geothermal and the abovementioned biomasses should be employed for the production of electricity and hydrogen[110,132].

In the following, we will present the main strategies for $CO_2$ valorization excluding the already discussed DRM process, which represents an interesting method for $CO_2$ valorization[133–135].

## 1.4.1 Hydrogenation of $CO_2$

Another appealing method of $CO_2$ transformation is represented by the $CO_2$ hydrogenation which in many cases represents the first step for the transformation of this molecule into valuable chemicals and can lead to a series of products such as CO (*via* RWGS), alcohols and hydrocarbons[136,137]. If the hydrogen comes from renewable resources, e.g. by biomasses as discussed above, this process could allow an almost carbon neutral cycle.

#### 1.4.1.1 Reverse Water Gas Shift and Fischer-Tropsch

The reduction of $CO_2$ to CO by Reverse Water Gas Shift (Eq. 6) is an important reaction for the production since CO is an important intermediate for the synthesis of valuable chemicals[110,136,137] such as Fischer-Tropsch (FT) fuels.

$$CO_2 + H_2 \rightarrow CO + H_2O \quad (\Delta H^0_{298K} = 41 \text{ kJ/mol}) \quad \text{Equation 6}$$

Concerning this last example, the hydrogenation of $CO_2$ to medium chain hydrocarbons through Fischer-Tropsch synthesis has been recently addressed as a way for carbon dioxide upgrading. Since RWGS represents an important first step for this reaction, the development of heterogenous catalysts active for both RWGS and FT represents an ambitious challenge[138]. The challenge lies in the difficult design of the catalyst, which must possess both RWGS and FT functionalities. Several works, recently reviewed by our group[110], obtained interesting results in this field[138,139].

#### 1.4.1.2 Hydrogenation of $CO_2$ to methanol

Another promising process of valorization of carbon dioxide consists of its hydrogenation to methanol (Eq. 9)[130].

$$CO_2 + 3H_2 \rightarrow CH_3OH + H_2O \quad (\Delta H^0_{298K} = \text{ kJ/mol}) \quad \text{Equation 9}$$

Eq. 9 represents the main reaction occurring during this process, however RWGS represents the main side reaction, which, by virtue of the extra hydrogen consumption, negatively affects the methanol formation[140]. Moreover, the large amount of water formed as a by-product, from both methanol synthesis and the reverse water-gas shift side reaction, also had an inhibitory effect on the active metal during the reaction[131,141], leading to the deactivation of the catalyst. Furthermore, the formation of other hydrogenated products such as higher alcohols and hydrocarbons usually associated with methanol formation, represents a poor selectivity of this process, which by consequence needs to be addressed towards highly active and selective catalysts[140]. Many efficient catalytic systems have been reported, including homo- and heterogeneous catalysts[142–145]. Concerning the heterogenous catalysts, the study of the SMSI is of great importance for the development of active catalysts, and in particular the interfaces between metals and supports usually serve as active sites for $CO_2$ activation and conversion to methanol[110,146]. Metal-ceria interfaces recently revealed to be a key parameter for the hydrogenation of $CO_2$ to methanol[147,148] and, with more detail, Copper ceria interfaces in inverse ceria-copper catalysts[149–151].

### 1.4.1.3. Hydrogenation of $CO_2$ to methane.

Another important and promising process for $CO_2$ valorization is represented by its fully hydrogenation to methane, known as Sabatier reaction of $CO_2$ methanation (Eq. 10) and represents a virtuous example of conversion of waste into energy[110,152,153]. Moreover, it could represent a suppletive methane resource, further reducing the dependence from other countries importations.

$$CO_2 + 4H_2 \rightarrow CH_4 + 2H_2O \quad (\Delta H^0_{298K} = -252.9 \text{ kJ/mol}) \text{ Equation 10}$$

The catalysts for $CO_2$ methanation comprises noble or transition metals on various supports, which have an important effect on the reaction mechanism[154,155]. The research conducted on ceria-based materials dates back in the 90s[156,157] when it was firstly evidenced the superior activity of metals supported on cerium oxide respect other similar supported catalysts. The peculiar redox properties and the presence of surface oxygen vacancies revealed to have a crucial role in the enhanced activity of these materials towards this reaction, as it was confirmed also by more recent studies conducted in Ni and Ru supported on ceria, which are amongst the most studied systems for this reaction[158–162].

Figure 9 summarizes the discussed strategies for $CO_2$ valorization.

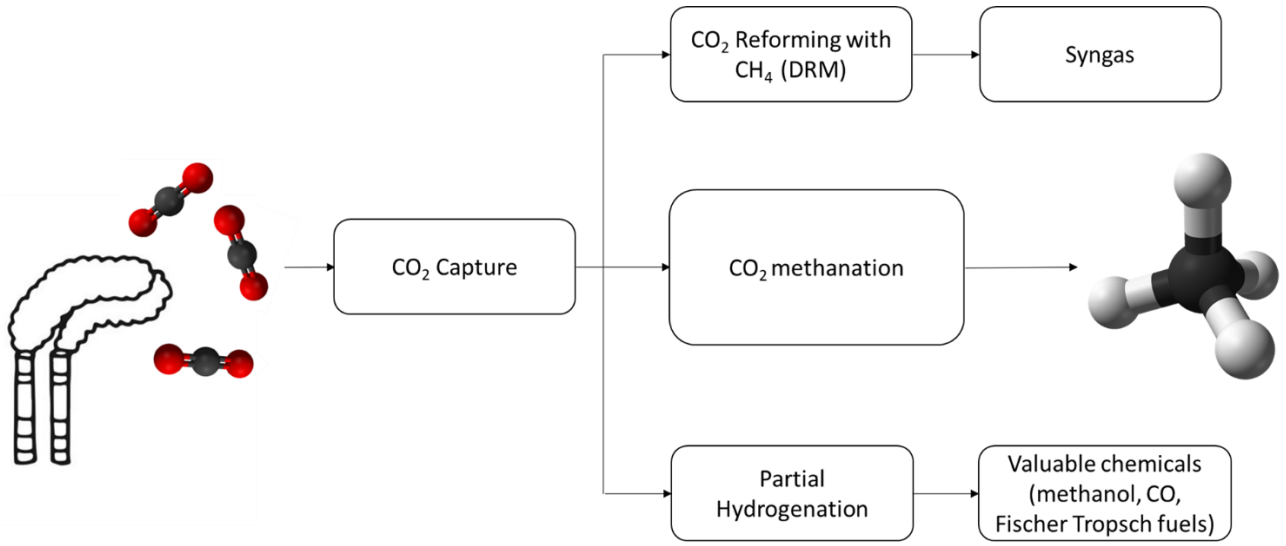


**Figure 9:** schematic representation of the discussed $CO_2$ valorization routes.

# 1.5 Mechano-chemical Synthesis

As pointed out in the overview, it is important to develop synthetic strategies favorable from and industrial standpoint and possibly in agreement with the principles of green chemistry. Mechanochemistry, that is, the use of mechanical energy to promote chemical transformations[163,164] perfectly matches with the principles of green chemistry since it does not require any solvent thus it does not produce any waste by-product compared to other synthetic strategies. The mechanical energy is generally released by milling the desired reactants in a ball-mill apparatus, where the movement of the grinding bowl imposes kinetic and potential energy to the grinding balls. In turn, the grinding spheres release mechanical energy to the reactants through impacts occurring during milling. Moreover, by virtue of its simplicity and versatility, it is appealing from an industrial standpoint. The mechanochemical approach via ball milling was extensively investigated for the solid synthesis of mixed oxides, alloys and novel materials[165–169]. Nowadays, the increasing attention towards greener and more sustainable processes made ball milling an interesting candidate in several chemistry fields ranging from organic chemistry[170] to inorganic chemistry[171]. The possibility of overcoming thermodynamic equilibria made the mechanochemical processes very attractive for the synthesis of catalytic materials. However, the main drawback of this kind of synthesis for catalytic applications is represented by the lack of theoretical background[172]. By consequence a trial-and-error approach is often required for the synthesis of these materials. However, this kind of approach revealed to be successful for the synthesis of many catalytic materials that presented an enhanced catalytic activity compared to conventionally prepared heterogenous catalysts by virtue of the formation of metastable structures generated by the mechanical energy provided from this synthesis[173–177]. Recent studies have focused on metal-supported catalysts, where the possibility of depositing the metal on the support oxide and promoting the metal-support interaction was investigated with encouraging[178–182] results. This suggests that further work is needed in order to correlate the studies on the mechano-chemical process to the synthesis of supported heterogeneous catalysts, particularly because an understanding of the chemistry taking place at nanoscale induced by mechanical forces is missing. In our group this kind of synthetic approach was investigated and gave excellent results in the synthesis of $Pd/CeO_2$ and $Pt\text{-}Pd/CeO_2$ systems that showed excellent activity and stability in methane combustion in both dry and wet atmospheres. The reason of this peculiar and enhanced catalytic activities was found to be related to some morphological characteristics generated specifically from the synthetic method used[172,177,183–185]. These promising catalysts were synthesized with a particular ball milling procedure, namely Mild Energy Ball Milling, whose difference with the classic High Energy Ball Milling lies in several parameters such as the number of balls used and the movement of the apparatus which clearly affected the quantity of mechanical energy provided to the reactants (Figure 10).

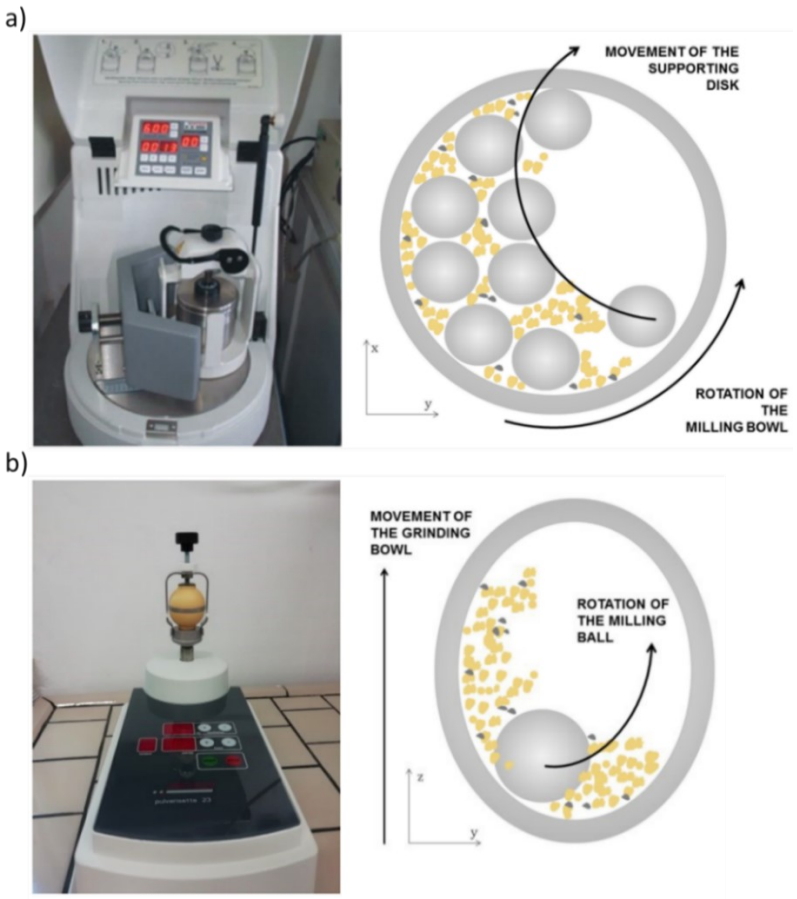


**Figure 10:** a) Fritsch Pulverisette 6 planetary ball mill with schematic movement of milling bowl and spheres; b) Fritsch Pulverisette 23 mill with schematic movement of the milling bowl and sphere. Image taken from Ref. 172.

A careful perusal of the effect of the milling system was studied and the results confirmed that the soft shear-like stresses induced by the mild-energy ball milling apparatus were responsible for the creation of the cited morphological structures[172,183].

Given this promising background, the aim of this PhD thesis has been to further investigate this novel mild-energy ball milling technique for the synthesis of metal supported catalysts based on cerium oxide and cheap and relatively abundant transition metals. In particular, several nickel supported on ceria catalysts have been synthesized and tested in the DRM reaction (chapter 3) and a series of inverse $CeO_2$/CuO catalysts for the activation of methane at low temperatures (chapter 4). In both cases High Surface Area ceria was used, and revealed to be, especially in the case of the inverse $CeO_2$/CuO catalysts, of particular importance for the peculiar characteristics of the system. For this reason further efforts have been made for the development of a synthetic procedure to obtain of high surface area cerium oxide, (Section 2.2.1. of Chapter 2).

# 1.6. References.


1. UNFCCC. Kyoto Protocol. (1997).
2. UNFCCC. Paris Agreement. (2016).
3. IPCC. *Technical Summary. Contribution of Working Group I to the Sixth Assessment Report of the Intergovernmental Panel on Climate Change*. *Climate Change 2021: The Physical Science Basis.* (2021).
4. Stern, N. A time for action on climate change and a time for change in economics. *Econ. J.* ueac005 (2022).
5. Cho, H. M. & He, B. Q. Spark ignition natural gas engines—A review. *Energy Convers. Manag.* **48**, 608–618 (2007).
6. Pourkhesalian, A. M., Shamekhi, A. H. & Salimi, F. Alternative fuel and gasoline in an SI engine: A comparative study of performance and emissions characteristics. *Fuel* **89**, 1056–1063 (2010).
7. U.S. EPA. Global Greenhouse Gas Emissions Data. https://www.epa.gov/ghgemissions/understanding-global-warming-potentials.
8. Miller, S. M., Wofsy, S. C., Michalak, A. M., Kort, E. A., Andrews, A. E., Biraud, S. C., Dlugokencky, E. J. & Eluszkiewicz, J., Fischer, M. L., Janssens-Maenhout, G., Miller, B. R., Miller, J. B., Montzka, S. A., Nehrkorn, T., Sweeney, C. Anthropogenic emissions of methane in the United States. *PNAS* **110**, 20018–20022 (2013).
9. Hopkins, F. M., Ehleringer, J. M., Bush, S. M., Duren, R. M., Miller, C. E., Lai, C. & Hsu, Y., Carranza, V. Randerson, J. T. Earth's Future Mitigation of methane emissions in cities: How new measurements and partnerships can contribute to emissions reduction strategies. *AGU Publ.* 408–425 (2016).
10. Aneggi, E., Boaro, M., Colussi, S., de Leitenburg, C. & Trovarelli, A. Ceria-Based Materials in Catalysis: Historical Perspective and Future Trends. *Handb. Phys. Chem. Rare Earths* **50**, 209–242 (2016).
11. Centi, G., Ciambelli, P., Perathoner, S. & Russo, P. Environmental catalysis: trends and outlook. *Catal. Today* **75**, 3–15 (2002).
12. Dai, Y., Liu, W., Formo, E., Sun, Y. & Xia, Y. Ceramic nanofibers fabricated by electrospinning and their applications in catalysis, environmental science, and energy technology. *Polym. Adv. Technol.* **22**, 326–338 (2011).
13. Rong, H., Ji, S., Zhang, J., Wang, D. & Li, Y. Synthetic strategies of supported atomic clusters for heterogeneous catalysis. *Nat. Commun.* **11**, 5884 (2020).
14. Das, S. Ramirez, P. J., Gong J., Dewangan, N., Hidajat, K., Gates, B. C., Kawi, S. Core–shell structured catalysts for thermocatalytic, photocatalytic, and electrocatalytic conversion of CO2. *Chem Soc Rev* **49**, 2937–3004 (2020).

15. Yamamoto, K., Imaoka, T., Tanabe, M. & Kambe, T. New Horizon of Nanoparticle and Cluster Catalysis with Dendrimers. *Chem. Rev.* **120**, 1397–1473 (2020).
16. Zang, W., Li, G., Wang, L. & Zhang, X. Catalytic hydrogenation by noble-metal nanocrystals with well-defined facets: A review. *Catal. Sci. Technol.* **5**, 2532–2553 (2015).
17. Cargnello, M., Doan-Nguyen, V. T., Gordon, T. R., Diaz, R. E., Stach, E. A., Gorte, R. J., Fornasiero, P., Murray, C. B. Control of metal nanocrystal size reveals metal-support interface role for ceria catalysts. *Science (80-. ).* **341**, 771–773 (2013).
18. Dahle, J. T. & Arai, Y. Environmental Geochemistry of Cerium: Applications and Toxicology of Cerium Oxide Nanoparticles. *Int. J. Environ. Res. Public Heal.* **12**, 1253–1278 (2015).
19. Trovarelli, A. *Catalysis by Ceria and Related Materials*. (2002).
20. Walkey, C., Das, S., Seal, S., Erlichman, J., Heckman, K., Ghibelli, L. & Traversa, E., McGinnis, J. F., Self, W. T. Catalytic properties and biomedical applications of cerium oxide nanoparticles. *Environ. Sci. Nano* **2**, 33–53 (2015).
21. Trovarelli, A. Catalytic Properties of Ceria and CeO2 containing materials. *Catal. Rev. Sci. Eng.* **38**, 439–520 (1996).
22. Li, P., Chen, X., Li, Y. & Schwank, J. W. A review on oxygen storage capacity of CeO 2 -based materials: Influence factors, measurement techniques, and applications in reactions related to catalytic automotive emissions control. *Catal. Today* **327**, 90–115 (2019).
23. Meriaudeau, P., Dutel, J. F., Dufaux, M. & Naccache, C. Further Investigation on Metal-Support Interaction: TiO2, CeO2, SiO2 Supported Platinum Catalysts. *Stud. Surf. Sci. Catal.* **11**, 95–104 (1982).
24. Bernal, S., Calvino, J. J., Cauqui, M. A., Cifredo, G. A. & Jobacho, A., Rodríguez-Izquierdo, J. M. Metal-support interaction phenomena in rhodium/ceria and rhodium/titania catalysts: Comparative study by high-resolution transmission electron spectroscopy. *Appl. Catal. A Gen.* **99**, 1–8 (1993).
25. Onn, T. M., Zhang, S., Arroyo-Ramirez, L., Xia, Y. & Wang, C., Pan, X., Graham, G. W., Gorte, R. J. High-surface-area ceria prepared by ALD on Al2O3 support. *Appl. Catal. B Environ.* **201**, 430–437 (2017).
26. Reddy, B. M., Gode & Lakshmi Katta, T. Design of Efficient Ce x M 12x O 22d (M 5 Zr, Hf, Tb and Pr) Nanosized Model Solid Solutions for CO Oxidation. *Catal. Letters* **141**, 572–581 (2011).
27. Reddy, B. M., Katta, L. & Thrimurthulu, G. Novel nanosized CexZr1−xO2, CexHf1−xO2 and CexTb1−xO2−δ solid solutions: Structural characteristics and catalytic performance. *Catal. Today* **175**, 585–592 (2011).
28. Mai, H.-X., Sun, L. D., Zhang, Y.-W., Si, R., Feng, W., Zhang, H.-P., Liu, H.-C., Yan, C.-H. Shape-Selective Synthesis and Oxygen Storage Behavior of Ceria Nanopolyhedra, Nanorods, and Nanocubes. *J. Phys. Chem. B* **109**, 24380–24385 (2005).
29. S. Sreeremya, T., Krishnan, A., C. Remani, K., R. Patil, K. & F. Brougham, D., Ghosh, S. Shape-Selective

Oriented Cerium Oxide Nanocrystals Permit Assessment of the Effect of the Exposed Facets on Catalytic Activity and Oxygen Storage Capacity. *ACS Appl. Mater. & Interfaces* **7**, 8545–8555 (2015).

30. Aneggi, E., Wiater, D., de Leitenburg, C., Llorca, J. & Trovarelli, A. Shape-Dependent Activity of Ceria in Soot Combustion. *ACS Catal.* **4**, 172–181 (2013).
31. Piumetti, M., Andana, T., Bensaid, S., Russo, N., Fino, D., Pirone, R. Study on the CO Oxidation over Ceria-Based Nanocatalysts. *Nanoscale Res. Lett.* **11**, 165–173 (2016).
32. Du, X., Zhang, D., Shi, L., Gao, R. & Zhang, J. Morphology dependence of catalytic properties of Ni/CeO 2 nanostructures for carbon dioxide reforming of methane. *J. Phys. Chem. C* **116**, 10009–10016 (2012).
33. Laosiripojana, N., Sutthisripok, W. & Assabumrungrat, S. Reactivity of high surface area CeO2 synthesized by surfactant-assisted method to ethanol decomposition with and without steam. *Chem. Eng. J.* **127**, 31–38 (2007).
34. Liang, Q., Wu, A. X., Xiaodi, A. E., Ae, W. & Weng, D. Role of Surface Area in Oxygen Storage Capacity of Ceria-Zirconia as Soot Combustion Catalyst. *Catal. Letters* **119**, 265–270 (2007).
35. Yang, J., Lukashuk, L., Li, H., Föttinger, K., Rupprechter, G., Schubert, U. High Surface Area Ceria for CO Oxidation Prepared from Cerium t-Butoxide by Combined Sol-Gel and Solvothermal Processing. *Catal. Letters* **144**, 403–412 (2014).
36. Laosiripojana, N. & Assabumrungrat, S. Catalytic dry reforming of methane over high surface area ceria. *Appl. Catal. B Environ.* **60**, 107–116 (2005).
37. Laosiripojana, N. & Assabumrungrat, S. The effect of specific surface area on the activity of nano-scale ceria catalysts for methanol decomposition with and without steam at SOFC operating temperatures. *Chem. Eng. Sci.* **61**, 2540–2549 (2006).
38. Fornasiero, P., Kašpar, J., Sergo, V. & Graziani, M. Redox Behavior of High-Surface-Area Rh-, Pt-, and Pd-Loaded Ce0.5Zr0.5O2Mixed Oxide. *J. Catal.* **182**, 56–69 (1999).
39. C. Fink, A. Hagermeyer, Z. Hogan, A. Volpe Jr, J. Y. High Surface Area Cerium Oxide. *Curr. Catal.* **5**, 182–202 (2016).
40. Bickford, E. S., Velu, S. & Song, C. Nano-structured CeO2 supported Cu-Pd bimetallic catalysts for the oxygen-assisted water–gas-shift reaction. *Catal. Today* **99**, 347–357 (2005).
41. Bumajdad, A., I. Zaki, M., Eastoe, J. & Pasupulety, L. Microemulsion-Based Synthesis of CeO2 Powders with High Surface Area and High-Temperature Stabilities. *Langmuir* **20**, 11223–11233 (2004).
42. Phonthammachai, N., Rumruangwong, M., Gulari, E., Jamieson, A. M., Jitkarnka, S., Wongkasemjit, S. Synthesis and rheological properties of mesoporous nanocrystalline CeO2 via sol–gel process. *Colloids Surfaces A Physicochem. Eng. Asp.* **247**, 61–68 (2004).

43. Zhou, X.-D., Huebner, W. & U. Anderson, H. Processing of Nanometer-Scale CeO2 Particles. *Chem. Mater.* **15**, 378–382 (2002).
44. Bruce, L. A., Hoang, M., Hughes, A. E. & Turney, T. W. Surface area control during the synthesis and reduction of high area ceria catalyst supports. *Appl. Catal. A Gen.* **134**, 351–362 (1996).
45. Terribile, D., Trovarelli, A., de Leitenburg, C., Dolcetti, G. & Llorca, J. Unusual Oxygen Storage/Redox Behavior of High-Surface-Area Ceria Prepared by a Surfactant-Assisted Route. *Chem. Mater.* **9**, 2676–2678 (1997).
46. Zhang, Y.-W., Si, R., Liao, C.-S., Yan, C.-H., Xiao, C.-X., Kou, Y. Facile Alcohothermal Synthesis, Size-Dependent Ultraviolet Absorption, and Enhanced CO Conversion Activity of Ceria Nanocrystals. *J. Phys. Chem. B* **107**, 10159–10167 (2003).
47. Masui, T., Hirai, H., Hamada, R., Imanaka, N., Adachi, G. Y., Sakata, T., Mori, H. Synthesis and characterization of cerium oxide nanoparticles coated with turbostratic boron nitride. *J. Mater. Chem.* **13**, 622–627 (2003).
48. Anastas, P. & Eghbali, N. Green Chemistry: Principles and Practice. *Chem. Soc. Rev.* **39**, 301–312 (2010).
49. Tok, A. I. Y., Boey, F. Y. C., Dong, Z. & Sun, X. L. Hydrothermal synthesis of CeO 2 nano-particles. *J. Mater. Process. Technol.* **190**, 217–222 (2007).
50. Trovarelli, A., De Leitenburg, C., Boaro, M. & Dolcetti, G. The utilization of ceria in industrial catalysis. *Catal. Today* **50**, 353–367 (1999).
51. Kubsh, J. E., Rieck, J. S. & Spencer, N. D. Cerium Oxide Stabilization: Physical Property and Three-Way Activity Considerations. *Stud. Surf. Sci. Catal.* **71**, 125–138 (1991).
52. Summers, J. C. & Ausen, S. A. Interaction of cerium oxide with noble metals. *J. Catal.* **58**, 131–143 (1979).
53. Diwell, A. F., Rajaram, R. R., Shaw, H. A. & Truex, T. J. The Role of Ceria in Three-Way Catalysts. *Stud. Surf. Sci. Catal.* **71**, 139–152 (1991).
54. Akah, A. Application of rare earths in fluid catalytic cracking: A review. *J. Rare Earths* **35**, 941–956 (2017).
55. Courcot, D., Abi-Aad, E., Capelle, S. & Aboukaïs, A. Investigation of copper-cerium oxide catalysts in the combustion of diesel soot. *Stud. Surf. Sci. Catal.* **116**, 625–634 (1998).
56. Liu, S., Wu, X., Weng, D. & Ran, R. Ceria-based catalysts for soot oxidation: a review. *J. Rare Earths* **33**, 567–590 (2015).
57. Kurian, M. Cerium oxide based materials for water treatment – A review. *J. Environ. Chem. Eng.* **8**, 104439 (2020).
58. Toso, A., Colussi, S., Padigapaty, S., de Leitenburg, C. & Trovarelli, A. High stability and activity of solution combustion synthesized Pd-based catalysts for methane combustion in presence of water.

*Appl. Catal. B Environ.* **230**, 237–245 (2018).

59. Bozo, C., Guilhaume, N. & Herrmann, J. M. Role of the Ceria–Zirconia Support in the Reactivity of Platinum and Palladium Catalysts for Methane Total Oxidation under Lean Conditions. *J. Catal.* **203**, 393–406 (2001).
60. Salazar-Villalpando, M. D., Berry, D. A. & Gardner, T. H. Partial oxidation of methane over Rh/supported-ceria catalysts: Effect of catalyst reducibility and redox cycles. *Int. J. Hydrogen Energy* **33**, 2695–2703 (2008).
61. Chien, A. C., Ye, N. J., Huang, C.-W. & Tseng, I.-H. Studies of Nickel/Samarium-Doped Ceria for Catalytic Partial Oxidation of Methane and Effect of Oxygen Vacancy. *Catalysts* **11**, 731–742 (2021).
62. Carrillo, A. J., Navarrete, L., Laqdiem, M., Balaguer, M. & Serra, J. M. Boosting methane partial oxidation on ceria through exsolution of robust Ru nanoparticles Boosting methane partial oxidation on ceria through exsolution of robust Ru nanoparticles. *Mater. Adv* **2**, 2924 (2021).
63. Biswas, S., Kundu, C., P. Kulkarni, A., Kattel, S., Giddey, S., Bhattacharya, S. A Study on CO2 Hydrogenation Using a Ceria–Zirconia Mixed Oxide (CexZr1–xO2)-Supported Fe Catalyst. *Ind. & Eng. Chem. Res.* **60**, 14410–14423 (2021).
64. Ouyang, B., Tan, W. & Liu, B. Morphology effect of nanostructure ceria on the Cu/CeO2 catalysts for synthesis of methanol from CO2 hydrogenation. *Catal. Commun.* **95**, 36–39 (2017).
65. Winter, L. R., Gomez, E., Yan, B., Yao, S. & Chen, J. G. Tuning Ni-catalyzed CO2 hydrogenation selectivity via Ni-ceria support interactions and Ni-Fe bimetallic formation. *Appl. Catal. B Environ.* **224**, 442–450 (2018).
66. Feio, L. S.F., Hori, C. E., Damyanova, S., Noronha, F. B., Cassinelli, W. H., Marques, C. M.P., Bueno, J. M. C. The effect of ceria content on the properties of Pd/CeO2/Al2O3 catalysts for steam reforming of methane. *Appl. Catal. A Gen.* **316**, 107–116 (2007).
67. Iglesias, I. D., Baronetti, G. & Mariño, F. Nickel-based doped ceria-supported catalysts for steam reforming of methane at mild conditions. *Energy Sources, Part A Recover. Util. Environ. Eff.* **39**, 129–133 (2017).
68. Wang, F., Xu, L., Yang, J., Zhang, J., Zhang, L., Li, H., Zhao, Y., Li, H. X., Wu, K., Xu, G. Q., Chen, W. Enhanced catalytic performance of Ir catalysts supported on ceria-based solid solutions for methane dry reforming reaction. *Catal. Today* **281**, 295–303 (2017).
69. Laosiripojana, N., Sutthisripok, W. & Assabumrungrat, S. Synthesis gas production from dry reforming of methane over CeO2 doped Ni/Al2O3: Influence of the doping ceria on the resistance toward carbon formation. *Chem. Eng. J.* **112**, 13–22 (2005).
70. Zhang, B., Tang, X., Li, Y., Cai, W., Xu, Y., Shen, W. Steam reforming of bio-ethanol for the production of hydrogen over ceria-supported Co, Ir and Ni catalysts. *Catal. Commun.* **7**, 367–372 (2006).
71. Raza, R., Zhu, B., Rafique, A., Naqvi, M. R. & Lund, P. Functional ceria-based nanocomposites for

advanced low-temperature (300–600 °C) solid oxide fuel cell: A comprehensive review. *Mater. Today Energy* **15**, 100373 (2020).

72. Putna, E. S., Stubenrauch, J., Vohs, J. M. & Gorte, R. J. Ceria-Based Anodes for the Direct Oxidation of Methane in Solid Oxide Fuel Cells. *Langmuir* **11**, 4832–4837 (1995).
73. Bellardita, M., Fiorenza, R., Palmisano, L. & Scirè, S. Photocatalytic and photothermocatalytic applications of cerium oxide-based materials. *Cerium Oxide Synth. Prop. Appl.* 109–167 (2020).
74. Chen, W., Xue, J., Bao, Y. & Feng, L. Surface engineering of nano-ceria facet dependent coupling effect on Pt nanocrystals for electro-catalysis of methanol oxidation reaction. *Chem. Eng. J.* **381**, 122752 (2020).
75. Chen, Y., Ma, J., Han, B., Zhang, P., Hua, H., Chen, H., Su, X. Emissions of automobiles fueled with alternative fuels based on engine technology: A review. *J. Traffic Transp. Eng. (English Ed.* **5**, 318–334 (2018).
76. Kakaee, A. H., Paykani, A. & Ghajar, M. The influence of fuel composition on the combustion and emission characteristics of natural gas fueled engines. *Renew. Sustain. Energy Rev.* **38**, 64–78 (2014).
77. Godec, M. & Baron, R. Natural gas. *Energy (Norwalk, Connect.* **22**, 14 (1997).
78. Tavana, M., Pirdashti, M., Kennedy, D. T., Belaud, J. P. & Behzadian, M. A hybrid Delphi-SWOT paradigm for oil and gas pipeline strategic planning in Caspian Sea basin. *Energy Policy* **40**, 345–360 (2012).
79. Scholten, D. & Bosman, R. The geopolitics of renewables; exploring the political implications of renewable energy systems. *Technol. Forecast. Soc. Change* **103**, 273–283 (2016).
80. Scholten, D., Bazilian, M., Overland, I. & Westphal, K. The geopolitics of renewables: New board, new game. *Energy Policy* **138**, 111059 (2020).
81. Su, C. W., Khan, K., Umar, M. & Zhang, W. Does renewable energy redefine geopolitical risks? *Energy Policy* **158**, 112566 (2021).
82. Van de Graaf, T., Overland, I., Scholten, D. & Westphal, K. The new oil? The geopolitics and international governance of hydrogen. *Energy Res. Soc. Sci.* **70**, 101667 (2020).
83. Muhammad Nasir, I., Mohd Ghazi, T. I. & Omar, R. Production of biogas from solid organic wastes through anaerobic digestion: a review. *Appl. Microbiol. Biotechnol.* **95**, 321–329 (2012).
84. Zhang, C., Su, H., Baeyens, J. & Tan, T. Reviewing the anaerobic digestion of food waste for biogas production. *Renew. Sustain. Energy Rev.* **38**, 383–392 (2014).
85. Karellas, S., Boukis, I. & Kontopoulos, G. Development of an investment decision tool for biogas production from agricultural waste. *Renew. Sustain. Energy Rev.* **14**, 1273–1282 (2010).
86. Scarlat, N., Dallemand, J. F. & Fahl, F. Biogas: Developments and perspectives in Europe. *Renew. Energy* **129**, 457–472 (2018).
87. Brémond, U., Bertrandias, A., Steyer, J. P., Bernet, N. & Carrere, H. A vision of European biogas

sector development towards 2030: Trends and challenges. *J. Clean. Prod.* **287**, 125065 (2021).

88. Taherian, Z., Khataee, A., Han, N. & Orooji, Y. Hydrogen production through methane reforming processes using promoted-Ni/mesoporous silica: A review. *J. Ind. Eng. Chem.* **In press**, (2021).
89. De Lorenzo, G. & Fragiacomo, P. Energy analysis of an SOFC system fed by syngas. *Energy Convers. Manag.* **93**, 175–186 (2015).
90. Kamm, B. Production of platform chemicals and synthesis gas from biomass. *Angew. Chemie - Int. Ed.* **46**, 5056–5058 (2007).
91. Pruett, R. L. Synthesis gas: A raw material for industrial chemicals. *Science (80-. ).* **211**, 11–16 (1981).
92. Gao, F., Wang, S., Wang, W., Duan, J., Dong, J., Chen, G. Adsorption separation of CO from syngas with CuCl@AC adsorbent by a VPSA process. *RSC Adv.* **8**, 39362–39370 (2018).
93. Saha, D. & Deng, S. Adsorption Equilibria and Kinetics of Carbon Monoxide on Zeolite 5A, 13X, MOF-5, and MOF-177. *J. Chem. & Eng. Data* **54**, 2245–2250 (2009).
94. Angeli, S. D., Monteleone, G., Giaconia, A. & Lemonidou, A. A. State-of-the-art catalysts for CH4 steam reforming at low temperature. *Int. J. Hydrogen Energy* **39**, 1979–1997 (2014).
95. Ozavize Ayodele, F., Mustapa, S. I., Ayodele, B. V. & Mohammad, N. An Overview of Economic Analysis and Environmental Impacts of Natural Gas Conversion Technologies. *sustainability* **12**, 10148 (2020).
96. Howarth, A. & Jacobson. How green is blue hydrogen? *Energy Sci. Eng.* **9**, 1676–1687 (2021).
97. Minh, D. P., Siang, T. J., Vo, D. V. N., Phan, T. S., Ridart, C., Nzihou, A., Grouset, D. Hydrogen Production From Biogas Reforming: An Overview of Steam Reforming, Dry Reforming, Dual Reforming, and Tri-Reforming of Methane. *Hydrog. Supply Chain Des. Deploy. Oper.* 111–166 (2018).
98. Mourhly, A., Kacimi, M., Halim, M. & Arsalane, S. New low cost mesoporous silica (MSN) as a promising support of Ni-catalysts for high-hydrogen generation via dry reforming of methane (DRM). *Int. J. Hydrogen Energy* **45**, 11449–11459 (2020).
99. Peng, H., Zhang, X., Zhang, L., Rao, C., Lian, J., Liu, W., Ying, J., Zhang, G., Wang, Z., Zhang, N., Wang, X. One-Pot Facile Fabrication of Multiple Nickel Nanoparticles Confined in Microporous Silica Giving a Multiple-Cores@Shell Structure as a Highly Efficient Catalyst for Methane Dry Reforming. *ChemCatChem* **9**, 127–136 (2017).
100. Usman, M., Wan Daud, W. M. A. & Abbas, H. F. Dry reforming of methane: Influence of process parameters—A review. *Renew. Sustain. Energy Rev.* **45**, 710–744 (2015).
101. Aramouni, N. A. K., Touma, J. G., Tarboush, B. A., Zeaiter, J. & Ahmad, M. N. Catalyst design for dry reforming of methane: Analysis review. *Renew. Sustain. Energy Rev.* **82**, 2570–2585 (2018).
102. Spivey, J. A review of dry (CO2) reforming of methane over noble metal catalysts. *Chem Soc Rev* **43**, 7813–7837 (2014).
103. Lavoie, J.-M. & Luis Sanchez, J. Review on dry reforming of methane, a potentially more

environmentally-friendly approach to the increasing natural gas exploitation. *Front. Chem.* **2**, 1–17 (2014).

104. Ian, Z., Das, S., Ing, M., Wai, H., Hongmanorom, P., Kawi, S. AReview on Bimetallic Nickel-Based Catalysts for CO 2 Reforming of Methane. *ChemPhysChem* **18**, 3117–3134 (2017).
105. Fan, M. S., Abdullah, A. Z. & Bhatia, S. Utilization of greenhouse gases through dry reforming: Screening of nickel-based bimetallic catalysts and kinetic studies. *ChemSusChem* **4**, 1643–1653 (2011).
106. Wang, S., Q. (Max) Lu, G. & J. Millar, G. Carbon Dioxide Reforming of Methane To Produce Synthesis Gas over Metal-Supported Catalysts: State of the Art. *Energy & Fuels* **10**, 896–904 (1996).
107. Wang, S. A Comprehensive Study on Carbon Dioxide Reforming of Methane over Ni/γ-Al2O3 Catalysts. *Ind. & Eng. Chem. Res.* **38**, 2615–2625 (1999).
108. Barroso-Quiroga, M. M. & Castro-Luna, A. E. Catalytic activity and effect of modifiers on Ni-based catalysts for the dry reforming of methane. *Int. J. Hydrogen Energy* **35**, 6052–6056 (2010).
109. Liu, Z., Grinter, D. C., Lustemberg, P. G., Nguyen-Phan, T. D., Zhou, Y., Luo, S., Waluyo, I., Crumlin, E. J., Stacchiola, D. J. *et al.* Dry Reforming of Methane on a Highly-Active Ni-CeO2Catalyst: Effects of Metal-Support Interactions on C–H Bond Breaking. *Angew. Chemie - Int. Ed.* **55**, 7455–7459 (2016).
110. Boaro M., Colussi S., T. A. Ceria-Based Materials in Hydrogenation and Reforming Reactions for CO2 Valorization. *Front. Chem. | www.frontiersin.org* **7**, 28 (2019).
111. I. Olivos-Suarez, A., Szécsényi, À., J. M. Hensen, E., Ruiz-Martinez, J., A. Pidko, E., Gascon, J. Strategies for the Direct Catalytic Valorization of Methane Using Heterogeneous Catalysis: Challenges and Opportunities. *ACS Catal.* **6**, 2965–2981 (2016).
112. Chen, Q., Dong, A., Wang, D., Qiu, L., Ma, C., Yuan, Y., Zhao, Y., Jia, N., Guo, Z., Wang, N. Efficient and Selective Methane Borylation Through Pore Size Tuning of Hybrid Porous Organic-Polymer-Based Iridium Catalysts. *Angew. Chemie* **131**, 10781–10786 (2019).
113. Caballero, A. & Pérez, P. J. Methane as raw material in synthetic chemistry: The final frontier. *Chem. Soc. Rev.* **42**, 8809–8820 (2013).
114. Huang, W., Zhang, S., Tang, Y., Li, Y., Nguyen, L., Li, Y., Shan, J., Xiao, D., Gagne, R., Frenkel, A. I. & Tao, F. F. Low-Temperature Transformation of Methane to Methanol on Pd1O4Single Sites Anchored on the Internal Surface of Microporous Silicate. *Angew. Chemie - Int. Ed.* **55**, 13441–13445 (2016).
115. Jensen Gunsalus, N., Koppaka, A., Hume Park, S., M. Bischof, S., G. Hashiguchi, B., A. Periana, R. Homogeneous Functionalization of Methane. *Chem. Rev.* **117**, 8521–8573 (2017).
116. D. Gesser, H., R. Hunter, N. & B. Prakash, C. The direct conversion of methane to methanol by controlled oxidation. *Chem. Rev.* **85**, 235–244 (2002).
117. D. Senanayake, S., A. Rodriguez, J. & F. Weaver, J. Low Temperature Activation of Methane on

Metal-Oxides and Complex Interfaces: Insights from Surface Science. *Acc. Chem. Res.* **53**, 1488–1497 (2020).

118. A. Arndtsen, B., G. Bergman, R., Andrew Mobley, T. & H. Peterson, T. Selective Intermolecular Carbon-Hydrogen Bond Activation by Synthetic Metal Complexes in Homogeneous Solution. *Acc. Chem. Res.* **28**, 154–162 (2002).
119. E. Shilov, A. & B. Shul'pin, G. Activation of C−H Bonds by Metal Complexes. *Chem. Rev.* **97**, 2879–2932 (1997).
120. Coperet, C. C−H Bond Activation and Organometallic Intermediates on Isolated Metal Centers on Oxide Surfaces. *Chem. Rev.* **110**, 656–680 (2009).
121. M. Mayer, J. Understanding Hydrogen Atom Transfer: From Bond Strengths to Marcus Theory. *Acc. Chem. Res.* **44**, 36–46 (2010).
122. Weckhuysen, B. M., Beale, A. M., Luo, W., Yu, T., Li, Z., Jones, W., Liu, Y., He, Q., Song, W., Du, P., Yang, B., An, H., Farmer, D. M., Qiu, C., Wang, A. Identifying key mononuclear Fe species for low-temperature methane oxidation Identifying key mononuclear Fe species for low-temperature methane oxidation. *Chem. Sci.* **12**, 3152–3160 (2021).
123. Osadchii, D., Y. & I. Olivos-Suarez, A., Szécsényi, Á., Li, G., A. Nasalevich, M., A. Dugulan, I., Serra Crespo, P., J. M. Hensen, E., L. Veber, S., V. Fedin, M., Sankar, G., A. Pidko, E., Gascon, J. Isolated Fe Sites in Metal Organic Frameworks Catalyze the Direct Conversion of Methane to Methanol. *ACS Catal.* **8**, 5542–5548 (2018).
124. I. Chan, S. & S.-F. Yu, S. Controlled Oxidation of Hydrocarbons by the Membrane-Bound Methane Monooxygenase: The Case for a Tricopper Cluster. *Acc. Chem. Res.* **41**, 969–979 (2008).
125. Culpepper, M. A. & Rosenzweig, A. C. Architecture and active site of particulate methane monooxygenase. *Crit. Rev. Biochem. Mol. Biol.* **47**, 483–492 (2012).
126. Anderson, S. & Newell, R. Prospects for carbon capture and storage technologies. *Annu. Rev. Environ. Resour.* **29**, 109–142 (2004).
127. Araújo, O. de Q. F. & de Medeiros, J. L. Carbon capture and storage technologies: present scenario and drivers of innovation. *Curr. Opin. Chem. Eng.* **17**, 22–34 (2017).
128. Gibbins, J. & Chalmers, H. Carbon capture and storage. *Energy Policy* **36**, 4317–4322 (2008).
129. Ola, O., Maroto-Valer, M. M. & Mackintosh, S. Turning CO2 into Valuable Chemicals. *Energy Procedia* **37**, 6704–6709 (2013).
130. Raudaskoski, R., Turpeinen, E., Lenkkeri, R., Pongrácz, E. & Keiski, R. L. Catalytic activation of CO2: Use of secondary CO2 for the production of synthesis gas and for methanol synthesis over copper-based zirconia-containing catalysts. *Catal. Today* **144**, 318–323 (2009).
131. Inui, T. & Takeguchi, T. Effective conversion of carbon dioxide and hydrogen to hydrocarbons. *Catal. Today* **10**, 95–106 (1991).

132. J. A. Martens, A. Bogaerts, N. De Kimpe, P. A. Jacobs, G. B. Marin, K. Rabaey, M. Saeys, S. Verhelst, J. A. Martens, A. Bogaerts, N. De Kimpe, P. A. Jacobs, G. B. Marin, K. Rabaey, M. Saeys, S. Verhelst. The Chemical Route to a CO2- neutral world. *ChemSusChem* **10**, 1039–1055 (2017).

133. Rostrup-Nielsen, J. R. & Bak Hansen, J. H. CO2-Reforming of Methane over Transition Metals. *J. Catal.* **144**, 38–49 (1993).

134. Wang, S. & Lu, G. Q. M. CO2 reforming of methane on Ni catalysts: Effects of the support phase and preparation technique. *Appl. Catal. B Environ.* **16**, 269–277 (1998).

135. Li, Z., Lin, Q., Li, M., Cao, J., Liu, F., Pan, H., Wang, Z., Kawi, S. Recent advances in process and catalyst for CO2 reforming of methane. *Renew. Sustain. Energy Rev.* **134**, 110312 (2020).

136. Wang, W., Wang, S., Ma, X. & Gong, J. Recent advances in catalytic hydrogenation of carbon dioxide. *Chem. Soc. Rev.* **40**, 3703–3727 (2011).

137. Kondratenko, E. V., Mul, G., Baltrusaitis, J., Larrazábal, G. O. & Pérez-Ramírez, J. Status and perspectives of CO2 conversion into fuels and chemicals by catalytic, photocatalytic and electrocatalytic processes. *Energy Environ. Sci.* **6**, 3112–3135 (2013).

138. Marc D. Porosoff, B. Y. and J. G. C. Catalytic reduction of CO2 by H2 for synthesis of CO, methanol and hydrocarbons: Challenges and opportunities. *Energy Environ. Sci.* **9**, 62–73 (2016).

139. Samanta, A., Landau, M. V., Vidruk-Nehemya, R. & Herskowitz, M. CO2 hydrogenation to higher hydrocarbons on K/Fe-Al-O spinel catalysts promoted with Si, Ti, Zr, Hf, Mn and Ce. *Catal. Sci. Technol.* **7**, 4048–4063 (2017).

140. Ma, J., Sun, N., Zhang, X., Zhao, N., Xiao, F., Wei, W., Sun, Y. A short review of catalysis for CO2 conversion. *Catal. Today* **148**, 221–231 (2009).

141. Frei, M. S., Capdevila-Cortada, M., García-Muelas, R., Mondelli, C., López, N., Stewart, J. A., Curulla Ferré, D., Pérez-Ramírez, J. Mechanism and microkinetics of methanol synthesis via CO2 hydrogenation on indium oxide. *J. Catal.* **361**, 313–321 (2018).

142. Studt, F., Sharafutdinov, I., Abild-Pedersen, F., Elkjaer, C. F., Hummelshøj, J. S., Dahl, S., Chorkendorff, I., Nørskov, J. K. Discovery of a Ni-Ga catalyst for carbon dioxide reduction to methanol. *Nat. Chem.* **6**, 320–324 (2014).

143. Jiang, X., Nie, X., Guo, X., Song, C. & G. Chen, J. Recent Advances in Carbon Dioxide Hydrogenation to Methanol via Heterogeneous Catalysis. *Chem. Rev.* **120**, 7984–8034 (2020).

144. Wesselbaum, S., Vom Stein, T., Klankermayer, J. & Leitner, W. Hydrogenation of carbon dioxide to methanol by using a homogeneous ruthenium-phosphine catalyst. *Angew. Chemie - Int. Ed.* **51**, 7499–7502 (2012).

145. Wang, J., Li, G., Li, Z., Tang, C., Feng, Z., An, H., Liu, H., Liu, T., Li, C. A highly selective and stable ZnO-ZrO2 solid solution catalyst for CO2 hydrogenation to methanol. *Sci. Adv.* **3**, 1–11 (2017).

146. Wu, C., Cheng, D., Wang, M. & Ma, D. Understanding and Application of Strong Metal–Support

Interactions in Conversion of CO2 to Methanol: A Review. *Energy & Fuels* **35**, 19012–19023 (2021).

147. Kattel, S., Liu, P. & G. Chen, J. Tuning Selectivity of CO2 Hydrogenation Reactions at the Metal/Oxide Interface. *J. Am. Chem. Soc.* **139**, 9739–9754 (2017).
148. Rodriguez, A. J., Liu, P., Stacchiola, D., Senanayake, D. S., White, G. M., Chen, G. J. Hydrogenation of CO2 to Methanol: Importance of Metal–Oxide and Metal–Carbide Interfaces in the Activation of CO2. *ACS Catal.* **5**, 6696–6706 (2015).
149. Senanayake, D. S., Ramírez, J. P., Waluyo, I., Kundu, S., Mudiyanselage, K., Liu, Z., Liu, Z., Axnanda, S., Stacchiola, J. D., Evans, J. & A. Rodriguez, J. Hydrogenation of CO2 to Methanol on CeOx/Cu(111) and ZnO/Cu(111) Catalysts: Role of the Metal–Oxide Interface and Importance of Ce3+ Sites. *J. Phys. Chem. C* **120**, 1778–1784 (2016).
150. Rodriguez, J. A., Grinter, D. C., Liu, Z., Palomino, R. M. & Senanayake, S. D. Ceria-based model catalysts: Fundamental studies on the importance of the metal-ceria interface in CO oxidation, the water-gas shift, CO2 hydrogenation, and methane and alcohol reforming. *Chem. Soc. Rev.* **46**, 1824–1841 (2017).
151. Graciani, J., Mudiyanselage, K., Xu, F., Baber, A. E., Evans, J., Senanayake, S. D., Stacchiola, D. J., Liu, P., Hrbek, J., Fernández Sanz, J. & Rodriguez, J. A. Highly active copper-ceria and copper-ceria-titania catalysts for methanol synthesis from CO2. *Science (80-. ).* **345**, 546–550 (2014).
152. Navarro, J. C., Centeno, M. A., Laguna, O. H. & Odriozola, J. A. catalysts Policies and Motivations for the CO 2 Valorization through the Sabatier Reaction Using Structured Catalysts. A Review of the Most Recent Advances. *Catalysts* **8**, 578–602 (2018).
153. Iaquaniello, G., Setini, S., Salladini, A. & De Falco, M. CO2 valorization through direct methanation of flue gas and renewable hydrogen: A technical and economic assessment. *Int. J. Hydrogen Energy* **43**, 17069–17081 (2018).
154. Frontera, P., Macario, A., Ferraro, M., Antonucci, P., Louis, B., Wang, Q., Pereira, M. M. Supported Catalysts for CO 2 Methanation: A Review. *Catalysts* **7**, 59–86 (2017).
155. Su, X., Xu, J., Liang, B., Duan, H., Hou, B., Huang, Y. Catalytic carbon dioxide hydrogenation to methane: A review of recent studies. *J. Energy Chem.* **25**, 553–565 (2016).
156. De Leitenburg, C. & Trovarelli, A. Metal-Support Interactions in Rh/CeO2, Rh/TiO2, and Rh/Nb2O5 Catalysts as Inferred from CO2 Methanation Activity. *J. Catal.* **156**, 171–174 (1995).
157. De Leitenburg, C., Trovarelli, A. & Kašpar, J. A Temperature-Programmed and Transient Kinetic Study of CO2Activation and Methanation over CeO2Supported Noble Metals. *J. Catal.* **166**, 98–107 (1997).
158. Díez-Ramírez, J., Sánchez, P., Kyriakou, V., Zafeiratos, S., Marnellos, G. E., Konsolakis, M., Dorado, F. Effect of support nature on the cobalt-catalyzed CO2 hydrogenation. *J. CO2 Util.* **21**, 562–571 (2017).
159. Sharma, S., Hu, Z., Zhang, P., McFarland, E. W. & Metiu, H. CO2 methanation on Ru-doped ceria. *J.*

*Catal.* **278**, 297–309 (2011).

160. Bian, Z., Chan, Y. M., Yu, Y. & Kawi, S. Morphology dependence of catalytic properties of Ni/CeO2 for CO2 methanation: A kinetic and mechanism study. *Catal. Today* **347**, 31–38 (2020).
161. Upham, D. C., Derk, A. R., Sharma, S., Metiu, H. & McFarland, E. W. CO2 methanation by Ru-doped ceria: The role of the oxidation state of the surface. *Catal. Sci. Technol.* **5**, 1783–1791 (2015).
162. Cárdenas-Arenas, A., Quindimil, A., Davó-Quiñonero, A., Bailón-García, E., Lozano-Castelló, D., De-La-Torre, U., Pereda-Ayo, B., González-Marcos, J. A., González-Velasco, J. R., Bueno-López, A. Design of active sites in Ni/CeO2 catalysts for the methanation of CO2: tailoring the Ni-CeO2 contact. *Appl. Mater. Today* **19**, 100591 (2020).
163. Takacs, L. The historical development of mechanochemistry. *Chem. Soc. Rev.* **42**, 7649–7659 (2013).
164. Baláž, P., Achimovicová, M., Baláž, M., Billik, P., Zara, C. Z., Criado, J. M., Delogu, F., Dutková, E., Gaffet, E., Gotor, F. J., Kumar, R., Mitov, I., Rojac, T., Senna, M., Streletskii, A., Krystyna, W. C. Hallmarks of mechanochemistry: From nanoparticles to technology. *Chem. Soc. Rev.* **42**, 7571–7637 (2013).
165. Trovarelli, A., Zamar, F., Llorca, J., De Leitenburg, C. & Dolcetti, G., Kiss, J. T. Nanophase Fluorite-Structured CeO2–ZrO2Catalysts Prepared by High-Energy Mechanical Milling. *J. Catal.* **169**, 490–502 (1997).
166. Yadav, T. P., Mukhopadhyay, N. K., Tiwari, R. S. & Srivastava, O. N. Studies on the formation and stability of nano-crystalline Al50Cu28Fe22 alloy synthesized through high-energy ball milling. *Mater. Sci. Eng. A* **393**, 366–373 (2005).
167. Furlani, E., Aneggi, E., de Leitenburg, C. & Maschio, S. High energy ball milling of titania and titania–ceria powder mixtures. *Powder Technol.* **254**, 591–596 (2014).
168. Šepelák, V., Düvel, A., Wilkening, M., Becker, K. D. & Heitjans, P. Mechanochemical reactions and syntheses of oxides. *Chem. Soc. Rev.* **42**, 7507–7520 (2013).
169. Jiang, H. G., Hu, H. M. & Lavernia, E. J. Synthesis of Fe-rich Fe-Al nanocrystalline solid solutions using ball milling. *J. Mater. Res.* **14**, 1760–1770 (1999).
170. Stolle, A., Szuppa, T., Leonhardt, S. E. S. & Ondruschka, B. Ball milling in organic synthesis: Solutions and challenges. *Chem. Soc. Rev.* **40**, 2317–2329 (2011).
171. Garay, A. L., Pichon, A. & James, S. L. Solvent-free synthesis of metal complexes. *Chem. Soc. Rev.* **36**, 846–855 (2007).
172. Danielis, M. Pd/CeO2 Methane Abatement Catalysts Prepared by Solvent-free Mechano-chemical Synthesis. (2020).
173. Jentoft, F. C., Schmelz, H. & Knözinger, H. Preparation of selective catalytic reduction catalysts via milling and thermal spreading. *Appl. Catal. A Gen.* **161**, 167–182 (1997).
174. Kwon, D. W., Park, K. H. & Hong, S. C. The influence on SCR activity of the atomic structure of

V2O5/TiO2 catalysts prepared by a mechanochemical method. *Appl. Catal. A Gen.* **451**, 227–235 (2013).

175. Wang, L. C., Liu, Y. M., Chen, M., Cao, Y., He, H. Y., Wu, G. S., Dai, W. L., Fan, K. N. Production of hydrogen by steam reforming of methanol over Cu/ZnO catalysts prepared via a practical soft reactive grinding route based on dry oxalate-precursor synthesis. *J. Catal.* **246**, 193–204 (2007).
176. Guczi, L., Takács, L., Stefler, G., Koppány, Z. & Borkó, L. Re–Co/Al2O3 bimetallic catalysts prepared by mechanical treatment: CO hydrogenation and CH4 conversion. *Catal. Today* **77**, 237–243 (2002).
177. Danielis, M., Colussi, S., de Leitenburg, C., Soler, L., Llorca, J., Trovarelli, A. Outstanding Methane Oxidation Performance of Palladium-Embedded Ceria Catalysts Prepared by a One-Step Dry Ball-Milling Method. *Angew. Chemie - Int. Ed.* **57**, 10212–10216 (2018).
178. Kamolphop, U., Taylor, F. R. S., Breen, P. J., Burch, R., Delgado, J. J., Chansai, S., Hardacre, C., Hengrasmee, S., James, L. S. Low-Temperature Selective Catalytic Reduction (SCR) of NOx with n-Octane Using Solvent-Free Mechanochemically Prepared Ag/Al2O3 Catalysts. *ACS Catal.* **1**, 1257–1262 (2011).
179. Borchers, C., Martin, M. L., Vorobjeva, G. A., Morozova, O. S., Firsova, A. A., Leonov, A. V., Kurmaev, E. Z., Kukharenko, A. I., Zhidkov, I. S., Cholakh, S. O. Cu-CeO 2 nanocomposites: mechanochemical synthesis, physico-chemical properties, CO-PROX activity. *J. Nanoparticle Res.* **18**, 344–359 (2016).
180. Maeda, Y., Akita, T. & Kohyama, M. High Activity of Gold/Tin-Dioxide Catalysts for Low-Temperature CO Oxidation: Application of a Reducible Metal Oxide to a Catalyst Support. *Catal. Letters* **144**, 2086–2090 (2014).
181. Kondrat, S. A., Shaw, G., Freakley, S. J., He, Q., Hampton, J., Edwards, J. K., Miedziak, P. J., Davies, T. E., Carley, A. F., Taylor, S. H., Kiely, C. J., Hutchings, G. J. Physical mixing of metal acetates: a simple, scalable method to produce active chloride free bimetallic catalysts. *Chem. Sci.* **3**, 2965–2971 (2012).
182. Zhou, M., Zhao, J., Zhang, P., Chen, N. & Yang, S. Solvent-free and rapid synthesis of mesoporous Pt-iron oxide catalysts: Via mechanochemical assembly. *Catal. Sci. Technol.* **9**, 3907–3913 (2019).
183. Danielis, M., Colussi, S., de Leitenburg, C., Soler, L., Llorca, J., Trovarelli, A. The effect of milling parameters on the mechanochemical synthesis of Pd-CeO 2 methane oxidation catalysts. *Catal. Sci. Technol* **9**, 4232–4238 (2019).
184. Danielis, M., Betancourt, L. E., Orozco, I., Divins, N. J., Llorca, J., Rodríguez, J. A. & Senanayake, S. D., Colussi, S., Trovarelli, A. Methane oxidation activity and nanoscale characterization of Pd/CeO2 catalysts prepared by dry milling Pd acetate and ceria. *Appl. Catal. B Environ.* **282**, 119567 (2021).
185. Mussio, A., Danielis, M., J. Divins, N., Llorca, J., Colussi, S., Trovarelli, A. Structural Evolution of Bimetallic PtPd/CeO2 Methane Oxidation Catalysts Prepared by Dry Milling. *ACS Appl. Mater. & Interfaces* **13**, 31614–31623 (2021).

# 2. Experimental

The aim of this chapter is to briefly describe the materials synthesized in this thesis and the methods of characterization used. Most of the experiments were conducted in our laboratories. The NEXAFS and XPS analysis were conducted in the Advanced Photoelectric Effect – High Energy (APE-HE) beamline of Elettra synchrotron of Trieste. The HRTEM experiments were performed at the Universitat Politècnica de Catalunya, in Barcelona.

## 2.1. Material Synthesis.

### 2.1.1. Synthesis High Surface Area (HSA) cerium oxide.

100 mL of 1.25M CAN (TIAG) solution, were prepared by dissolving the appropriate amount of salt in deionized water, and then transferred in a 1 liter three-necked balloon. To the said solution, 260 mL of 0.4 $NH_3$ (Sigma-Aldrich) solution were added dropwise under constant and gentle magnetic stirring, reaching a pH of 0.5. This particular value of pH was defined by Ikeda-Ohno[1] as a "critical pH" in a work aimed to the understanding of the nanocrystalline ceria evolution in Ce(IV) solution. At this value, the pH value became transiently unchanged regardless the addition of base and this was related to the formation of a fine colloidal suspension of ceria nanoparticles. The final system appeared of a limpid orange color and, accordingly with what described by Ikeda-Ohno[1], consisted of a colloidal suspension of very fine nanocrystals. The obtained system was heated to reflux (100°C). During the heating, the color of the solution changed from orange to yellow, maintaining unaltered the clarity of the system. As the reflux started, the precipitation of a yellow solid occurred. Starting from this point the system was left in reflux conditions for 4 hours in order to age the precipitated solid (Figure 1).

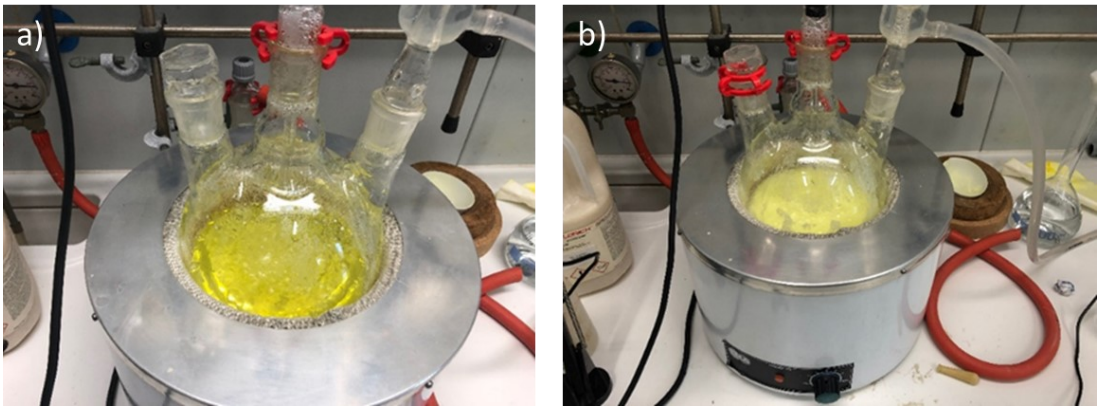


**Figure 1:** comparison of the system before (a) and after (b) the start of the reflux.

The system was then cooled at room temperature and centrifuged to recover the yellow solid. A small aliquot (approximately 1g) of the precipitate was calcined at 400°C in order to determine the $CeO_2$ percentage, which demonstrated to be of approximately 62-64%. The remaining cake was dispersed in a 2M $NH_3$ solution in order to obtain a $CeO_2$ concentration of 48g/L, transferred in a Teflon vessel and subsequently treated in hydrothermal conditions of 180°C for 1 hour. The obtained solid was filtered and washed with deionized water before being calcined at 350°C for 6 hours. Subsequent calcinations at higher temperatures were performed starting from the calcined at 350°C powders and all the calcinations lasted 6h.

The described procedure led to an unprecedented surface area of 337 $m^2/g$ after calcination at 350°C and to high values of surface area also for higher calcination temperatures, as reported in Table 1.

**Table 1:** morphological characteristics of the synthesized cerium oxide.

| Calcination Temperature (°C) | BET Surface Area ($m^2/g$) | Average Pore Diameter (Å) | Mean Pore Volume ($cm^3/g$) | Average Particle Size (nm)[a] |
|---|---|---|---|---|
| 350 | 337 | 43.23 | 0.281 | 4 |
| 500 | 230 | 34.56 | 0.247 | 5 |
| 550 | 204 | 75.87 | 0.480 | 6 |
| 800 | 56 | 178.62 | 0.326 | 18 |
| 900 | 37 | 233.73 | 0.240 | 27 |
| 1000 | 18 | 325.07 | 0.233 | 40 |
| 1200 | 5 | 599.61 | 0.086 | 65 |

[a] : calculated according to Scherrer's equation from the line broadening of $CeO_2$ (111)

## 2.1.2. Synthesis of the $Ni/CeO_2$ catalysts

$Ni/CeO_2$ catalysts with 4 wt % Ni loadings were prepared on a commercial high surface area ceria (Umicore) and, in some experiments, a high surface area ceria (HSA) prepared in our laboratories with a synthetic procedure that will be described in the following pages, calcined in static air at 800°C prior to metal deposition and with a specific surface area of 64 $m^2/g$ and 56 $m^2/g$, respectively. Two series of catalysts were prepared from two different Ni hydrated salts, namely $Ni(NO_3)_2 \cdot 6H_2O$ and $NiCl_2 \cdot 6H_2O$. Reference catalytic materials were prepared by conventional incipient wetness impregnation (IW). For the preparation of the reference IW catalysts, an aqueous solution of the nickel precursor (Aldrich, 99,999%) was used in appropriate amount to reach the desired nominal Ni loading. The solution was impregnated drop by drop on the ceria support with the help of a mortar and a pestle to homogenize the powders. The catalyst was then dried at 100°C overnight and calcined at 500°C for 1 hour in static air. The milled samples were synthesized with the following procedure: the Nickel precursor and the Cerium oxide were pre mixed in a sample holder in order to homogenize the mixture prior to the milling, then the mixture was transferred in a 15 mL zirconia jar and milled with a single ball made of zirconia (15 mm in diameter, 10 g weight) at a constant frequency (15 Hz) with a variable time that goes from 5 (M05) to 60 minutes (M60) by using a Fritsch Pulverisette 23 minimill. For the long-time milled catalysts M40 and M60 subsequent 20 min steps were carried out to avoid agglomeration. A zero-time milled sample was obtained from the mixing the starting materials inside the jar without the ball (Loose Contact, LC) at a frequency of 15 Hz for 10 minutes. After milling the samples were calcined at 500°C for 1 hour.

## 2.1.3. Synthesis of the $CeO_2$/CuO catalysts

A reference impregnated catalysts (I $CeO_2$ CuO 2080) with a 20% weight of $CeO_2$ was synthesized *via* impregnation technique. In a 50 ml Becher a proper amount of Cerium nitrate ($Ce(NO_3)_3 \cdot 6H_2O$) (Treibacher Industrie AG) was dissolved in 45 mL of ethanol (Sigma-Aldrich). In this solution the proper amount (750 mg) of CuO was dispersed. The resulting suspension was gently heated (60°C) until complete evaporation of the solvent. The resulting black powder was dried at 100°C for 12 hours prior to calcination at 400°C for 1 hour. The milled catalysts were prepared by premixing the desired amounts of pre-calcined CuO and $CeO_2$ powders. The CuO and the $CeO_2$ were calcined at 600°C and 500°C respectively. We used an industrial cerium oxide provided by Umicore pre-calcined at 500°C for 6 hours with an active surface are of 120 $m^2/g$ and one prepared in our laboratories (HSA) pre-calcined at 350°C for 6 hours with a surface area of 307 $m^2/g$. The cerium oxide weight content was increased from 20% to 80%. The homogenized powders were transferred in a 15mL zirconia jar together with a single zirconia ball (15 mm in diameter, 10 g weight). The powders were milled for 10 minutes at a frequency of 15Hz from using a Fritsch Pulverisette 23 minimill. After the milling step the powders were collected with the help of a brush to remove the powders from the jar. No calcination step was performed since we started from pre-calcined CuO and $CeO_2$.

# 2.2. Characterization

## 2.2.1. Surface Area and Pore Size Measurements

Evaluation of the catalysts surface area was carried out in a Micrometrics Tristar Porosimeter by analyzing N2 adsorption isotherms at -196 °C using the Brunauer-Emmett-Teller (BET) method[2]. Pore size measurements were performed in the same setup using the Barrett-Joyner-Halenda method (BJH) on desorption isotherms. Catalyst samples were degassed at 150°C for 1.5 hours prior to analysis.

## 2.2.2. Temperature Programmed Reduction (TPR)

TPR experiments were carried out in a Micromeritics AutoChem II 2920 analyzer on 50 mg of catalysts, loaded in a U-shaped quartz micro-reactor. The sample was pretreated in air at 500°C for 1 h, then cooled to room temperature under $N_2$ flow. The analysis was performed under a flowing reducing mixture of 4.5% H2 in N2 (flow rate = 35 ml/min), heating the sample from RT to 800°C at a heating rate of 10 °C/min, then cooled at RT. The experiment was repeated starting from the pre-treatment step.

In the case of $CeO_2$/CuO catalysts the analysis was conducted on 10 mg of sample, that were analyzed, without pre-treatment, in the same reduction mixture following the same heating ramp.

## 2.2.3. Thermo-gravimetric Analysis (TGA)

To determine the quantity of formed carbon after the catalytic test in DRM in the Ni/$CeO_2$ catalysts, thermogravimetric analyses were carried out in a Q500 - TA Instruments thermobalance. Usually, 10-15 mg of sample were loaded on a platinum pan with 60 ml/min of gas flowing horizontally over the sample surface. The sample was gradually heated at 10 °C/min from RT to 800°C, then cooled to 100 °C. Weight loss profiles have been measured under synthetic air (20.9% O2/N2).

## 2.2.4. X-ray Diffraction Analysis (XRD)

XRD analysis was performed *ex-situ* in a Philips X'Pert diffractometer equipped with an X'Celerator detector using Ni-filtered Cu Kα radiation (λ = 1.542 Å). Data were recorded in the 2θ range of 20-100° with a step size of 0.02° and a counting time per step of 40 s. Fitting of the crystalline phases was performed using the Philips X'Pert HighScore program. Particle size was estimated using the Scherrer equation[3] using the {111} ceria peak at 2θ = 28.61° and the {111} CuO peak at 38.73° and the instrumental peak widening correction measured for a silica standard.

*In-situ* XRD analysis was performed using a Anton Paar high temperature cell in order to follow the redox process of $Ni/CeO_2$ (see 2.2.3. section)

## 2.2.5. High Resolution Transmission Electron Microscopy (HRTEM)

Microstructural characterization by High Resolution Transmission Electron Microscopy (HRTEM)[4] of the $Ni/CeO_2$ samples was carried out at the Universitat Politècnica de Catalunya. Images were collected at 200 kV with a JEOL JEM-2010F electron microscope equipped with a field emission gun. The point-to-point resolution was 0.19 nm and the resolution between lines was 0.14 nm. Samples were dispersed in alcohol in an ultrasonic bath, and a drop of supernatant suspension was poured onto a holey carbon-coated grid.

## 2.2.6. X-Ray Photoelectron Spectroscopy (XPS)

Ex-situ X-Ray Photoelectron Spectroscopy experiments were performed at the Advanced Photoelectric Effect – High Energy (APE-HE) beamline at Elettra Synchrotron in Trieste (Italy). The measurements were done exploiting a conventional non monochromatized X-Ray source (Al Kα= 1486 eV) with a hemispherical electron energy analyzer, in a dedicated chamber of the NFFA UHV MBE-cluster system[5]. The powders have been glued on the sample holder using a conductive silver paste. The samples have been positioned at 45°with respect to the incident beam, probing an area of ~ 1 $mm^2$ and a depth of ~ 1 nm. The Ce 3d, Ni 2p and O 1s spectra have been acquired using a pass energy of 30 and a dwell time of 1000 ms; they have been aligned in energy using the Au 4f spectra of a reference Au foil positioned just above the sample. The data analysis has been performed using Origin© Software and CasaXPS©. The fitting procedure for XPS spectra has been made using a Shirley background type and a Levenberg-Marquardt Algorithm (LMA).

## 2.2.7. Near Edge X-Ray Absorption Fine Structure Spectroscopy (NEXAFS)

X-Ray absorption spectra at the Ni $L_{2,3}$ edges have been measured at the APE-HE beamline at the ELETTRA synchrotron radiation source[6]. The NEXAFS spectra have been acquired using the Total Electron Yield (TEY) detection mode, allowing a probing depth of ~ 5 nm. The energy resolution of these spectra is about 0.1 eV. The samples, in the form of powders, have been glued on the sample holder using conductive silver paste and then loaded on the manipulator of the APE-HE chamber (in UHV conditions). The sample was oriented at 45° with respect to the incident beam, probing an area of ~ 150 $\mu m^2$. All the data treatment, involving spectra normalization and energy alignment, was performed using the Origin© Software.

## 2.2.8. *Operando* Soft X-Ray NEXAFS Spectroscopy at ambient pressure

The experiments were performed at the APE-HE beamline at Elettra Synchrotron in Trieste (Italy), exploiting an innovative home-made reaction cell[7]. The experimental setup is designed to acquire NEXAFS spectra continuously at 1 bar, in TEY mode. A maximum of two gas mixtures could be introduced in the reaction cell; a micro-GC (Agilent), equipped with a Volamine column, connected to the output of the cell, allows to detect the gas products in real time during the NEXAFS spectra acquisition (Figure 2).

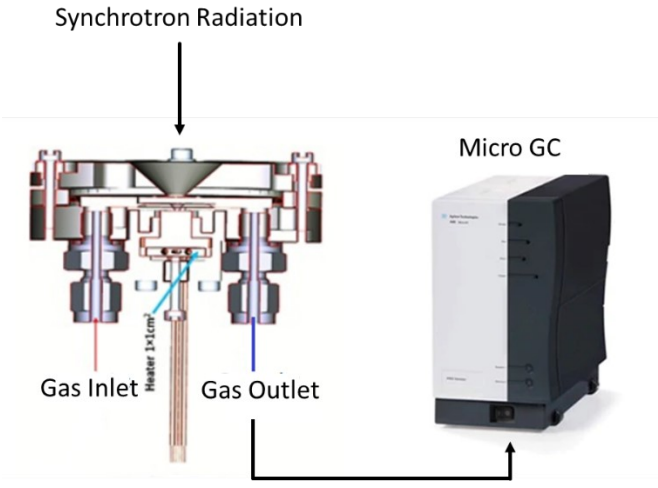


**Figure 2:** experimental setup of the *in-operando* NEXAFS experiment.

The gas line is controlled by three flowmeters, calibrated to a maximum total flow of 50 ml/min. For the study of methane activation, the sample was exposed to a gas mixture containing 10 vol% CH4 in He for 1 hour, then methane was removed for 10 minutes before being exposed to a 5 vol% $O_2$ in He atmosphere for 20 minutes.

## 2.2.9. Diffuse Reflectance Infrared Fourier Transform Spectroscopy (DRIFTS)

*In-situ* DRIFTS spectra were collected in absorbance mode using a Thermo Fisher Nicolet is-50 FTIR spectrometer equipped with a Pike cell (Figure 3).

**Figure 3:** Optical geometry of the DiffusIR accessory (left) and low temperature chamber shown with connections (right).

*In-situ* methane activation/oxidation were carried out to investigate the adsorbed species on the catalysts surface and their stability in oxidizing atmospheres, following the scheme of Figure 4. Powder samples were loaded in the reaction cell under 80 ml/min total gas flow. Before reaction, the sample was pretreated in pure Helium at 300°C for 15 minutes. After cooling at 250°C the reaction temperature, the background was collected with 100 scans. For the study of methane activation, the sample was exposed to a gas mixture containing 10 vol% $CH_4$ in He for 1 hour, then methane was removed for 10 minutes before being exposed to a 5 vol% $O_2$ in He atmosphere for a time that depended from the characteristics of the different tested samples.

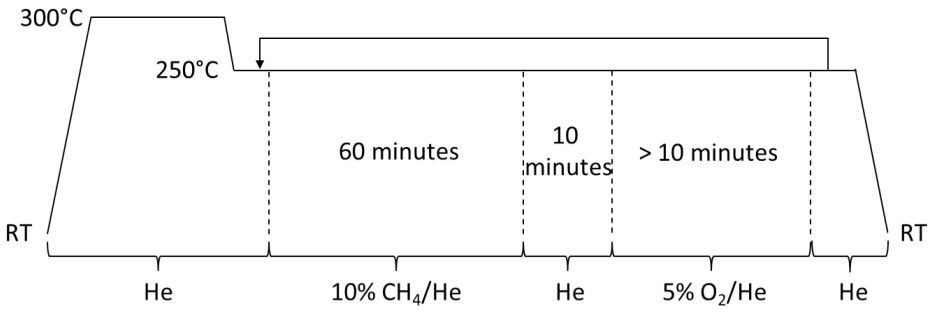


**Figure 4:** Experimental detail of the in-situ DRIFTS methane oxidation (MO) tests. Heating/cooling ramps: 10 °C/min; reaction mixture: 10%$CH_4$/5%$O_2$/He.

# 2.3. Catalytic Test

## 2.3.1. Dry Reforming Catalytic Tests

The dry reforming catalytic tests were conducted accordingly with previously reported procedures[8]. In detail, at atmospheric pressure in a fixed-bed reactor (i.d. = 4 mm) using 0.08 g of catalyst in powder form (mixed with quarts in a 1:1 ratio). The temperature of the reaction was controlled by a thermocouple placed a few millimeters on the top of the sample. All the temperature ramps used were of 10°C/min. Prior to catalytic test the sample was reduced in hydrogen at 800°C for 1 hour. Catalytic experiments were conducted in the temperature range of 550-800°C with steps of 50 °C on the catalyst previously reduced under hydrogen at 800°C for 1 h (Figure 5).

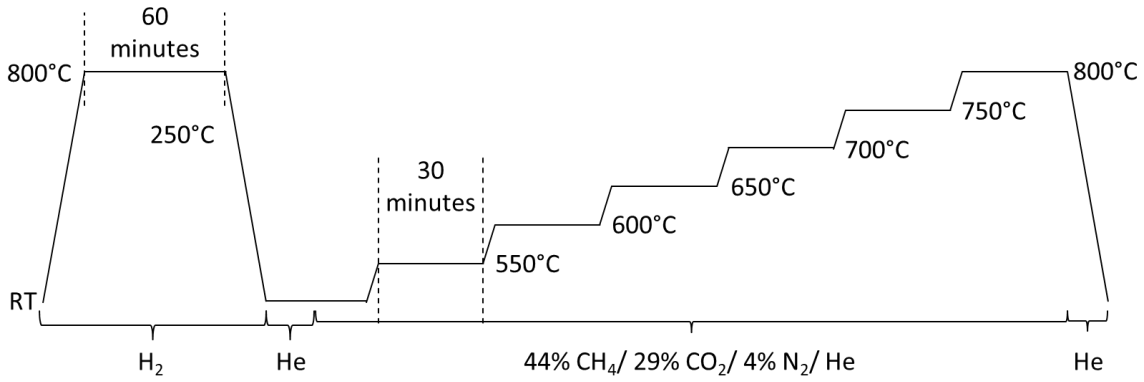


**Figure 5:** Experimental detail of the DRM catalytic tests.

The total volumetric flow was 82 mL/min with a $CO_2/CH_4$ ratio of 3:2, in order to simulate the typical composition of biogas sourced from biogenic waste. Nitrogen was used as internal reference. The composition of the reactor outlet gases mixture (CO, $H_2$, $CO_2$, and $CH_4$) was analyzed with a gas chromatograph (GC, Agilent model 8860) equipped with two columns (a molecular sieve and carboxen column) and with a thermal conductivity detector (TCD). Below an image of the plant used (Figure 6): gases flows were controlled by a series of flow meters (Brooks), the gases were mixed before the inlet of reactors, six ways valve allow to bypass the reactor and feed directly the reactant mixture for a check of composition before the catalytic test. All lines can be purged with an inert gas, if necessary.

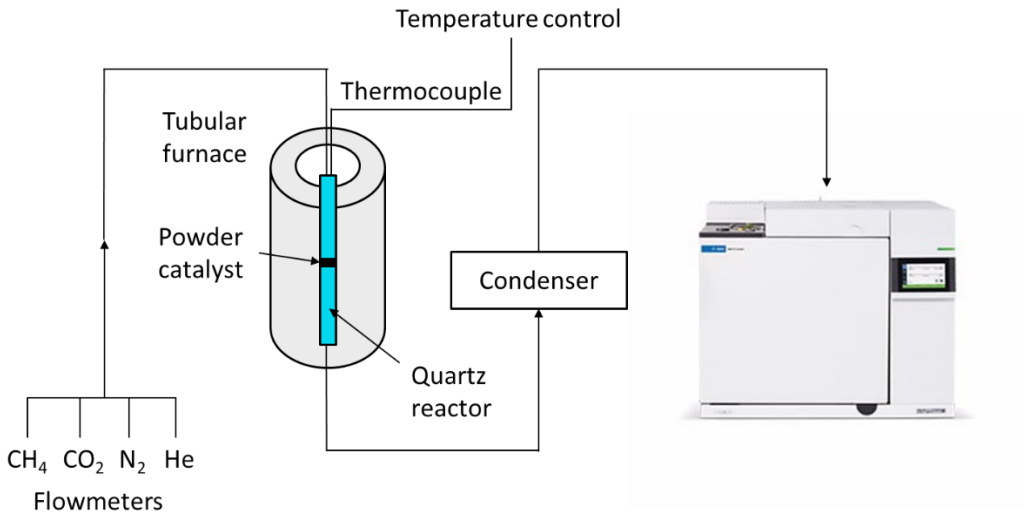


**Figure 6:** Experimental setup for the Dry Reforming of Methane test.

The reaction mixture was injected to the GC after 30 min of isothermal conditions, in order to measure in steady state conditions. The time on stream experiments were conducted right after the catalytic test described above after cooling at 750°C, in isothermal conditions for 70 hours. The conversions of $CO_2$ and $CH_4$ and $H_2$/CO ratios were calculated according to the following formulas, the factor β to consider the changes of flow rate during the reaction.

$$\beta = [N_2]in/[N_2]out$$

$$X[CH_4]\% = \{[CH_4]in \times ([CH_4]out \times \beta)\}/[CH_4]in) \times 100$$

$$X[CO_2]\% = \{[CO_2]in \times ([CO_2]out \times \beta)\}/[CO_2]in) \times 100$$

$$H_2/CO = [H_2]out/[CO]out$$

# 2.4. References


1. Ikeda-Ohno, A., Hennig, C., Weiss, S., Yaita, T. & Bernhard, G. Hydrolysis of tetravalent cerium for a simple route to nanocrystalline cerium dioxide: An in situ spectroscopic study of nanocrystal evolution. *Chem. - A Eur. J.* **19**, 7348–7360 (2013).
2. Brunauer, S., Emmett, P. H. & Teller, E. Adsorption of Gases in Multimolecular Layers. *J. Am. Chem. Soc.* **60**, 309–319 (1938).
3. Jenkins Ron, S. R. L. *X-Ray Powder Diffractometry*. (Wiley, 2012).
4. Maiti, S. *et al.* Combustion synthesized copper-ion substituted FeAl2O4 (Cu0.1Fe0.9Al2O4): A superior catalyst for methanol steam reforming compared to its impregnated analogue. *J. Power Sources* **304**, 319–331 (2016).
5. Torelli, P. *et al.* Experimental setup for high energy photoemission using synchrotron radiation. *Rev. Sci. Instrum.* **76**, (2005).
6. Panaccione, G. *et al.* Advanced photoelectric effect experiment beamline at Elettra: A surface science laboratory coupled with Synchrotron Radiation. *Rev. Sci. Instrum.* **80**, (2009).
7. Castán-Guerrero, C. *et al.* A reaction cell for ambient pressure soft x-ray absorption spectroscopy. *Rev. Sci. Instrum.* **89**, (2018).
8. Pappacena, A., Razzaq, R., De Leitenburg, C., Boaro, M. & Id, A. T. inorganics The Role of Neodymium in the Optimization of a Ni/CeO 2 and Ni/CeZrO 2 Methane Dry Reforming Catalyst. *inorganics* **6**, 39–54 (2018).

# 3. Activity and stability of methane dry reforming $Ni/CeO_2$ catalysts prepared via mild energy ball milling synthesis

## 3.1. Abstract

$Ni/CeO_2$ catalysts are suitable systems for reforming reaction due to their good activity, stability and affordability. However, their catalytic activity is strongly dependent on the interaction between metal and support. Mechano-synthesis via ball milling has been recently proved to be a valid approach to promote specific and strong metal interactions in ceria-based catalyst. Moreover, this technique matches with the principles of green chemistry being solvent-free and of easy scalability. In this thesis the synthesis of $Ni/CeO_2$ catalysts via ball milling starting form cheap hydrated metal salts is proposed, with a deep investigation on the milling time, in order to give information that will be useful for future attempts of synthesis of ceria-based catalysts with this synthetic procedure. All the synthesized catalysts have been characterized by means of BET, XRD, TPR and tested in DRM reaction and compared to a reference incipient wetness (IW) catalyst. The best performing catalysts have been characterized more deeply with HRTEM and XPS. The catalytic tests conducted revealed that the mechanical action was responsible for an enhanced catalytic activity compared to the reference IW, independently from the starting precursor. The milled catalyst obtained from the nitrate precursor also showed an enhanced stability with respect to the impregnated sample. The results of the XPS analysis showed the presence of an unpredicted profile for cerium, which can be associated with the formation of few layers of a $Ni_xCeO_{2-x}$ phase localized in the surface of the milled catalysts. The XPS analysis resulted in good agreement with the HRTEM results that showed the presence of a surface "rugosity" potentially related to a particular arrangement of Ni, O and Ce atoms.

# 3.2. Introduction

In Chapter 1 we discussed the potentiality of the Dry Reforming of Methane (DRM), together with the main issues of this process, mainly represented by the deactivation of the catalysts due to the coke formation. An approach to overcome these issues is the use of noble metals as catalysts, but this would make the process not economically competitive for a development to industrial scale[1–4]. Nickel, in contrast to noble metals, is an economic and a relatively abundant element which has a particular activity in DRM[2–5]; however it is very prone to coke formation[6–8]. Several approaches have been investigated to avoid this problem, such as the alloying Ni to other metals[9–13] or its dispersion it on active supports obtaining a strong metal-support interaction, which contributes to reduce the accumulation of carbon[14–16]. One of the most popular and successful support used is the cerium oxide . In fact, this oxide has peculiar oxygen transfer properties, able to limit the carbon buildup and thus improving stability of catalysts[17–20]. Therefore, $Ni/CeO_2$ catalysts are amongst the most studied systems for DRM[17,21] which, however, need the utilization of some synthetic strategies in order to improve both the nickel dispersion and the mobility of oxygen vacancies on its surface. It was demonstrated that the formation of Ni-O-Ce interactions improved the catalytic performance in terms of both activity and durability of the catalyst since the confinement of Ni atoms/particles in the support boosted the synergy between the two materials[22–26,27]. Ball milling is a green synthetic technique[28] which has been recently investigated for the synthesis of heterogenous catalysts[29]. It was demonstrated that the mechanical energy provided from this kind of synthesis favors the intimate interaction between metal and support thus giving rise to the formation of metastable structures that showed superior catalytic activity compared to catalysts synthesized with conventional procedures[24,29,30]. Zhang et al.[24] reported that the synthesis via wet-ball milling led to a nanoconfinement of Ni particles into the support thus giving rise to active and stable $Ni/CeO_2$ catalysts. However, they obtained their catalyst after 10 hours of wet High Energy Ball Milling technique starting from skeletal Nickel as precursor which has the main drawback of being highly pyrophoric. Literature reported that when exist an intrinsic attitude to interact between the metal and support (as between Pd and $CeO_2$) it is possible promote unusual metal-support interaction by using mild-energy of milling also starting from hydrated metal-salt precursors[30,31]. Nickel is reported to be a transition metal with a strong affinity with cerium oxide[17,32] and in this work we proposed dry-Mild Energy Ball Milling approach for the synthesis of $Ni/CeO_2$ for the DRM reaction. The aim of this work was to investigate the enhanced metal-support interaction induced by the milling process and to understand its role in the improved catalytic activity and stability. For this purpose two different series of catalysts, derived from two Nickel salts, $Ni(NO_3) \cdot 6H_2O$ and $NiCl_2 \cdot 6H_2O$, were obtained by varying the milling time from zero (Loose Contact, LC) to 60 minutes (M60). The zero-time sample consists of a simple mixing of the two precursors without the milling action and it is expected to be an heterogenous mixture of the two staring materials.

The effect of precursors and milling time was carefully analyzed in order to come up with some general principles that can guide the formulation and synthesis of a broader class of materials from ceria (or ceria-based materials) and transition-metal hydrated salt precursors.

# 3.3. Experimental

## 3.3.1. Catalysts Synthesis

$Ni/CeO_2$ catalysts with 4 wt % Ni loadings were prepared on a commercial high surface area ceria (Umicore) and a high surface area ceria (HSA) prepared in our laboratories, calcined in static air at 1073 K prior to metal deposition and with a specific surface area of 63 and 48 $m^2/g$, respectively. Samples were prepared by dry mechanochemical synthesis using the solid hydrated salts $Ni(NO_3)_2x6H_2O$ and $NiCl_2x6H_2O$ as precursors (Sigma Aldrich) and by standard incipient wetness impregnation using an aqueous solution obtained from the same precursors, following established synthesis procedures[33]. Briefly, for the milling synthesis, the Nickel precursor and the cerium oxide were pre mixed in a sample holder in order to homogenize the mixture prior to the milling, then the mixture is transferred in a 15 mL zirconia jar and milled with a single ball made of zirconia (15 mm in diameter, 10 g weight) at a constant frequency (15 Hz) and variable time from 5 (M05) to 60 minutes (M60) using a Fritsch Pulverisette 23 minimill. For the long-time milled catalysts M40 and M60 subsequent 20 min steps of milling were carried out to avoid agglomeration. A zero-time milled sample was obtained from the mixing inside the jar without the ball (Loose Contact, LC) at a frequency of 15 Hz for 10 minutes. After milling the sample is calcined at 773 K for 1 hour. For the incipient wetness (IW) synthesis, an appropriate amount of the nickel salt solution was used to wet the ceria powders, which were dried at 373 K for 15 h before calcination at 773 K. Prepared samples are denoted as reported in Table 1.

**Table 1:** list of the prepared $Ni/CeO_2$ samples and corresponding labels.

| | **Precursor** | |
|---|---|---|
| **Catalyst** | **$NiCl_2 \cdot 6H_2O$** | **$Ni(NO_3)_2 \cdot 6H_2O$** |
| Incipient Wetness | IWC | IWN |
| Loose Contact | LCC | LCN |
| Milled at a frequency of 15Hz for 5 minutes | M05C | M05N |
| Milled at a frequency of 15Hz for 10 minutes | M10C | M10N |
| Milled at a frequency of 15Hz for 20 minutes | M20C | M20N |
| Milled at a frequency of 15Hz for 30 minutes | M30C | M30N |
| Milled at a frequency of 15Hz for 40 minutes | M40C | M40N |
| Milled at a frequency of 15Hz for 60 minutes | M60C | M60N |

## 3.3.2. Catalysts Characterization

Characterization of the materials was carried out by means of Brunauer−Emmett− Teller (BET) surface area measurements, in-situ X-ray diffractometry, high-resolution transmission electron microscopy (HRTEM), Temperature-Programmed Reduction (TPR), x-ray photoemission spectroscopy (XPS) and Near-Edge X-ray Adsorption Fine Structure (NEXAFS) tests. The evaluation of carbon percentage after catalytic tests was performed by terms of Thermo Gravimetric Analysis (TGA). For details on the use of the above techniques see chapter 2.

## 3.3.3. Powder Samples Activity Tests

The dry reforming tests were conducted at atmospheric pressure in a fixed-bed reactor (i.d. = 4 mm) using 0.08 g of catalyst in powder form (mixed with quarts in a 1:1 ratio). The temperature of the reaction was controlled by a thermocouple placed a few millimeters on the top of the sample. All the temperature ramps used were 10°C/min. According to an established procedure, the sample was reduced in hydrogen at 800°C for 1 hour prior to the catalytic test[34]. Catalytic experiments were conducted in the temperature range 550-800°C with steps of 50 °C. The total volumetric flow rate was 82 mL/min with a $CO_2/CH_4$ ratio of 3:2, in order to simulate the typical composition of biogas from biogenic waste. Nitrogen was used as internal reference. The total composition of the inlet reactive mixture was 44% $CH_4$/ 29% $CO_2$/ 4% $N_2$/ He. The composition of the reactor outlet gas mixture (CO, $H_2$, $CO_2$, and $CH_4$) was analyzed with a gas chromatograph (GC, Agilent model 8860) equipped with two columns (a molecular sieve and carboxen column) and with a thermal conductivity detector (TCD). The reaction mixture was analyzed in steady state conditions after 30 min of isotherm at the desired temperature. The time on stream experiments were conducted right after the catalytic test cooling the sample at 750°C, and keeping it in atmosphere of reaction at this temperature for 70 hours The conversions of $CO_2$ and $CH_4$ and $H_2/CO$ ratios were calculated according to the formulas reported in Chapter 2; for details see chapter 2.3.1.

# 3.4. Results and Discussion

## 3.4.1. Textural and Morphological properties

Morphological properties of the materials investigated are summarized in Table 2. It is possible to observe a drop in surface area, pore volume and pore diameter in all the catalysts after the deposition of the metallic phase, independently from the synthetic technique. In general in the chloride-derived catalysts ($Cl^-$), we observed a major drop compared to the nitrate-derived-catalysts ($NO_3^-$). This difference could be related to the different interaction of the anion of the Nickel salt with the support during the deposition. Comparing the two synthetic techniques, independently from the metal salt, it is possible to observe a more consistent drop in the IW catalysts in comparison to the milled ones. This difference is probably attributable to the characteristics of the impregnation procedure, in which the aqueous solution of the metal precursor should fill the pores of the support more effectively than is expected in the ball milling procedure, which uses undissolved salts directly. Concerning the milled samples we observed, independently from the nickel precursor used, a constant decrease in pore volume and pore diameter with increasing milling time, with the surface area that remained constant. This gradual drop could have been related to the gradual disaggregation of the support clusters due to the mechanical action.

**Table 2:** Morphological and textural properties of $CeO_2$ and investigated catalysts obtained from commercial HSA $CeO_2$.

| **Precursor** | **$NiCl_2 \cdot 6H_2O$** | | | **$Ni(NO_3)_2 \cdot 6H_2O$** | | |
|---|---|---|---|---|---|---|
| | **BET ($m^2/g$)** | **Pore volume ($cm^3/g$)** | **Pore diameter (Å)** | **BET ($m^2/g$)** | **Pore volume ($cm^3/g$)** | **Pore diameter (Å)** |
| $CeO_2$ | 64 | 0.410 | 179 | 64 | 0.410 | 179 |
| IW | 48 | 0.147 | 90 | 57 | 0.235 | 129 |
| LC | 54 | 0.304 | 159 | 56 | 0.326 | 166 |
| M05 | 51 | 0.309 | 169 | 56 | 0.293 | 155 |
| M10 | 50 | 0.241 | 141 | 58 | 0.248 | 136 |
| M20 | 50 | 0.240 | 144 | 58 | 0.256 | 140 |
| M30 | 50 | 0.218 | 124 | 57 | 0.253 | 137 |
| M40 | 50 | 0.161 | 98 | 57 | 0.218 | 118 |
| M60 | 50 | 0.166 | 101 | 58 | 0.205 | 112 |

## 3.4.2. XRD and HRTEM Analysis

The XRD experiments conducted in the calcined samples of the different catalysts of both the series showed the typical diffraction peaks of the fluorite phase of $CeO_2$ and the peaks relative to Face-Centered Cubic (FCC) phase of NiO (Figure 1):

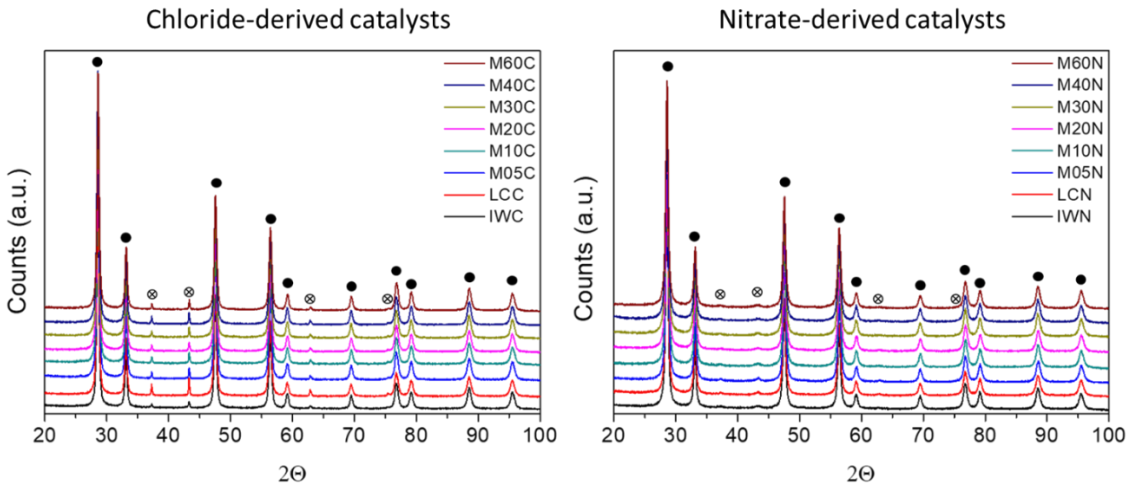


**Figure 1:** XRD diffraction patterns of the catalysts obtained from the $Cl^-$ (left) and $NO_3^-$ (right) series. Full circles (●) are related to the $CeO_2$ fluorite phase while the crossed circles (⊗) to the FCC phase of NiO.

We observed the presence of very large and broad peaks of the NiO phase in the $NO_3^-$ catalysts, this could be related to a nanometric/sub-nanometric dispersion of the active phase. On the contrary, the $Cl^-$ catalysts showed sharper peaks, indicating a larger particle size in these catalysts respect to the $NO_3^-$ analogues . This effect is well depicted in Figure 2, where three representative samples from the two series are considered: the reference IW, the LC and the M10 as a representative catalyst obtained with the mechanochemical synthetic technique.

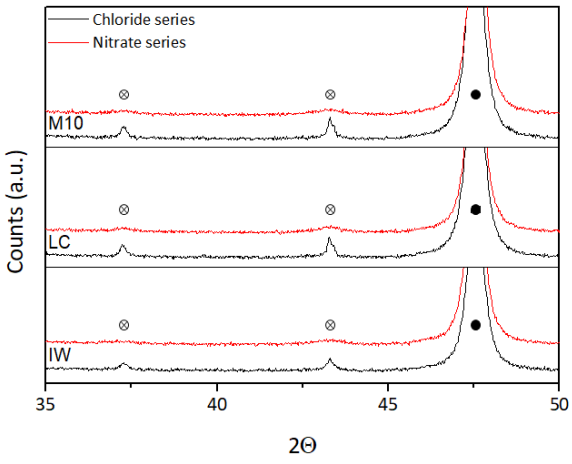


**Figure 2:** Detail of the 35°-50° 2Θ window of figure 1. Full circles (●) are related to the $CeO_2$ fluorite phase while the crossed circles (⊗) to the FCC phase of NiO.

The presence of broad peaks reflects a small dimension of the metal phase on the support. It is possible to see that this phenomenon was observed independently from the synthetic method or milling time, indicating a better dispersion of the NiO phase in the catalysts of the nitrate series. Similar differences in the nickel particle size depending on the precursor were observed in different Nickel supported catalysts[35,36]. Taking into account that the same results were also found for the LC samples, which consist of a heterogeneous mixture of $CeO_2$ and NiO, it was inferred that the difference in NiO particle size is due to the different decomposition mechanism of the two salts[37].

HRTEM analyses conducted on the representative M10 catalysts obtained from both the two series (Figure 3) confirmed the XRD results, since larger Ni domains were observed in the M10C sample respect to the M10N. Moreover, it showed that the differences in Ni particle size were maintained after reduction at high temperature (800°C), it is not excluded that the sintering process is influenced by the initial NiO particle size, with a more pronounced effect for the smaller particle. After reduction, the Ni particle size of the $NO_3^-$ catalysts varied from 6 to 12 nm for the IWN sample and from 8 to 15 nm for the LCN sample, while it ranged from 5 to 6 nm in the M10N sample, which is a remarkable small dimension for high temperature annealed supported metal phases[38]. On the other hand, Ni particle sizes were larger in the corresponding chloride-derived catalysts (8-13 nm, 8-20 nm, 8-15 nm  in IWC, LCC and M10C, respectively).

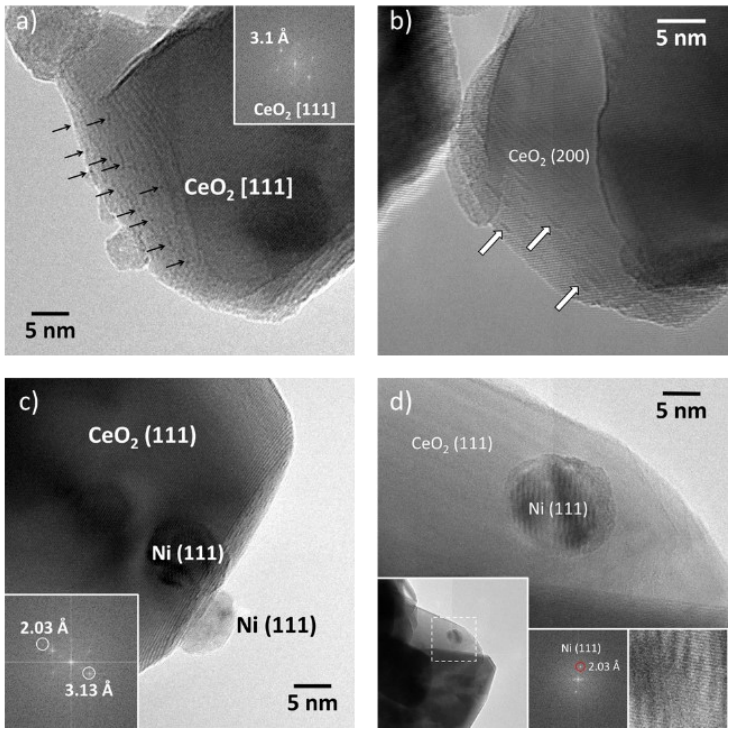


**Figure 3:** HRTEM images of the M10 catalysts obtained from the nitrate (a, c) and the chloride (b, d side) precursors after calcination at 500°C (up) and after reduction at 800°C (down).

A careful perusal of HRTEM images of calcined M10 samples (Fig.3a and 3b) revealed the presence of a "rugosity" in the surface of the ceria crystallites in which a remarkable dispersion of sub-nanometric Ni entities was detected. This rugosity appeared more enhanced in the nitrate-derived material. The small size of these entities prevented the appearance of clear lattice fringes, and they were identified by contrast. The HRTEM/EDX analysis conducted in the as-prepared M10 sample (prior to calcination at 500°C) showed the presence of the same morphology described above (Figure 4), thus indicating that this morphological pattern is already present after the milling process. The EDX analysis revealed the presence of Ni in addition to the peaks of Ce and O from the support (the Cu signals come from the TEM grid), and we concluded that these entities observed in the calcined sample were ascribable to Ni.

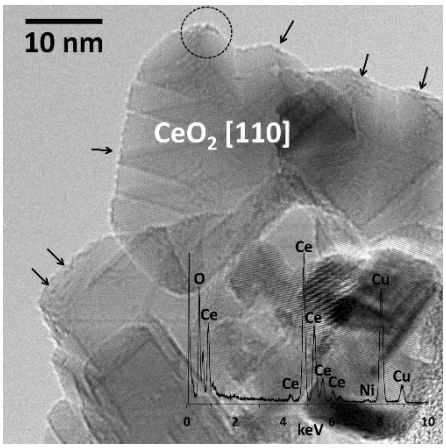


**Figure 4**: HRTEM image and EDX analysis the as-prepared M10 sample (prior to calcination at 500°C). The EDX analysis corresponds to the area enclosed to the circle.

Since the above described rugosity was better evidenced in the M10 sample derived from the nitrate precursor we made a comparison between the IWN, M10N and M40N calcined catalysts of this series (Figure 5) In all samples the presence of ceria crystallites of 10-20 nm was detected together with the presence of some sub-nanometric entities well dispersed on the ceria support. In the milled samples, independently from the milling time, the ceria crystallites presented the described rugosity in which the sub-nanometric particles were visible. Apparently, this rugosity is more pronounced in the M10N sample compared to the M40N and seems to be absent in the IWN sample. From these findings it was possible to conclude that the rugosity observed is a peculiar effect of the mechanochemical synthetic procedure. It is interesting to point out that the rugosity, together with the presence of the sub-nanometric entities, observed in the M10N as-prepared sample, is maintained unaltered after calcination at 500°C, indicating a stability of this peculiar morphology since no sintering of the sub-nanometric Ni entities was observed.

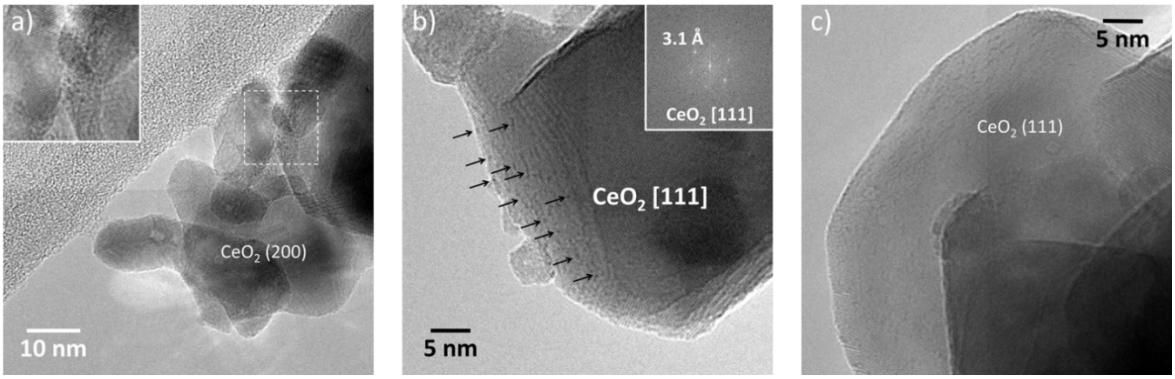


**Figure 5**: HRTEM images of different Nitrate catalysts after calcination at 500°C for 1h; a) IWN; b) M10N; c) M40N.

Looking at the comparison between the M10N and M40N samples before and after calcination (Figure 6), it is possible to see that the reducing treatment had a strong effect on the sample, since a sintering of both ceria and nickel was observed, with ceria particles of 40-60 nm, and Ni nanoparticles, of about 5-6 nm in diameter in the M10 sample and 6-8 nm in the M40 sample. Most of these particles exhibited the typical lattice fringes at 3.13 Å corresponding to the (111) planes of cerium oxide, the lattice fringes at 2.03 Å corresponding to metallic Ni, and lattice fringes at 2.41 Å corresponding to the crystallographic planes of NiO likely formed from the oxidation of metallic Ni in contact with air during sample manipulation. Interestingly, the rugosity and the presence of Ni entities distinguishable from the larger Ni particles were mantained also after reduction at 800°C, indicating once again the stability of this peculiar morphology also in harsher thermal treatments.

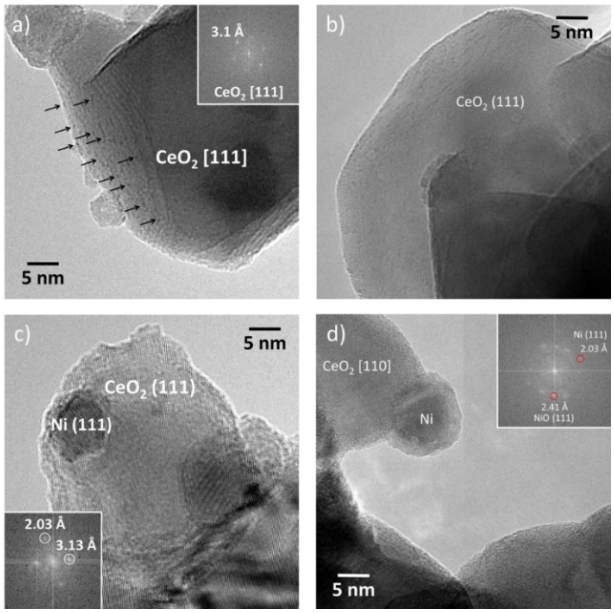


**Figure 6**: HRTEM images of different $NO_3^-$ catalysts before and after reduction at 800°C for 1h; a) M10N before reduction; b) M40N before reduction; c) M10N after reduction; d) M40N after reduction.

## 3.4.3. TPR Analysis

The redox properties of the investigated catalysts in relation to the type of synthesis and milling time were studied by performing two consecutive TPR measurements following the scheme reported in Figure 7. The reason of two oxidation/reduction cycles comes from the necessity to study the material in two different moments: the first cycle gave us information about the as-prepared catalyst after calcination at 500°C, while the second cycle gave us information about the catalyst in the operating conditions, since prior to the catalytic test a reduction in hydrogen at 800°C is performed.

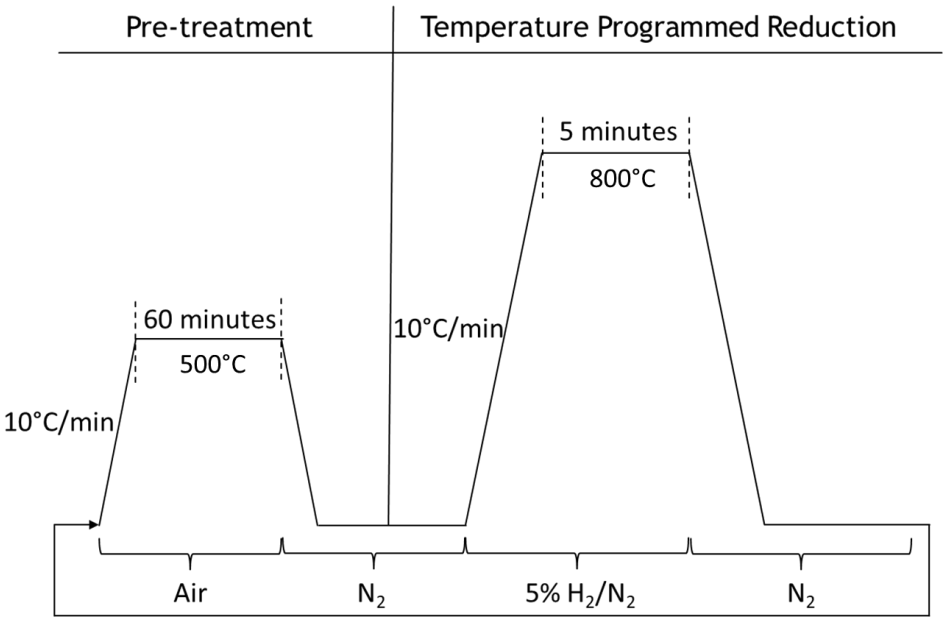


**Figure 7:** Schematic representation of the TPR experiment.

For the sake of clarity, Figure 8 shows only the results of a few representative samples: the reference IW, LC, M10 as an example of a catalyst milled for a short time and M40 as representative of a catalyst milled for a longer time.

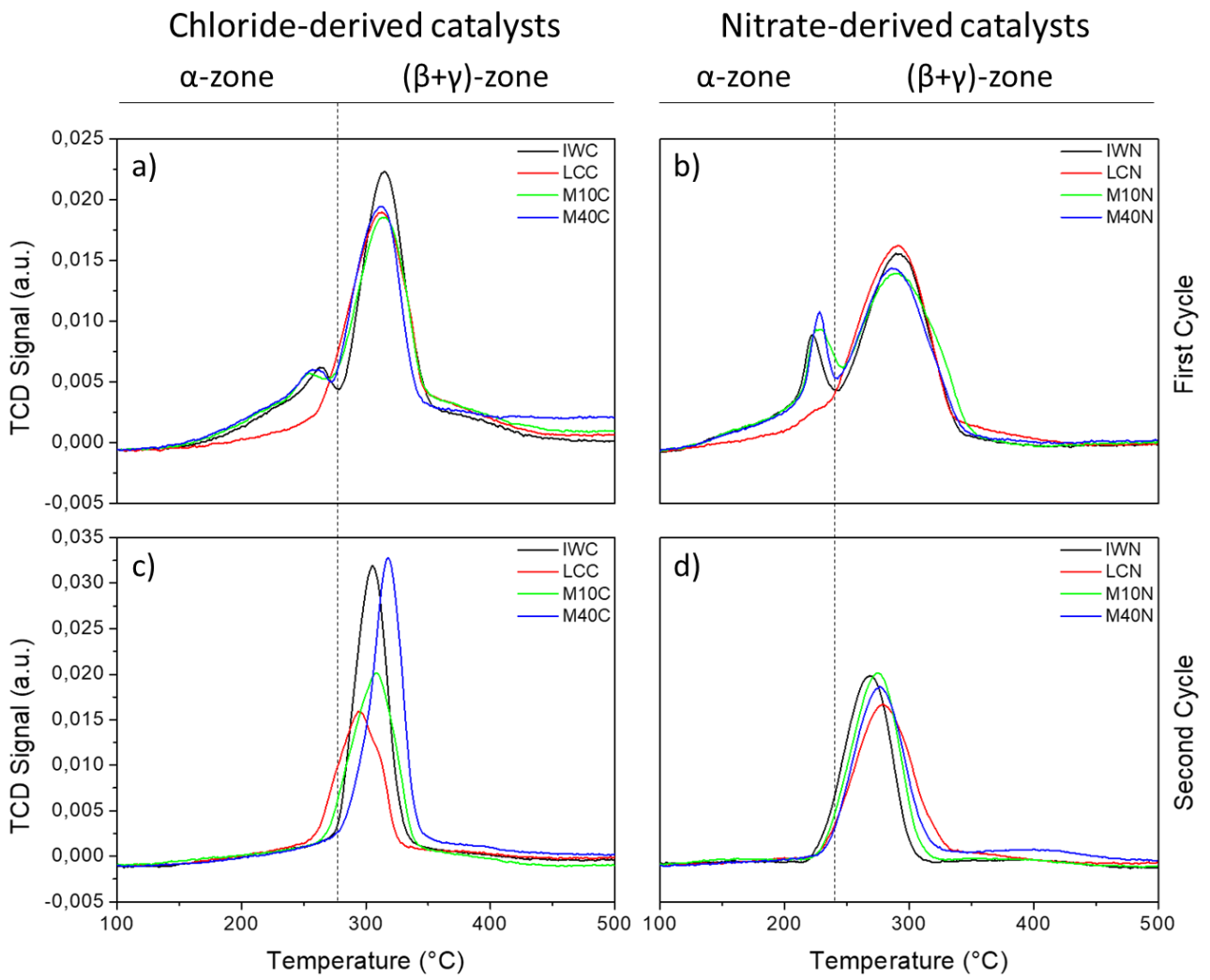


**Figure 8**: TPR profiles of the IW, LC, M10 and M40 catalysts from the chloride and nitrate series; a) First TPR cycle of the chloride series; b) First TPR cycle of the nitrate series; c) second TPR cycle of the chloride series; d) second TPR cycle of the nitrate series.

In Figure 8 a comparison between the first (Figs. 8a and 8b) and second (Figs. 8c and 8d) cycles of the $Cl^-$ and $NO_3^-$ catalysts respectively is reported. Regarding the first cycles it is possible to observe the presence of a small peak (α) at lower temperatures (see α-zone in Figs. 8a and 8b) whose attribution in literature is debated[39] and two other peaks, β and γ, partially or completely overlapped depending on the used Ni precursor (see β+γ zone, Figs. 8c and 8d). However, several authors describing nickel ceria solid solution and/or the substitution of $Ni^{2+}$ into the ceria lattice, attributed this peak to the easy reduction of surface adsorbed oxygen species, which is a consequence of Ni incorporation in the cerium oxide lattice[26,40,41]. In particular, Shan et. al.[41] exhaustively described the origin of these surface oxygen species: the incorporation of a $Ni^{2+}$ atom in the ceria lattice replaces some $Ce^{4+}$ forming a solid solution and unbalancing the charge which needs to be balanced with the generation of oxygen vacancies which are able to adsorb oxygen or oxygen containing molecules quite easily. They also pointed out that only a small amount of $Ni^{2+}$ can be

incorporated in the support lattice, with the remaining Ni segregating in large particles more or less interacting with the support. On the contrary, the attribution of the β and γ peaks to the reduction of bulk NiO is fully supported by literature, with the two components which are relative to the reduction of bulk NiO and the NiO in strong interaction with the support respectively[24,39,41–43]. Focusing on the α peak it is possible to observe that it is absent in both the LC samples, which is coherent with the literature attribution commented above, since the LC sample is supposed to be a simple heterogenous mixture of the two powders, thus, no peaks relative to a strong interactions between the two materials were expected to be observed. The comparison between the reference IW and the two milled catalysts did not show significant differences except for negligible shifts in the position of their maximum. In the $NO_3^-$ catalysts, all peaks are anticipated at lower temperature, with the α peak that appears clearly more intense with respect to the chloride analogues. In the $Cl^-$ materials the β+γ components are well distinct, the beta peak rises at 300/310°C and the gamma around 380/390°C, while the nitrate-series present a broad peak that is likely due to the overlapping of the two contributions. This is consistent with XRD results that showed a higher dispersion of the metal phase using nitrates rather than chlorides as precursors. Smaller crystallites tend to reduce more easily shifting the reduction peak at lower temperature[44]. From Figures 8c and 8d, that are relative to the second TPR cycle of the chloride and nitrate catalysts respectively, it is interesting to observe the disappearance of the α peak, since the species adsorbed on the oxygen vacancies were desorbed during the first cycle, together with an increase of intensity of the β peak, which suggests a sintering of the metal phase during the first cycle. Concerning the γ peak it possible to observe the presence of broad features at approximately 400°C in both the series, except for the LC sample, with a major intensity in the nitrate catalysts. Besides the disappearance of the α peak described above, an important difference in intensity of the peak between the different chloride catalysts was observed in the second cycle of TPR, which was not apparent in the reference IWC and M40C catalysts and showed a dependence with milling time, with the LCC (0 minutes of milling) that showed the minor intensity. From Figure 8d it is possible to observe that in the nitrate series this effect was not as pronounced as in the chloride-derived analogues. The reason of this difference must be related to a different Ni dispersion observed in the two series, as it was demonstrated, from the XRD analysis, the decomposition of the chloride precursor led to larger Ni particles compared to the nitrate precursor.

A better understanding of this phenomena can be obtained from the quantitative TPR analysis. Given the stoichiometry of reduction of the NiO by $H_2$:

$$NiO + H_2 \rightarrow Ni + H_2O$$

for the reduction of only NiO, we expect a Stoichiometric Ratio ($S_r$)

$$S_r = \frac{Moles\ of\ consumed\ Hydrogen}{Moles\ of\ Nickel} = 1$$

Table 3 and Figure 9 report the values of this ratio in the different cycles for the chloride catalysts at two reduction temperatures. In the first cycle the $H_2$ consumption was higher than that expected for the complete reduction of Nickel in all samples. This is because the measured values take into account the contribution of the reduction of $CeO_2$ surface.

It is interesting to note there is a drop in this value in the second cycle, which is more consistent for the catalysts milled for shorter times (LCC, M05C and M10C). This is probably due to the fact that for low milling times the major part of the Nickel introduced in the jar does not interact strongly with the support and tends, at the high temperatures and particular atmospheres of this experiment, to segregate and form large nanoparticles. After sintering, if the particle is large enough, the second oxidation step is not sufficient to fully re-oxidize the metal phase, and this could explain the minor hydrogen uptake registered in the second reduction cycle. Increasing the milling time this discrepancy tend to decrease, since the prolonged milling is able to promote a strong metal/support interaction and the incorporation of Ni into the support. In Figure 9 this effect is depicted with the graphical representations of the NiO particles after the second oxidation step; the yellow areas represent the oxidized phase while the black areas the metallic phase. If this hypothesis is correct, we should expect that by increasing the temperature of reduction from 800°C to 900°C the drop in the value of the 2$^{nd}$ cycle should be more enhanced, because of the major sintering that occurs at the higher temperatures. This is in line with what reported in the last column of Table 3 and in Figure 2.

**Table 3:** ratio between moles of consumed hydrogen and moles of Nickel of the catalyst of the chloride series at two different reduction temperatures.

| | Reduction Temperature 800°C | | Reduction Temperature 900°C | |
|---|---|---|---|---|
| **Catalyst** | **$S_r$ First Cycle** | **$S_r$ Second Cycle** | **$S_r$ First Cycle** | **$S_r$ Second Cycle** |
| IWC | 1.31 | 1.15 | 1.13 | 1.07 |
| LCC | 1.14 | 0.80 | 1.06 | 0.37 |
| M05C | 1.28 | 0.99 | 1.05 | 0.66 |
| M10C | 1.26 | 1.02 | 1.09 | 0.81 |
| M20C | 1.19 | 1.15 | 1.15 | 0.79 |
| M30C | 1.23 | 1.10 | 1.12 | 0.74 |
| M40C | 1.10 | 1.14 | 1.14 | 0.96 |
| M60C | 1.17 | 1.09 | 1.11 | 1.00 |

It should be noticed that the difference in the values of $S_r$ (first cycle) of the two experiments is likely due to the fact that for the second experiment another batch of support was used, which differed only for surface area ($56m^2/g$ *vs* $63m^2/g$). This would decrease the contribution of surface ceria reduction to total hydrogen consumption observed but this variation is not relevant for the purposes of the above discussion.

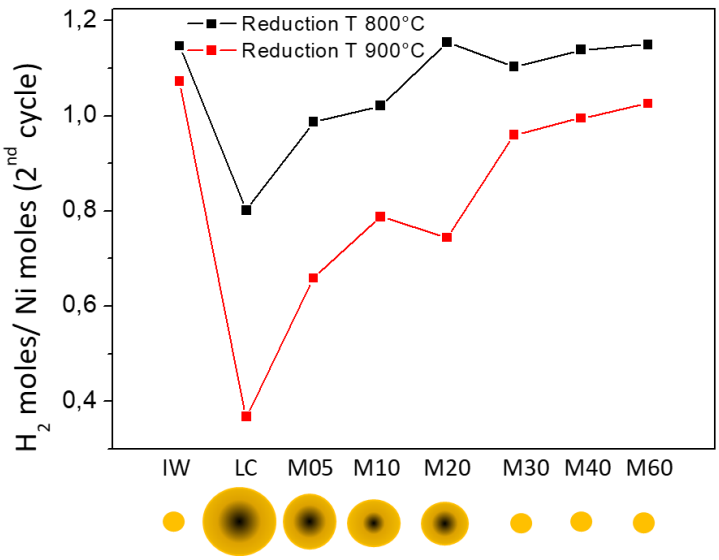


**Figure 9:** Trend of the $S_r$ with milling time together with a graphic representation of the NiO particles after the second oxidation step.

Another confirmation of this hypothesis comes from an *in-situ* XRD experiment in which we replicated the TPR experiment, following the same scheme of Figure 7. From Figure 10 we see that all the catalysts presented the typical peaks of NiO(111) and NiO(200) at 37 and 43 2Θ degrees respectively after the first oxidation, and the peak of metallic Ni(111) at 44 degrees after the first reduction, as expected. It is interesting to note that after the second oxidation step the LCC sample presented clearly a peak related to metallic Ni and two broad peaks related to the NiO, indicating that the Nickel oxidation has not been completed, in agreement with the formation of big Ni nanoparticles due to the sintering of the NiO phase not in strong interaction with the support during the first reduction step. In the M10C sample this phenomenon was still present, but the peaks of the nickel oxide were more intense, while the peak of metallic nickel decreased in intensity. In the M40C sample the Ni fully re-oxidized indicating a better dispersion of the metal phase likely due to a major quantity of nickel strongly interacting with the support.

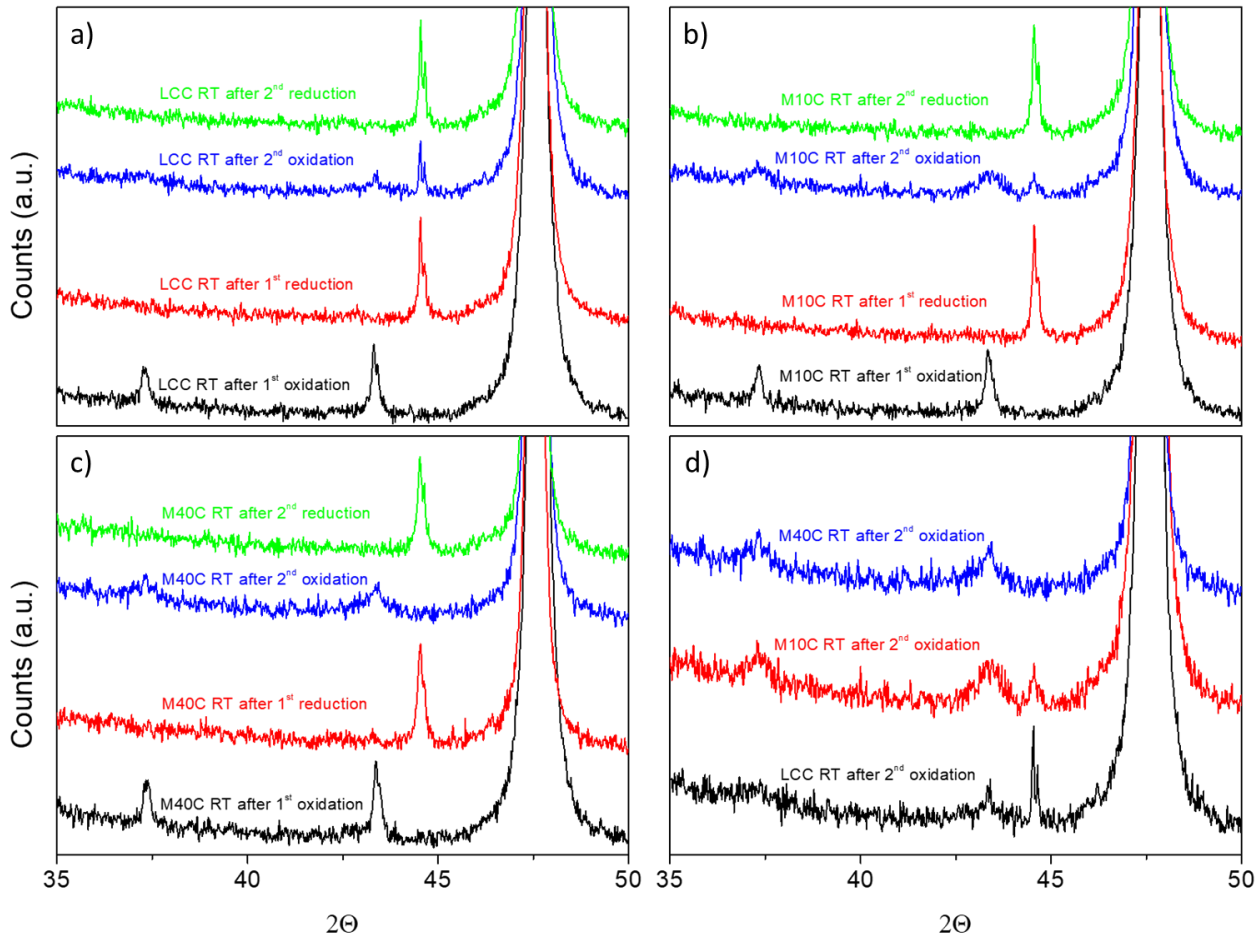


**Figure 10:** XRD profiles of three samples from the chloride series during the different steps of the TPR experiment: a) LC sample; b) M10 sample; c) M40 sample; d) comparison between LC, M10, M40 samples after the second oxidation step.

Table 4 shows analogous results for the $NO_3^-$ catalysts and evidences that the difference in the $S_r$ value between first and second cycle were approximately the same for all the catalysts of the series and likely attributable to the sintering of both the nickel and ceria phases. Regarding the samples milled for short times, in this case we did not observe the same high difference in Sr value observed in the catalysts obtained from the chloride series, indicating a minor sintering of the active phase.

**Table 4**: ratio between moles of consumed hydrogen and moles of Nickel of the catalyst of the chloride series.

| | Reduction Temperature 800°C | |
|---|---|---|
| **Catalyst** | **$S_r$ First Cycle** | **$S_r$ Second Cycle** |
| IWN | 1.23 | 0.94 |
| LCN | 1.17 | 0.99 |
| M05N | 1.29 | 1.10 |
| M10N | 1.29 | 0.98 |
| M20N | 1.23 | 0.99 |
| M30N | 1.27 | 1.04 |
| M40N | 1.36 | 1.00 |
| M60N | 1.29 | 0.98 |

It is likely that nickel particles deposited by nitrate precursors increase in size in the first reduction. Nevertheless, since they are initially smaller than those from chlorides and more interacting with the support (see HRTEM and XRD results), they grow to a size still suitable for a reversibility of the nickel oxidation-reduction process under the adopted operating conditions.

From these characterizations it is possible to design a graphical description, valid for the catalysts derived from both the precursors, of the process of incorporation of Ni into the cerium oxide with milling times and of the consequent behavior in the redox processes. In Figure 11 the yellow "clouds" represent the $CeO_2$ support while the black areas represent the Nickel phase. The IW sample consists of small particles well-dispersed and with a strong interaction with the support (Figure 11a). When the milling time is equal to zero (LC, Figure 11a) the $CeO_2$ and the Ni are not in strong interaction, thus during the thermal and reducing treatment the metallic phase segregates forming isolated nanoparticles with size depending on the precursors. Increasing the milling time, a portion of the nickel, thanks to the effect of the mild energy ball milling, strongly interacts with the support, but for low milling times (i.e. M05, M10, Figure 11c) a part of the nickel still segregates forming bigger nickel clusters that are difficult to oxidize. For prolongated milling times (M30, M40, M60, Figure 11e) it is possible to hypothesize that part of the nickel can be also encapsulated into the $CeO_2$ lattice.

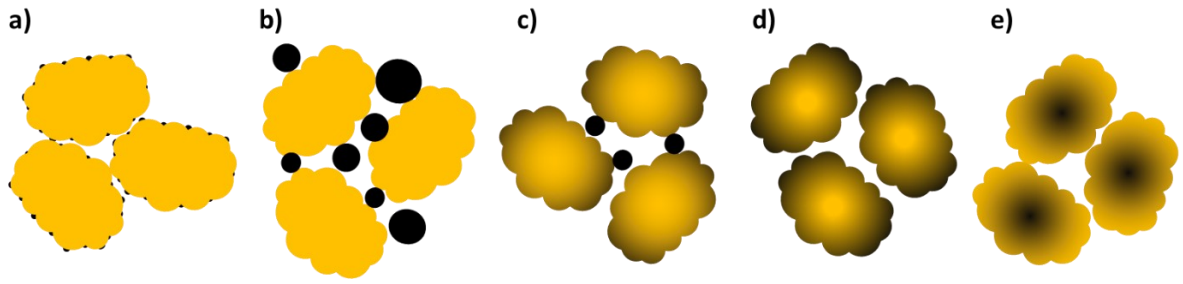


**Figure 11:** schematic representation of the different catalysts: a) reference Incipient Wetness catalyst; b) Loose Contact catalyst; c) M05 (M10) catalyst; d) (M10), M20 catalyst; e) M30, M40, M60 catalysts.

## 3.4.4. Catalytic tests

In Figure 12 the catalytic activity at two different temperatures, in terms of methane and carbon dioxide conversions and $H_2$/CO ratio, of the $Cl^-$ catalysts is reported comparing preparation method and milling time. The catalysts synthesized via ball milling technique have a better or comparable activity with the reference IWC catalyst.

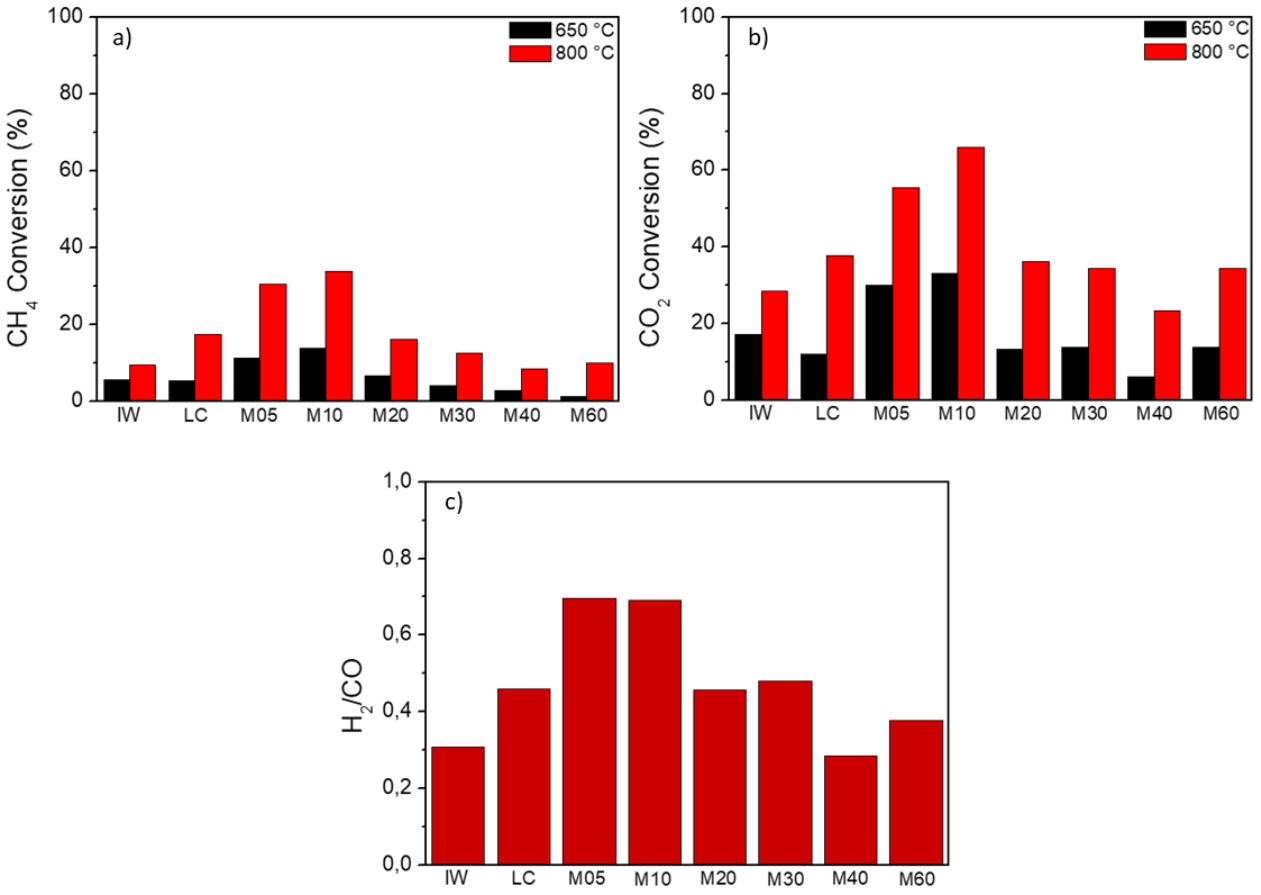


**Figure 12**: Catalytic performance parameters of $Cl^-$ catalysts; a) $CH_4$ conversion at 650°C (black bars) and 800°C (red bars); b) $CO_2$ conversion at 650°C (black bars) and 800°C (red bars); c) $H_2$/CO ratio at 800°C.

Conversions and $H_2$/CO ratio have a maximum in activity for the M10C catalyst, which at 800°C shows a methane conversion three times higher and a carbon dioxide conversion more than two times higher than that of IW. The same trend, with negligible differences, was observed by using another high surface area $CeO_2$ synthesized in our laboratories with the synthetic procedure described in chapter 3 (HSA), confirming the reproducibility of the synthetic procedure (Figure 13).

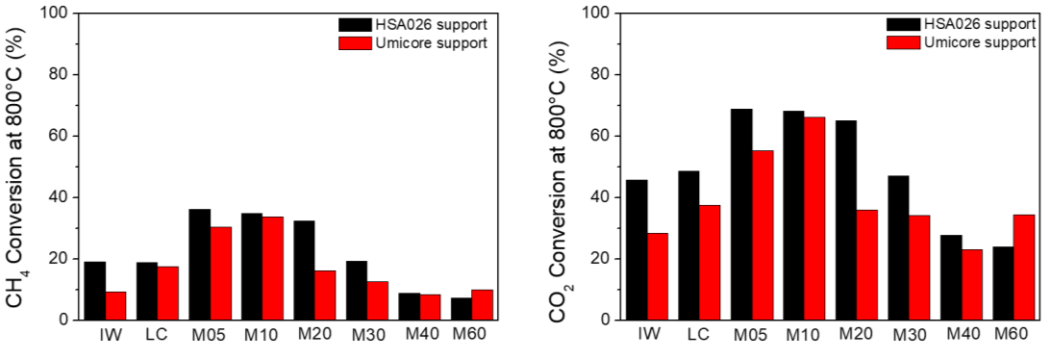


**Figure 13**: Comparison of two different series of catalysts obtained from $NiCl_2 \cdot 6H_2O$ by varying the support: a) $CH_4$ conversion at 800°C of the catalysts obtained from the HSA026 support; b) $CO_2$ conversion at 800°C of the catalysts obtained from the Umicore support.

Concerning the catalysts obtained from the nitrate precursor (Figure 14), most of the catalysts have a higher or similar activity in comparison to the reference IWN, with a minimum in activity for the M40N sample. The LCN resulted the most active catalyst of the series and the activity of the catalysts decreases linearly with the milling time.

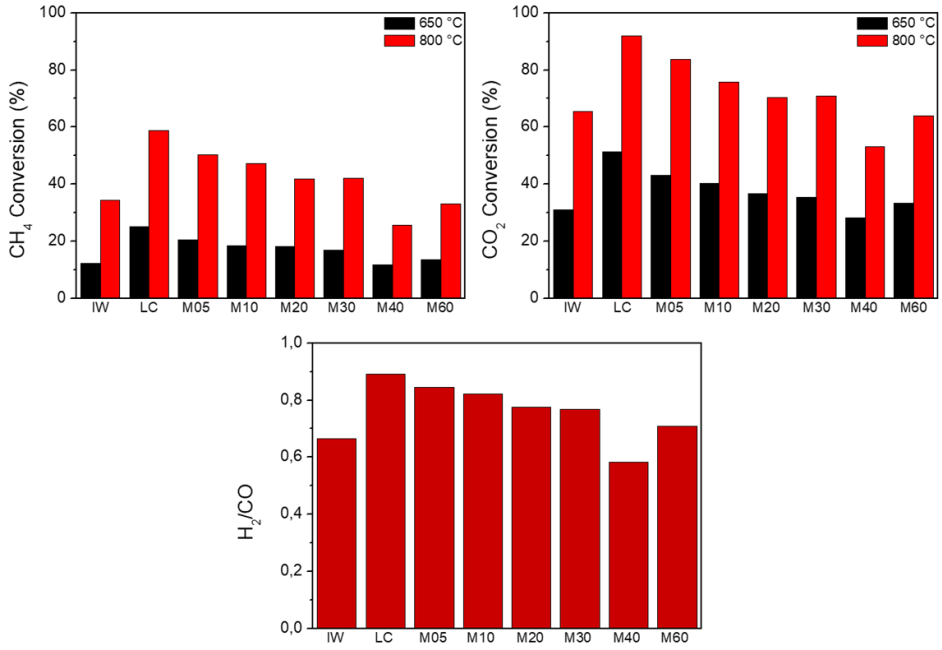


**Figure 14**: Catalytic performance parameters of the $NO_3^-$ catalysts , a) $CH_4$ conversion at 650°C (black bars) and 800°C (red bars); b) $CO_2$ conversion at 650°C (black bars) and 800°C (red bars); c) $H_2$/CO ratio at 800°C.

The comparison of the two series of catalysts (Figure 15) showed that the $NO_3^-$ catalysts are more active than that obtained from the chloride precursor, consistently with the different size of Nickel particles observed in the two series[32]. Moreover, it is known that chlorides could be incorporated on ceria lattice[45], which may have a detrimental effects in the catalytic activity[35].

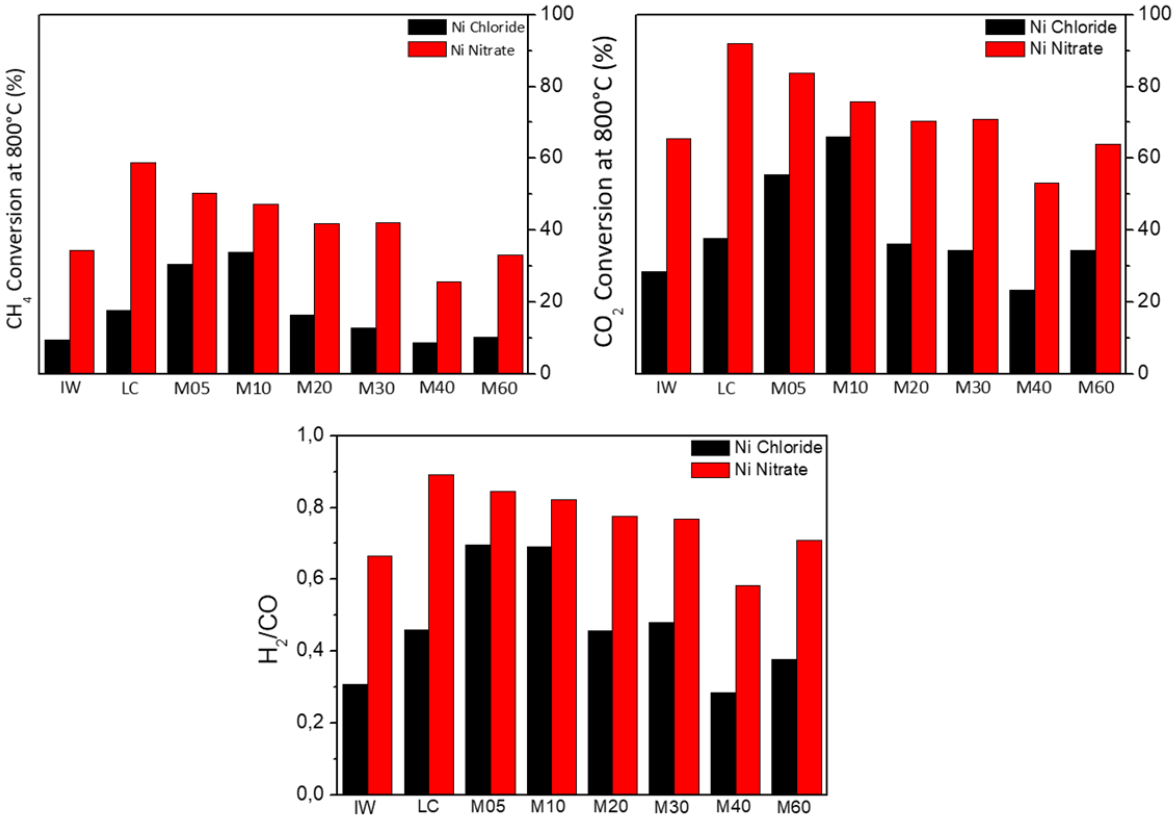


**Figure 15**: Comparison between the catalytic performance parameters of the catalysts from chloride (black bars) and nitrate (red bars) series in function of preparation method and milling time: a) $CH_4$ conversion at 800°C; b) $CO_2$ conversion at 800°C; c) $H_2$/CO ratio at 800°C.

We assessed carbon deposited on the catalysts by post-test thermal gravimetric analysis (TGA). Figure 16 summarizes the results in term of weight percent of carbon. In $NO_3^-$ catalysts the accumulation of carbon decrease with milling time: LCN and M05N samples are the ones which showed the major carbon formation. For the catalysts milled for higher milling times (M10N, M20N and M30N) a significant drop in the value of carbon formation was observed, the catalysts milled for higher milling times (M40N and M60N) showed no carbon formation. This trend is perfectly in agreement with the model proposed in figure 11. The LC sample is a mixture of ceria and free nickel particles, which are active in DRM reaction, but when not in strong interaction with the support they are very prone to the formation of carbon[7,8]. Increasing the milling time there is an increase of the fraction of Ni in strong interaction and less "free" nickel particles, which explains the decrease in carbon formation observed for the catalysts milled for higher milling times.

Regarding $Cl^-$ catalysts a minor quantity of carbon was detected. Moreover, the absence of carbonaceous deposits in the LCC sample seems to be in contradiction with what was commented for the nitrate analogue. These results could be explained with the minor catalytic activity of $Cl^-$ catalysts due to their lower Ni dispersion in comparison to the $NO_3^-$ catalysts. In addition, the presence of very larger Ni particles in LCC could justify the apparent contradiction observed, since too big metal nanoparticles are known to be less prone in the carbon formation related to the methane craking[46–48].

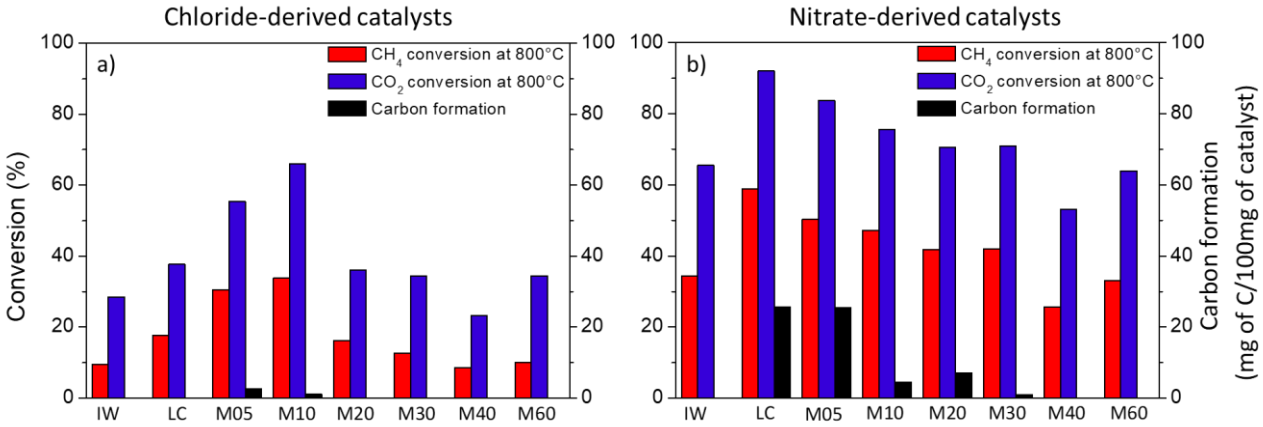


**Figure 16**: percentage of carbon on the spent catalysts.

In order to appraise the effect of carbon formation on the long term stability of catalysts, we performed some isothermal time on stream tests under the same experimental conditions of the tests described above, at 750°C for 70 hours.

Figure 17 shows the comparison between the stability performance of the reference IW and the M10 catalyst obtained from both precursors. Among the $Cl^-$ catalysts, the M10C sample has shown the best catalytic activity. In the nitrate series the M10N sample was the one with a good activity together with an acceptable carbon formation in comparison to the lower-milled samples LCN and M05N. Regarding the comparison between the IWC and M10C catalysts, it is possible to see that the IWC showed very low conversions for both $CH_4$ and $CO_2$, with a $H_2$/CO ratio of approximately 0.1. This catalytic performance is too low for any speculation about the stability of this material. M10C sample showed a rapid deactivation in the first hours of the stability test, reaching constant values of conversion and $H_2$/CO ratio after approximately 24 hours. The comparison between the IWN and M10N catalysts derived from the nitrate precursor is more interesting since both materials initially show conversion values appreciable and higher for M10N during the time of the test. Both the catalysts underwent deactivation during time. The difference between the two catalysts is better highlighted in Figure 18.

The comparison between the M10 catalysts obtained from the two series showed a major and rapid deactivation in the chloride derived precursor, which showed a deactivation of approximately 80% after 70 hours. A similar major deactivation at the beginning of the time-on-stream experiment was observed also in $Ni/CeO_2$ catalysts prepared by changing the nature of the precursor in the tri-reforming reaction[35], which is similar to the DRM process except for the presence small amounts of water and oxygen which are supposed to suppress the deactivation compared to the DRM process.

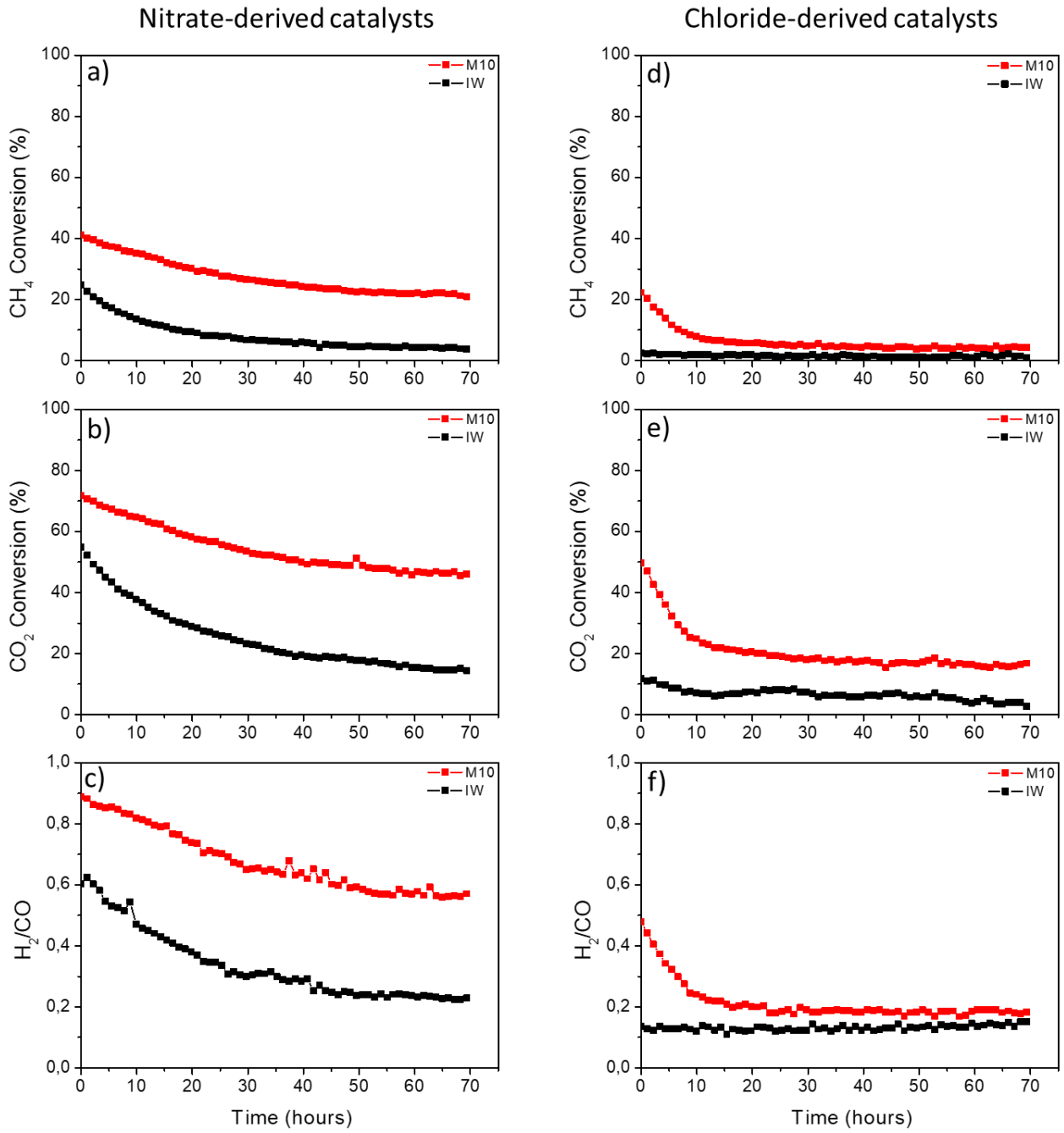


**Figure 17:** stability performances of the IW (black) and M10 (red) samples obtained from the nitrate (left side) and chloride (right side) in terms of $CH_4$ conversion (a and d), $CO_2$ conversion (b and e) and $H_2/CO$ ratio (c and f).

Figure 18 shows the catalytic indicators normalized for their initial value of the IWN, M10N and M30N catalyst. M30N is representative of a long-time milled sample with similar catalytic activity.

Both the milled catalysts showed a more stable behavior respect the IWN sample, whose $CH_4$ and $CO_2$ deactivation were of 85% and 75% respectively. The M30N sample showed a deactivation of 77% and 56% regarding the conversion of $CH_4$ and $CO_2$ respectively. The best stability was observed in the M10N catalyst which showed a $CH_4$ deactivation of 49% and a $CO_2$ deactivation of 36% after 70 hours. This comparison represents a remarkable result since it shows that $Ni/CeO_2$ catalysts derived from the nitrate precursor well compares in stability against the state of the art reference catalysts synthesized via incipient impregnation.

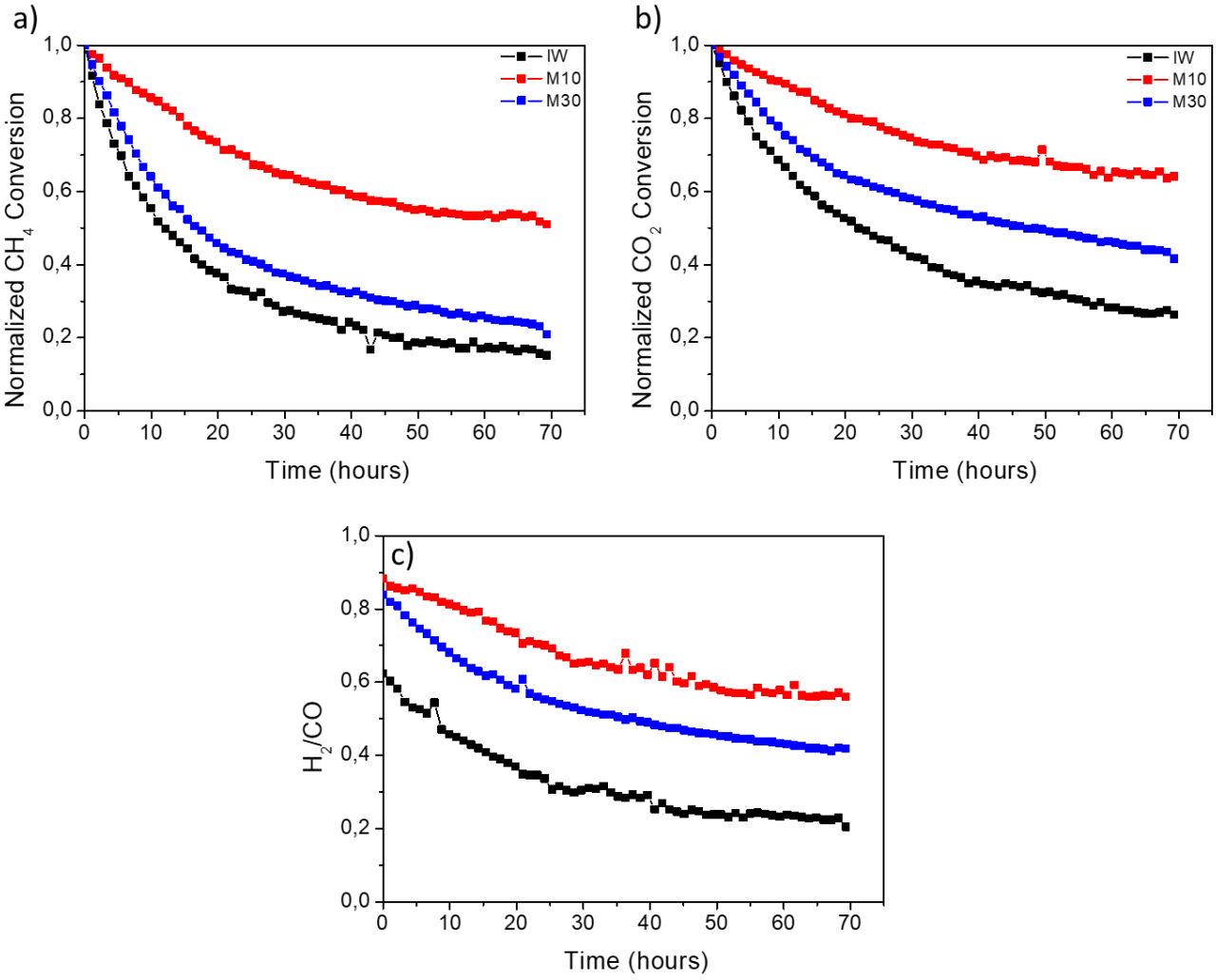


**Figure 18:** Stability performances of the IWN (black), M10N (red) and M30N (blue) catalysts from $NO_3^-$ in terms of a) $CH_4$ conversion; b) $CO_2$ conversion; c) $H_2/CO$ ratio.

Regarding the differences in the behavior of the two milled samples it is possible to conclude that a major stability was obtained for shorter milling times.

On the basis of HRTEM results, it is possible to hypothesize that the enhanced catalytic performance, in terms of both activity and stability, of milled samples might be related with the rugosity observed on their surface. In particular, we evidenced that the rugosity was more pronounced in the M10 sample with respect to the M40, which was chosen also as a representative long-time milled sample. We also mentioned that the said rugosity was maintained after reduction at 800°C in the M10 sample, thus in the catalytic conditions at which the material showed its behavior.

Considering the carbon mass balance of the IW and M10 catalysts, calculated from the gas composition at the different temperatures of the catalytic test and reported in Table 5, it is possible to see that at low temperatures more quantity of carbon is formed in the M10 catalyst. However, at higher temperatures at which the stability test was conducted, we can observe a negative value regarding the mass of carbon formed, indicating a gasification of the carbon deposited at the lower temperatures and this could be the reason of the stability we observed.

**Table 5**: Carbon mass balance of the IWN and M10N catalysts of the nitrate series at the different temperatures of the catalytic test.

| **IWN** | | | | |
|---|---|---|---|---|
| **Temperature (°C)** | **Moles of C (in) (mmol/min)** | **Moles of C (out) (mmol/min)** | **Delta (mmol/min) Moles (in) – Moles (out)** | **Mass of C (g/min)** |
| RT | 2.4 | | | |
| 550 | 2.4 | 2.347 | 0.053 | 0.000643 |
| 600 | 2.4 | 2.407 | -0.007 | -8.2E-05 |
| 650 | 2.4 | 2.382 | 0.018 | 0.00021 |
| 700 | 2.4 | 2.396 | 0.004 | 5.24E-05 |
| 750 | 2.4 | 2.386 | 0.014 | 0.000165 |
| 800 | 2.4 | 2.395 | 0.005 | 6.03E-05 |
| **M10N** | | | | |
| RT | 2.4 | | | |
| 550 | 2.4 | 2.327 | 0.073 | 0.000874 |
| 600 | 2.4 | 2.387 | 0.013 | 0.000161 |
| 650 | 2.4 | 2.363 | 0.037 | 0.000444 |
| 700 | 2.4 | 2.409 | -0.009 | -0.00011 |
| 750 | 2.4 | 2.421 | -0.021 | -0.00025 |
| 800 | 2.4 | 2.423 | -0.023 | -0.00027 |

## 3.4.5. XPS and NEXAFS analysis

A combined XPS and NEXAFS characterization has been performed in order to investigate the electronic structure of the LCN, IWN, M10N and M40N Ni-$CeO_2$ samples, synthetized starting from commercial HSA $CeO_2$ and $Ni(NO_3)_2 \cdot 6H_2O$ precursors.

All spectra have been measured with a photon energy of 1480.95 eV (from an *Al* K alpha X-Ray source). The samples have been measured as introduced in the UHV chamber. Looking at the survey spectra of Figure 19 we detected the presence of peaks related to Ce (3d, 4d and Auger MNN), Ni 2p, O (1s and Auger KLL), C1s, Ag 3d, and Mo (3d and 3p). The Mo peaks are due to the sample holder (made of Mo) and the Ag is present in the glue used to stick the sample on the sample holder. Thus, these two elements are present on the field of view of the analyzer but not on the sample surface. On the opposite the presence of the carbon (peak at ≈ 282 eV) on the surface of the sample is due to air exposure of the sample before being measured in the UHV chamber.

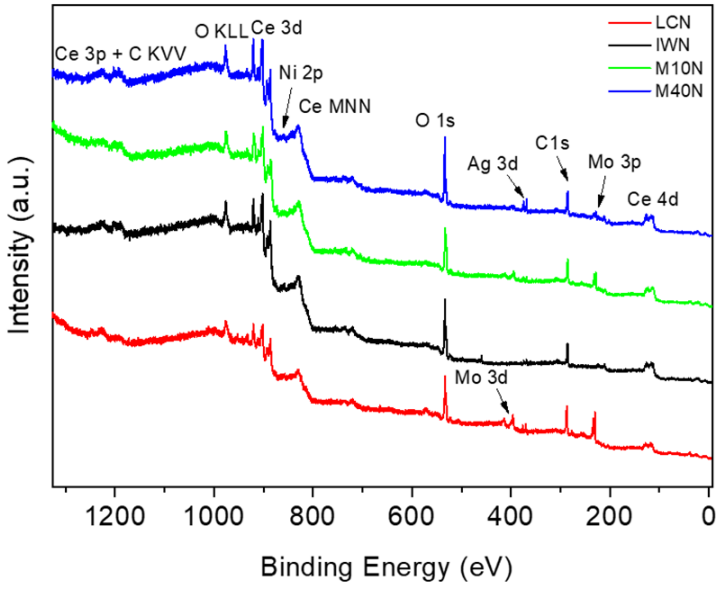


**Figure 19:** XPS survey spectra acquired for LC (red), IW (black), M10 (green) and M40 (blue) Ni-$CeO_2$ samples

To analyze more in detail the spectral modifications between the different samples, we acquired the Ce 3d core level spectra, shown in Figure 20. Ce 3d spectra are complex and display a rich multiplet structure. The fitting process of Ce 3d peaks is still under debate in literature because of the complexity of the photoemission peak, but we followed the procedure reported in a recent review[49]. $CeO_2$ spectrum can be deconvoluted in two multiplets (the blue components of Figure 20), corresponding respectively to electronic transitions related to the $3d_{3/2}$ and $3d_{5/2}$ orbitals, with a spin orbit splitting of about 18.3 eV.

u''' and v''' structures in Figure 20 are related to a Ce $3d_9 4f_0$ O $2p_6$ final state, while the lowest binding energy states u, v, u'', v'' structures are the result of Ce $3d_9 4f_2$ O $2p_4$ and Ce $3d_9 4f_1$ O $2p_5$ final states. The green components in the fit of Figure 20 have been attributed to $Ce_2O_3$. Also in this case, u and v labels are referred to the $3d_{3/2}$ and $3d_{5/2}$ spin orbits. The spin orbit splitting is about 17.9 eV, in agreement with literature data[50,51]. Each spin orbit is made of two structures: the ones with the higher BEs (u' and v') are related to a $3d_9 4f_1$ O $2p_6$ final state, while $u_0$ and $v_0$ can be attributed to a Ce $3d_9 4f_2$ O $2p_5$ state.

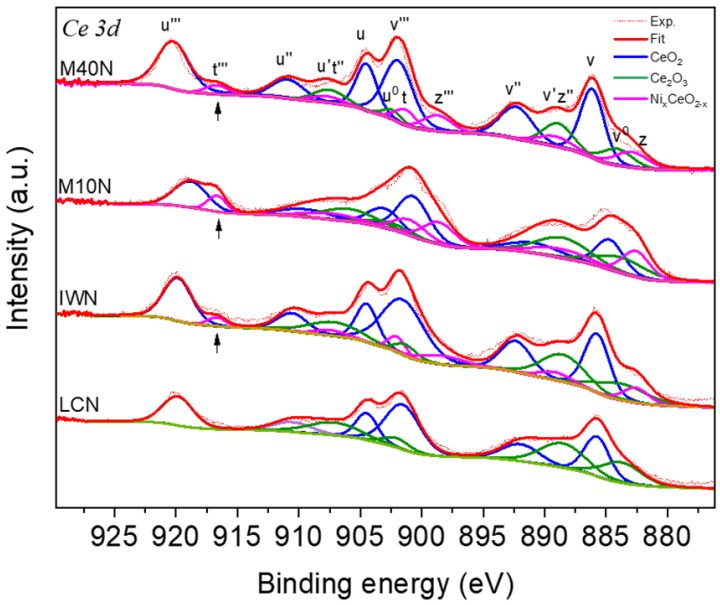


**Figure 20:** Ce 3d XPS spectra of the four Ni-$CeO_2$ samples, fitted with $CeO_2$, $Ce_2O_3$, $Ni_xCeO_{2-x}$ components.

Looking carefully at the spectra of Figure 20, it can be observed that the components attributed to Ce(IV) and Ce(III) oxides are not sufficient to obtain a good fit of the total spectrum, especially for the M10N sample. Indeed, three shoulders located at ≈ 884, 898 and 917 eV are present in the IWN, M10N and M40N samples: it is thus plausible that the structures were formed during the synthesis. Unfortunately, in literature the three new shoulders rarely have been observed for this kind of Ni-$CeO_2$ catalyst[49,52–54]. In particular, in Zhou et. al.[52] the authors observed these features in a series of transition-metal doped ceria microspheres, formulated as $M_xCeO_{2-x}$, including $Ni_xCeO_{2-x}$. Moreover, no agreement has been reached on their fitting process[49]. In this work, in order to clarify the nature of these transitions, we tried to perform a subtraction operation between the spectra of the M10N, who presented the most intense features, and the LCN in which they were not present, coherently with the expectations. The resulting spectrum is shown in the bottom part of Figure 21; even if it has a bad resolution, the subtracted spectrum allowed us to observe that the spectral shape is very similar to the one of a Ce(IV) species[49], thus we tried to fit the new peaks of Figure 20 with six components labelled as *t'''*, *t''*, *t* , *z'''*, *z''* and *z,* as we did for the structures referred to Ce(IV), but shifted to lower binding energies. The hypothesis of a $Ni_xCeO_{2-x}$ phase is consistent with the observation of a Ce(IV) species whose

XPS Ce 3d features are located at lower binding energies, because of the charge transfer effects due to the surface Ni incorporation.

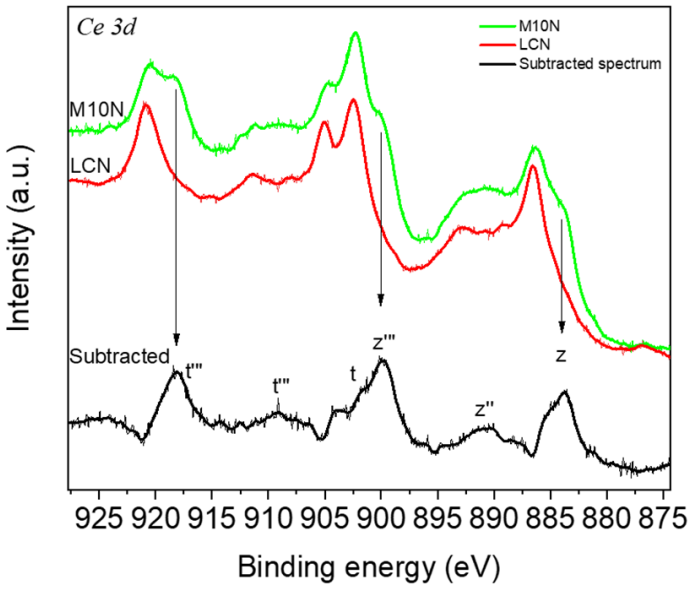


**Figure 21:** Top part: Ce 3d spectra related to the LC (red) and the M10 (green) samples. Bottom part: resulting spectrum obtained from the subtraction of the LC spectrum from the M10 one.

Also the HRTEM images indeed confirmed the presence of a Ni rugosity on the sample surface (see Figure 5) present especially for the M10N sample, which could be related to the $Ni_xCeO_{2-x}$ phase. The formation of this peculiar arrangement could be explained with the incorporation of $Ni^{2+}$ atoms in the defective sites of the support, which possessed a relatively high surface area of 64 $m^2/g$. The mechanical energy provided from the synthesis could have been able to promote a redox exchange between the surface $Ce^{3+}$ sites and the $Ni^{2+}$ atoms. This redox exchange implies an oxidation of the $Ce^{3+}$ to $Ce^{4+}$ and a reduction of $Ni^{2+}$ to a more reduced oxidation state. The Ce 3d XPS experiments confirmed the presence of an additional $Ce^{4+}$ feature, shifted at lower binding energies respect the conventional $Ce^{4+}$ signals of $CeO_2$, which could reasonably be related to the $Ce^{4+}$ in the different environment caused by the formation of the peculiar Ce-O-Ni arrangement obtained thanks to the synthetic technique.

Since this feature was found, with a negligible intensity, also in the IW catalyst one may argue that this phase is not related to the milling process. However, the Incipient Wetness procedure involved the use of a mortar and a pestle to homogenize the support with the solution containing the metal precursor. The whole process lasted about 30/40 minutes, and we can see that the intensities of the red features in the IW and M40 samples are approximately the same. As a matter of fact, the same XPS analysis conducted on a Impregnated catalyst synthesized by slow evaporation of a solution containing the proper amount of $Ni(NO_3)_2 \cdot 6H_2O$, so

with no grinding action of any mortar and pestle, revealed the absence of the feature described above (see figure 22).

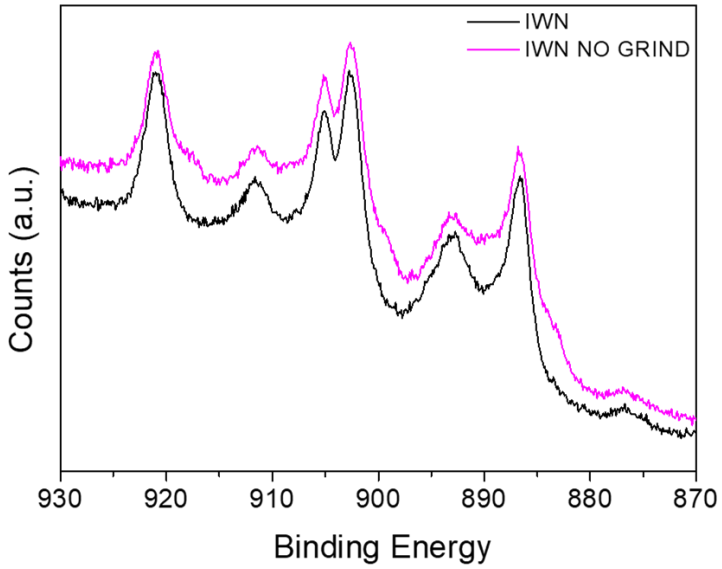


**Figure 22:** Comparison between the two Impregnated samples

As visible in Figure 20 the six component fit of the new features was successful. In order to further support the hypothesis of the $Ni_xCeO_{2-x}$ microstructure, we analyzed both the Ni 2p XPS and the Ni $L_{2,3}$ edges spectra (shown respectively in Figures 23 and 24. Unfortunately, Ni 2p photoemission spectra of Figure 23 were very noisy and difficult to interpret, because of the low Ni content of the samples (4% in weight). Nevertheless, we tried to fit the spectra with components typical of NiO, namely a, a' and a'' [55], for the LCN, IWN and M40N samples obtaining a relatively good fit. M10N Ni 2p spectrum could not be fitted using only the NiO components, thus we introduced two new components at lower binding energies (labelled in green in Figure 23), which compared to literature data can be assigned to a reduced Ni oxidation state[55,56]. In this way we obtained a good fit of the Ni 2p M10 sample. The presence of a Ni feature related to a lower oxidation state validates the abovementioned hypothesis of a redox exchange occurring between the $Ce^{3+}$ sites of the support and the $Ni^{2+}$ sites of the metal phase.

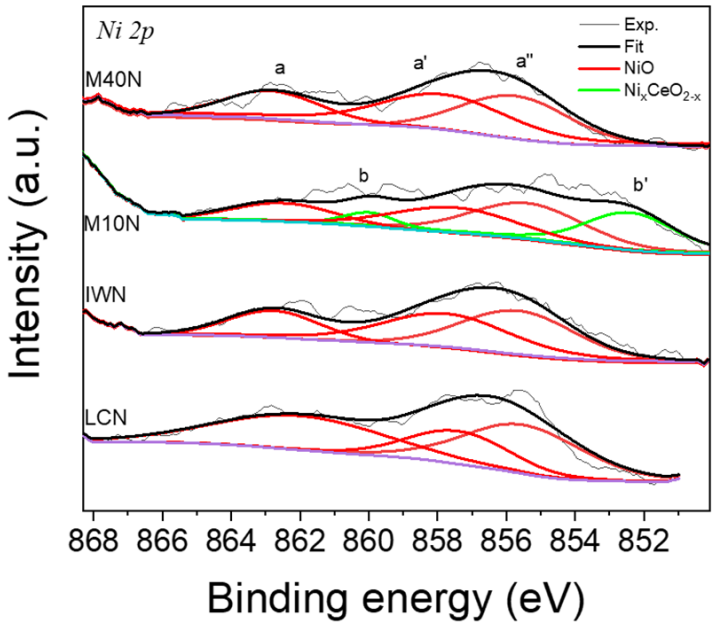


**Figure 23:** Ni 2p XPS spectra of the four Ni-$CeO_2$ samples, fitted with NiO (red) and $Ni_xCeO_{2-x}$ (green) components.

This result represents a further confirmation of the presence of a different $Ni_x$-$CeO_{2-x}$ arrangement in the first layers of the M10N sample surface, in which also Ni atoms have a different chemical environment and a different electronic structure, causing the formation of the new components at lower binding energies. To further investigate the electronic modifications of nickel we recorded the NEXAFS spectra of Ni $L_{2,3}$edges shown in Figure 24.

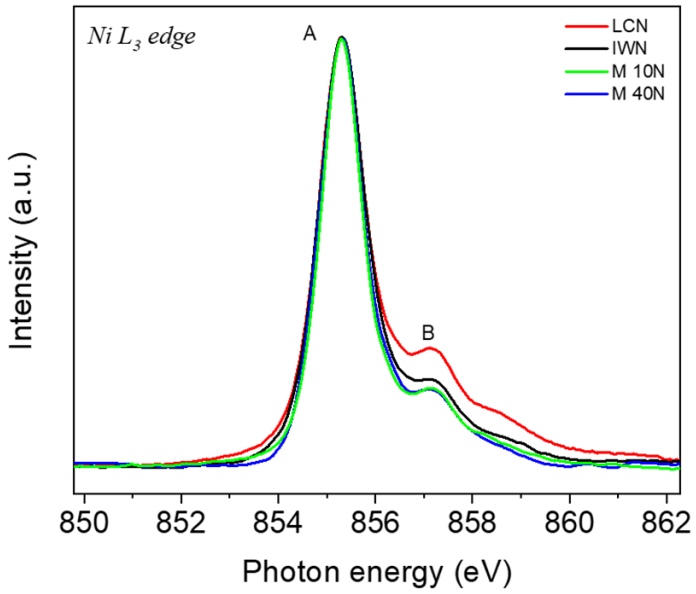


**Figure 24:** Ni $L_{2,3}$ edge spectra of the four Ni-$CeO_2$ samples normalized on the peak A maximum.

The $L_3$ edge is made of two main features located at ≈ 855 eV (A) and 857 eV (B). The first peak at 855 eV is ascribable to both $Ni^{2+}$ and $Ni^0$ oxidation states[57], while the structure at higher proton energies in typical of a $Ni^{2+}$ [56] and it is observable in all the four samples, even if it is more intense in the LCN. This result can be explained with a percentage of $Ni^{2+}$ sites which are reduced to a $Ni^{2-\delta}$ oxidation state, in agreement with the formation of the $Ni_x$-$CeO_{2-x}$ phase during the synthesis.

An apparent inconsistency between XPS and NEXAFS data arises from the observation that the components related to the $Ni_xCeO_{2-x}$ phase are visible only for M10N in the XPS of Ni 2p (Figure 23), while in the $L_{2,3}$ edges NEXAFS spectra we observe the same intensity decrease of peak B for IWN, M10N and M40N (Figure 24). The explanation lies in the probing depth of the two techniques, indeed with XPS only the first atomic layers are probed, while with the soft X-Ray NEXAFS using TEY detection mode the probing depth is between 2 and 5 nm[58,59]. Keeping in mind the model theorized in Figure 11, the $Ni_xCeO_{2-x}$ arrangement (where Ni and $CeO_2$ are in strong interaction) after 10 minutes of ball milling is extremely superficial (and thus it is visible in XPS spectra), while after 40 minutes and in the IW sample it is incorporated inside the particles, making it still visible in the NEXAFS spectra but not in the XPS ones.

Figure 25 shows the O 1s XPS spectra acquired for the four samples. The spectral shape has been deconvoluted in four components labelled as *i* (≈534.5 eV), *ii* (≈532.5 eV), *iii* (≈531.5 eV) and *iv* (≈529.6 eV). Based on literature data, we attributed *i* and *ii* to $CO_x$ and OH physisorbed species[60], *iii* to O vacancies and *iv* to the lattice O of $CeO_2$[61,62].

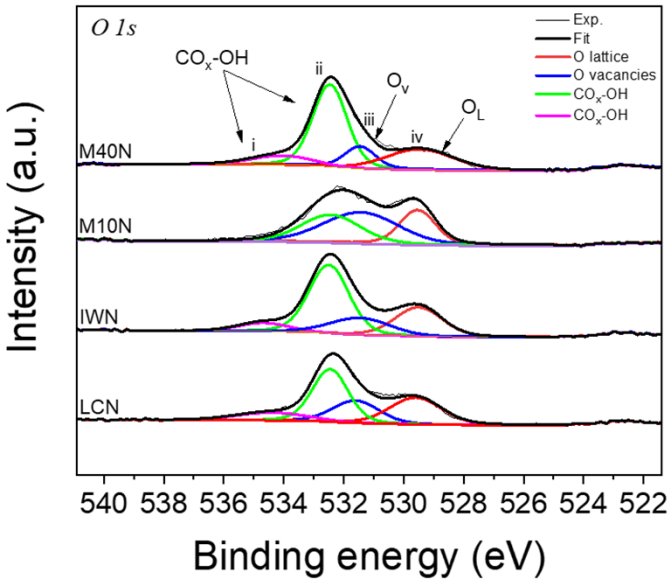


**Figure 25:** O 1s XPS spectra of the four Ni-$CeO_2$ samples, fitted with four components representing lattice O (iv), adsorbed surface O (iii) and adsorbed $CO_x$ and OH species (i and ii).

Peaks *i* and *ii* are present because the samples have been calcined in air at 500°C, and then cooled down in air to room temperature: during this process they could easily physisorb carbonaceous products and water

molecules coming from the air. We can observe from figure 25 that the O1s spectral shape of the M10N is different from the one of the other three samples. In particular, the component referred to $CO_x$ and OH species is almost negligible, while the *iii* is on the contrary more intense. Based on the results we depicted in Figure 21 and 23, we can suppose that peak *iii* is contributed by the O atoms of $Ce_2O_3$ but also by the $Ni_xCeO_{2-x}$ phase, which explains why it is more intense in the M10N spectrum; indeed, the O1s peak related to such solid solutions structures in Ni-$CeO_2$ compounds has already been found to be at higher binding energies with respect to the lattice O of $CeO_2$[62]. For what concerns *i* and *ii* structures ($CO_x$ and OH species), the fact that they are almost not present in the O1s M10N spectrum is a very interesting result, because it could mean that the $Ni_xCeO_{2-x}$ phase formed on the sample surface after 10 minutes of milling has different physisorption properties with respect to the classic structure of the Ni-$CeO_2$ material, and in particular that after the calcination treatment at 500°C $Ni_xCeO_{2-x}$ phase is less prone to adsorb $CO_x$ and water from the air.

Also the LCC and the M10C catalysts derived from the chloride precursor were analyzed in order to find the $Ni_xCeO_{2-x}$ nanostructure on the surface of the samples after the synthesis. Fig. 26 shows the Ce 3d spectra obtained for the two materials; also in this case it is evident that the electronic structure of Ce changes after the synthesis, in particular the structures attributed to the $Ni_xCeO_{2-x}$ arrangement arise (purple fitting curves), even if not so intense as for the M10N material obtained using nickel nitrate as precursor.

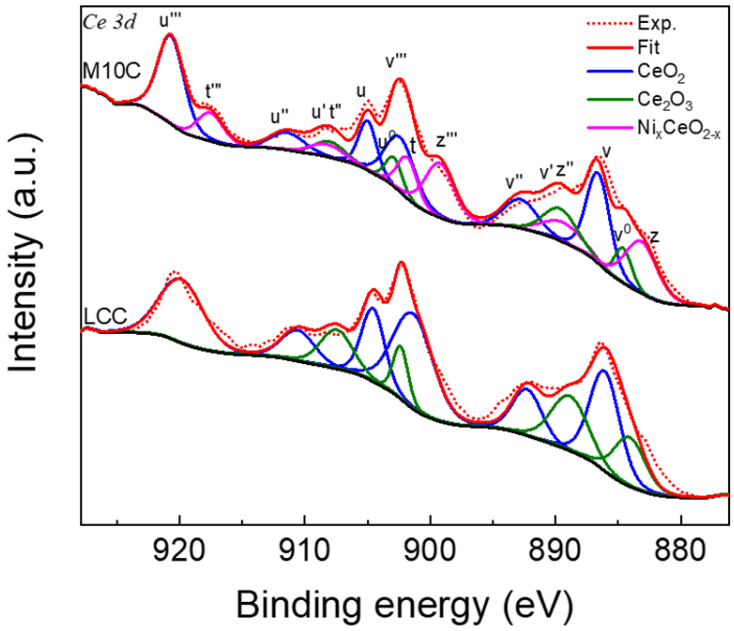


**Figure 26**: Ce 3d XPS spectra of the LC and M10 catalysts derived from the chloride series.

## 3.5. Conclusions

In this work we proposed a synthetic procedure for $Ni/CeO_2$ catalysts with mild energy ball milling technique starting from cerium oxide and hydrated nickel precursors. In particular, nickel chloride and nickel nitrate were studied. The use of the two different nickel precursors resulted in a difference in particle dimension of the metallic phase in the final catalyst; this evidence allowed us to conclude that the different anions have a particular and specific role in the synthesis. We also observed that the particle size of the metal phase in the catalysts obtained from the chloride precursor is larger compared to the corresponding catalysts obtained from the nitrate precursor, which are more active, thanks to the finer dispersion of the metal phase. A deep investigation on the milling time was performed and revealed that by increasing the milling time a decrease of the fraction of free nickel particles together with an increase of nickel in strong interaction with the support is observed. The catalytic tests in DRM conducted on the two series of catalysts revealed a benefic effect on the catalytic activity of several milled samples compared to the reference catalyst synthesized via the traditional incipient wetness technique. Furthermore, the catalytic tests conducted in the catalysts obtained from the nitrate series, confirmed the model we formulated after the TPR experiments, since we observed major amounts of carbon in the catalysts milled for shorter times (e.g. LC and M05) in which a major fraction of free nickel particles is present. By increasing the milling time a drop in carbon formation was observed, again in agreement with our model. In particular, regarding the nitrate series, we found that 10 minutes represents an optimal balance between free nickel particles and nickel in strong interaction with the support since it showed an interesting catalytic activity and stability, better to the one of the reference IW catalyst. The XPS analysis revealed the presence of an unpredicted set of signals which were particularly evident in the M10 sample and that we attributed to the formation of a $Ni_xCeO_{2-x}$ phase. This mixed phase was localized in the near surface of the materials and is in agreement with the HRTEM findings of a "rugosity" in which some sub-nanometric Ni entities were detected. The formation of this phase/arrangement was likely due to the mechanochemical-induced incorporation of Ni atoms in the defective sites of the used cerium oxide. This incorporation was accompanied a redox exchange, favored by the mechanical energy provided from the synthesis, between the surface $Ce^{3+}$ sites of the support and the $Ni^{2+}$ atoms of the nickel precursor, giving rise to the peculiar set of signals observed in both the Ce 3d and Ni 2p XPS analysis. For the materials milled for prolongated milling times this phase was still present, but the low intensity observed with the XPS suggested an incorporation of this phase in the deeper layers of the support. This represents an important result since we demonstrated, as did previously for $Pd/CeO_2$ systems(ref), that the mild shear-like stresses introduced by milling were able to promote peculiar surface arrangements between cerium oxide and the supported metal which are responsible for an enhanced catalytic performance of the material.

# 3.6. References


1. Spivey, J. A review of dry (CO2) reforming of methane over noble metal catalysts. *Chem Soc Rev* **43**, 7813–7837 (2014).

2. Júnior, L. C. P. F., Miguel, S. de, Fierro, J. L. G. & Carmo Rangel, M. do. Evaluation of Pd/La2O3 catalysts for dry reforming of methane. *Stud. Surf. Sci. Catal.* **167**, 499–504 (2007).

3. Ferreira-Aparicio, P., Fernandez-Garcia, M., Guerrero-Ruiz, A. & Rodríguez-Ramos, I. Evaluation of the Role of the Metal–Support Interfacial Centers in the Dry Reforming of Methane on Alumina-Supported Rhodium Catalysts. *J. Catal.* **190**, 296–308 (2000).

4. Ferreira-Aparicio, P., Rodríguez-Ramos, I., Anderson, J. A. & Guerrero-Ruiz, A. Mechanistic aspects of the dry reforming of methane over ruthenium catalysts. *Appl. Catal. A Gen.* **202**, 183–196 (2000).

5. Wang, Y., Yao, L., Wang, S., Mao, D. & Hu, C. Low-temperature catalytic CO2 dry reforming of methane on Ni-based catalysts: A review. *Fuel Process. Technol.* **169**, 199–206 (2018).

6. Fan, M. S., Abdullah, A. Z. & Bhatia, S. Utilization of greenhouse gases through dry reforming: Screening of nickel-based bimetallic catalysts and kinetic studies. *ChemSusChem* **4**, 1643–1653 (2011).

7. Wang, S., Q. (Max) Lu, G. & J. Millar, G. Carbon Dioxide Reforming of Methane To Produce Synthesis Gas over Metal-Supported Catalysts: State of the Art. *Energy & Fuels* **10**, 896–904 (1996).

8. Wang, S. A Comprehensive Study on Carbon Dioxide Reforming of Methane over Ni/γ-Al2O3 Catalysts. *Ind. & Eng. Chem. Res.* **38**, 2615–2625 (1999).

9. Ian, Z., Das, S., Ing, M., Wai, H., Hongmanorom, P., Kawi, S. *AReview on Bimetallic Nickel-Based Catalysts for CO 2 Reforming of Methane*. *ChemPhysChem* vol. 18 (2017).

10. Wu, T., Cai, W., Zhang, P., Song, X., Gao, L. Cu-Ni@SiO 2 alloy nanocomposites for methane dry reforming catalysis. *RSC* **3**, 23976–23979 (2013).

11. Song, K., Lu, M., Xu, S., Chen, C., Zhan, Y., Li, D. & Au, C., Jiang, L., Tomishige, K. Effect of alloy composition on catalytic performance and coke-resistance property of Ni-Cu/Mg(Al)O catalysts for dry reforming of methane. *Appl. Catal. B Environ.* **239**, 324–333 (2018).

12. Leba, A. & Yıldırım, R. Determining most effective structural form of nickel-cobalt catalysts for dry reforming of methane. *Int. J. Hydrogen Energy* **45**, 4268–4283 (2020).

13. Wahyu Budiman, A., Song, S.-H., Chang, T.-S., Shin, C.-H. & Choi, M.-J. Dry Reforming of Methane

Over Cobalt Catalysts: A Literature Review of Catalyst Development. *Catal. Surv. Asia* **16**, 183–197 (2012).

14. Kitla, A., Safonova, O. V & Föttinger, K. Infrared Studies on Bimetallic Copper/Nickel Catalysts Supported on Zirconia and Ceria/Zirconia. *Catal. Letters* **143**, 517–530 (2013).

15. Lv, X., Chen, J. F., Tan, Y. & Zhang, Y. A highly dispersed nickel supported catalyst for dry reforming of methane. *Catal. Commun.* **20**, 6–11 (2012).

16. Lu, Y., Guo, D., Zhao, Y., Moyo, P. S., Zhao, Y., Wang, S., Ma, X. Confined high dispersion of Ni nanoparticles derived from nickel phyllosilicate structure in silicalite-2 shell for dry reforming of methane with enhanced performance. *Microporous Mesoporous Mater.* **313**, 110842 (2021).

17. Boaro M., Colussi S., T. A. Ceria-Based Materials in Hydrogenation and Reforming Reactions for CO2 Valorization. *Front. Chem. | www.frontiersin.org* **7**, 28 (2019).

18. Laosiripojana, N. & Assabumrungrat, S. Catalytic dry reforming of methane over high surface area ceria. *Appl. Catal. B Environ.* **60**, 107–116 (2005).

19. Usman, M., Wan Daud, W. M. A. & Abbas, H. F. Dry reforming of methane: Influence of process parameters—A review. *Renew. Sustain. Energy Rev.* **45**, 710–744 (2015).

20. Liu, Z., Grinter, D. C., Lustemberg, P. G., Nguyen-Phan, T. D., Zhou, Y., Luo, S., Waluyo, I., Crumlin, E. J., Stacchiola, D. J. *et al.* Dry Reforming of Methane on a Highly-Active Ni-CeO2Catalyst: Effects of Metal-Support Interactions on C−H Bond Breaking. *Angew. Chemie - Int. Ed.* **55**, 7455–7459 (2016).

21. Gonzalez-Delacruz, V. M., Ternero, F., Pereñíguez, R., Pereñíguez, P., Caballero, A. & Holgado, J. P. Study of nanostructured Ni/CeO 2 catalysts prepared by combustion synthesis in dry reforming of methane. *Appl. Catal. A Gen.* **384**, 1–9 (2010).

22. Strniša, F., Sagar, V. T., Djinović, P., Pintar, A. & Plazl, I. Ni-containing CeO2 rods for dry reforming of methane: Activity tests and a multiscale lattice Boltzmann model analysis in two model geometries. *Chem. Eng. J.* **413**, 127498 (2021).

23. Zhang, S., Muratsugu, S., Ishiguro, N. & Tada, M. Ceria-Doped Ni/SBA-16 Catalysts for Dry Reforming of Methane. *ACS Catal* **3**, 1855–1864 (2013).

24. Zhang, C., Li, S., Wu, G. & Gong, J. Synthesis of stable Ni-CeO2 catalysts via ball-milling for ethanol steam reforming. *Catal. Today* **233**, 53–60 (2014).

25. Wang, F., Zhang, L., Deng, J., Zhang, J., Han, B., Wang, Y., Li, Z., Yu, H., Cai, W., Deng, Z. Embedded Ni catalysts in Ni-O-Ce solid solution for stable hydrogen production from ethanol steam reforming

reaction. *Fuel Process. Technol.* **193**, 94–101 (2019).

26. Deng, J., Chu, W., Wang, B., Yang, W. & Zhao, X. S. Mesoporous Ni/Ce1-xNixO2-y heterostructure as an efficient catalyst for converting greenhouse gas to H2 and syngas. *Catal. Sci. Technol.* **6**, 851–862 (2016).

27. Wu, L., Xie, X., Ren, H. & Gao, X. A short review on nickel-based catalysts in dry reforming of methane: Influences of oxygen defects on anti-coking property. *Mater. Today Proc.* **42**, 153–160 (2021).

28. Achim Stolle, B. R. *Ball Milling Towards Green Synthesis: Applications, Projects, Challenges*. (ACS Green Chemistry, 2014).

29. Ralphs, K., Hardacre, C. & James, S. L. Application of heterogeneous catalysts prepared by mechanochemical synthesis. *Chem. Soc. Rev* **42**, 7701 (2013).

30. Danielis, M., Colussi, S., de Leitenburg, C., Soler, L., Llorca, J., Trovarelli, A. Outstanding Methane Oxidation Performance of Palladium-Embedded Ceria Catalysts Prepared by a One-Step Dry Ball-Milling Method. *Angew. Chemie - Int. Ed.* **57**, 10212–10216 (2018).

31. Danielis, M., Colussi, S., de Leitenburg, C. & Trovarelli, A. The role of palladium salt precursors in Pd-PdO/CeO2 catalysts prepared by dry milling for methane oxidation. *Catal. Commun.* **135**, 105899 (2020).

32. Cargnello, M., Doan-Nguyen, V.V.T., Gordon, T. R., Diaz, R. E., Stach, E. A., Gorte, R. J., Fornasiero, P., Murray, C. B. Control of metal nanocrystal size reveals metal-support interface role for ceria catalysts. *Science (80-. ).* **341**, 771–773 (2013).

33. Gayen, A., Boaro, M., Leitenburg, C. de, Llorca, J. & Trovarelli, A. Activity, durability and microstructural characterization of ex-nitrate and ex-chloride Pt/Ce0.56Zr0.44O2 catalysts for low temperature water gas shift reaction. *J. Catal.* **270**, 285–298 (2010).

34. Pappacena, A., Razzaq, R., De Leitenburg, C., Boaro, M. & Id, A. T. inorganics The Role of Neodymium in the Optimization of a Ni/CeO 2 and Ni/CeZrO 2 Methane Dry Reforming Catalyst. *inorganics* **6**, 39–54 (2018).

35. García-Vargas, J. M., Valverde, J. L., De Lucas-Consuegra, A., Gómez-Monedero, B., Sánchez, P., Dorado, F. Precursor influence and catalytic behaviour of Ni/CeO2 and Ni/SiC catalysts for the tri-reforming process. *Appl. Catal. A Gen.* **431**–**432**, 49–56 (2012).

36. Wang, S. & Lu, G. Q. Reforming of methane with carbon dioxide over Ni/Al2O3 catalysts: Effect of nickel precursor. *Appl. Catal. A Gen.* **169**, 271–280 (1998).

37. Lenggoro, I. W., Itoh, Y., Iida, N. & Okuyama, K. Control of size and morphology in NiO particles prepared by a low-pressure spray pyrolysis. *Mater. Res. Bull.* **38**, 1819–1827 (2003).

38. Gonzalez-Delacruz, V. M., Ternero, F., Pereñíguez, R., Caballero, A. & Holgado, J. P. Study of nanostructured Ni/CeO2 catalysts prepared by combustion synthesis in dry reforming of methane. *Appl. Catal. A Gen.* **384**, 1–9 (2010).

39. Yahi, N., Menad, S. & Rodríguez-Ramos, I. Dry reforming of methane over Ni/CeO2 catalysts prepared by three different methods. *Green Process. Synth.* **4**, 479–486 (2015).

40. Wang, L., Liu, H., Liu, Y., Chen, Y. & Yang, S. Influence of preparation method on performance of Ni-CeO2 catalysts for reverse water-gas shift reaction. *J. Rare Earths* **31**, 559–564 (2013).

41. Shan, W., Luo, M., Ying, P., Shen, W. & Li, C. Reduction property and catalytic activity of Ce1−XNiXO2 mixed oxide catalysts for CH4 oxidation. *Appl. Catal. A Gen.* **246**, 1–9 (2003).

42. Iulianelli, A., Liguori, S., Vita, A., Italiano, C., Fabiano, C., Huang, Y., Basile, A. The oncoming energy vector: Hydrogen produced in Pd-composite membrane reactor via bioethanol reforming over Ni/CeO2 catalyst. *Catal. Today* **259**, 368–375 (2016).

43. Zhang, B., Tang, X., Li, Y., Cai, W., Xu, Y., Shen, W. Steam reforming of bio-ethanol for the production of hydrogen over ceria-supported Co, Ir and Ni catalysts. *Catal. Commun.* **7**, 367–372 (2006).

44. Li, J., Li, P., Li, J., Tian, Z. & Yu, F. Highly-Dispersed Ni-NiO Nanoparticles Anchored on an SiO 2 Support for an Enhanced CO Methanation Performance. *Catalysts* **9**, (2019).

45. Trovarelli, A. *Catalysis by Ceria and Related Materials*. (2002).

46. Ashik, U. P. M., Wan Daud, W. M. A. & Hayashi, J. ichiro. A review on methane transformation to hydrogen and nanocarbon: Relevance of catalyst characteristics and experimental parameters on yield. *Renew. Sustain. Energy Rev.* **76**, 743–767 (2017).

47. Seidel, R., S. Duesberg, G., Unger, E., P. Graham, A., Liebau, M., Kreupl, F. Chemical Vapor Deposition Growth of Single-Walled Carbon Nanotubes at 600 °C and a Simple Growth Model. *J. Phys. Chem. B* **108**, 1888–1893 (2004).

48. Han, J. W., Park, J. S., Choi, M. S. & Lee, H. Uncoupling the size and support effects of Ni catalysts for dry reforming of methane. *Appl. Catal. B Environ.* **203**, 625–632 (2017).

49. Paparazzo, E. Use and mis-use of x-ray photoemission spectroscopy Ce3d spectra of Ce2O3 and CeO2. *J. Phys. Condens. Matter* **30**, (2018).

50. Beche, E. B., Charvin, P., Perarnau, D., Abanades, S. & Flamant, G. Short Communication Ce 3d XPS

investigation of cerium oxides and mixed cerium oxide (Ce x Ti y O z ). *Surf. Interface Anal.* **40**, 264–267 (2008).

51. Maslakov, K. I., Teterin, Y. A., Popel, A. J., Teterin, A. Y., Ivanov, K. E., Kalmykov, S. N., Petrov, V. G., Petrov, P. K., Farnan, I. XPS study of ion irradiated and unirradiated CeO2 bulk and thin film samples. *Appl. Surf. Sci.* **448**, 154–162 (2018).

52. Zhou, L., Li, X., Yao, Z., Chen, Z., Hong, M., Zhu, R., Liang, Y., Zhao, J. Transition-Metal Doped Ceria Microspheres with Nanoporous Structures for CO Oxidation OPEN. *Sci. Rep.* **6**, 23900–23906 (2016).

53. Villas-Boas, L. A., De Paula Nascente, P. A., Landers, R., Campos, M. & De Souza, D. M. P. F. The effect of Co and Zn addition on densification and electrical properties of ceria-based nanopowders. *Mater. Res.* **19**, 1057–1063 (2016).

54. Guo, X., He, H., Traitangwong, A., Gong, M., Meeyoo, V., Li, P., Li, C., Peng, Z., Zhang, S. Ceria imparts superior low temperature activity to nickel catalysts for CO2 methanation. *Catal. Sci. Technol.* **9**, 5636–5650 (2019).

55. Mansour, A. N. Characterization of NiO by XPS. *Surf. Sci. Spectra* **3**, 231–238 (1994).

56. Miller, A. C. & Simmons, G. W. Nickel by XPS. *Surf. Sci. Spectra* **1**, 312–317 (1992).

57. Sánchez-Agudo, M., Yubero, F., Fuentes, G. G., Gutiérrez, A., Sacchi, M., Soriano, L., Sanz, J. M. Study of the growth of ultrathin films of NiO on Cu(111). *Surf. Interface Anal.* **30**, 396–400 (2000).

58. Ruosi, A., Raisch, C., Verna, A., Werner, R., Davidson, B. A., Fujii, J., Kleiner, R., Koelle, D. Electron sampling depth and saturation effects in perovskite films investigated by soft x-ray absorption spectroscopy. *Phys. Rev. B - Condens. Matter Mater. Phys.* **90**, 1–8 (2014).

59. Panaccione, G. & Kobayashi, K. Hard X-ray photoemission spectroscopy: Variable depth analysis of bulk, surface and interface electronic properties. *Surf. Sci.* **606**, 125–129 (2012).

60. Tang, C., Sun, J., Yao, X., Cao, Y., Liu, L., Ge, C., Gao, F., Dong, L. Efficient fabrication of active CuO-CeO2/SBA-15 catalysts for preferential oxidation of CO by solid state impregnation. *Appl. Catal. B Environ.* **146**, 201–212 (2014).

61. Chen, D., Ma, Q., Wei, L., Li, N., Shen, Q., Tian, W., Zhou, J., Long, J. Catalytic hydroliquefaction of rice straw for bio-oil production using Ni/CeO2 catalysts. *J. Anal. Appl. Pyrolysis* **130**, 169–180 (2018).

62. Pal, P., Kumar Singha, R., Saha, A., Bal, R. & Baran Panda, A. Defect-Induced Efficient Partial Oxidation of Methane over Nonstoichiometric Ni/CeO2 Nanocrystals. *J. Phys. Chem. C* **119**, 13610–

13618 (2015).

# 4. Inverse $CeO_2$-CuO catalyst prepared by ball milling for partial methane oxidation: an *in-situ* DRIFT / *operando* NEXAFS study

## 4.1. Abstract

A series of inverse $CeO_2$-CuO catalysts whit increasing Cerium-Copper molar ratio synthesized with a novel and effective mild-energy ball milling technique was investigated. The utilization of the mild energy ball milling technique was found to be an effective synthetic method to induce a redox reaction between the surface $Ce^{3+}$ sites of the supported oxide with the $Cu^{2+}$ sites of the support at ambient temperature. Contrarily to a reference equivalent material synthesized with a classic impregnation method, the synthesized composites revealed to be active in methane activation at 250°C. We also carried out a multi analytical approach that combines in situ Diffuse Reflectance Infrared Fourier Transform Spectroscopy (DRIFT) with operando X-ray Adsorption Near Edge Spectroscopy (XANES or NEXAFS) that resulted very effective in the understanding of the mechanism of methane activation at low temperature. Through this approach, we showed that the activity was related to the formation of a stable and reversible $Ce^{4+}/Cu^{+}$ couple, created thanks to the mechanical action provided by the milling action. We observed that the $CeO_2$ loading affected the desorption of the activated-methane species. During the operando NEXAFS analysis conducted at a low ceria content sample the formation of traces of the partial oxidation products and valuable chemicals, formaldehyde and methanol, were observed. We think that these results might put the basis for the preparation of a wide class of mixed-oxides composites where redox exchange reactions between the metal ions on the surface of the oxides can be easily promoted through the use of mechanochemical methods.

# 4.2. Introduction

As pointed out in the first chapter, the study of metal-oxide interfaces and SMSI (strong metal support interaction) is of great importance for the low temperature (< 300°C) activation of methane. In particular, the goal is represented by the finding of specific active sites for methane activation and subsequent functionalization into valuable product/chemicals. The Direct Methane To Methanol reaction (DMTM) is nowadays one of the most investigated approaches for methane functionalization in heterogenous catalysis[1–4] since methanol represents an attractive molecule for different applications: as intermediate for other chemicals such as dimethyl ether, as a fuel for fuel cells or as hydrogen carrier[4–8]. The main issue in this process is represented by the scarce selectivity for methanol which is due to the high reactivity of the intermediates that undergo easily a further oxidation to CO and $CO_2$[3,9]. We mentioned in Chapter 1 that some of the present state-of-the art catalysts for this reaction are based on Fe and Cu, usually incorporated into a zeolite or MOF systems[10–12]. The choice of these two metals lies on the mimicking of natural Methane Mono Oxygenase (MMO) enzymes which convert methane to methanol at room temperature. More recently other copper-based formulations revealed to be interesting candidates for this reaction[13–15]. Among them, copper-ceria formulations have been considered for the low temperature methane activation[16,17]. It is well documented that $CuO/CeO_2$ catalysts showed comparable or even better catalytic performances compared to other precious-metal-based catalysts in a wide range of catalytic reactions such as CO oxidation[18], CO-prox[19] , water gas shift[20] and $N_2O$ decomposition[21]. The interesting catalytic activity of these materials derives from the strong electronic interactions occurring between copper and cerium oxide. Recently, Konsolakis[22] deeply reviewed the nature of this synergism, pointing out that several interrelated factors are usually considered under the definition of synergism such as (i) the facilitation of redox interplay between $Cu^{2+}/Cu^{+}$ and $Ce^{3+}/Ce^{4+}$ redox couples, (ii) the presence of defects, such as oxygen vacancies, (iii) the superior reducibility of the mixed $CuO\text{-}CeO_2$ composites with respect to the single counterparts, (iv) the geometric or ligand effects induced by the interaction of the metal with the support and (v) the peculiar reactivity occurring at the metal-support interface. Unfortunately, the study of these interactions is often difficult and elusive. The development of advanced in-situ and in-operando spectroscopic techniques gave important insights into the understanding of this interactions. In order to further rationalize these systems, in recent years inverse type catalysts gained considerable attention, since they provide useful information in the understanding of the specific role of ceria particles as well as of the oxide-metal interfacial sites in the catalytic properties[17,18,22,23].

In particular, Senanayake et. al.[17] reported a model inverse catalyst in which Ce was deposited via Physical Vapor Deposition (PVD) on a Cu(111) surface in presence of oxygen. This procedure led to a $CeO_2/Cu_2O/Cu$ material in which methane was activated at room temperature forming $CH_x$, $CO_x$ and C species on the surface that in presence of oxygen at a temperature of 177°C desorbed in the form of methanol together with large

amounts of CO and $CO_2$. An interesting finding described in the same work is represented by the pivotal role of water that pushes the system towards an outstanding methanol selectivity. This selectivity improvement was attributed to the occupation of the oxygen vacancies by water. This occupation inhibits the subsequent abstraction of protons from the adsorbed methane, thus leading to a minor formation of the major oxidation products. This system has demonstrated, thanks to a deep XPS characterization, the active role of the specific $Cu^{+}$-O-$Ce^{4+}$ redox couple in the whole reaction mechanism. The above work marked an important milestone in this area. However, the system they studied was a model system, prepared with a non-scalable synthetic technique. This inspired us to synthesize a catalyst that could contain a similar $Cu^{+}/Ce^{4+}$ active site with a more scalable technique. For this reason we exploited the mild energy ball milling technique for the preparation of a $CeO_2$/CuO composite, starting from the single oxides, CuO and $CeO_2$. The choice of a high surface area (has) cerium oxide was due to the high concentrations of $Ce^{3+}$ surface sites that are present on this support. The idea was to promote an electronic exchange between the surface $Ce^{3+}$ sites and the $Cu^{2+}$ sites of the support with the mechanochemical energy provided by the synthetic procedure:

$$Ce^{3+} + Cu^{2+} \rightarrow \text{mechanical energy} \rightarrow Ce^{4+} + Cu^{+}$$

As evidenced by Konsolakis and Senanayake[16,22] the research on the specific sites for methane activation must be accompanied by the use of advanced *in situ/operando* spectroscopic techniques. For this reason, in order to unveil the effectiveness of this procedure we made an extensive utilization of in-situ and operando techniques, in particular in-situ DRIFT and operando NEXAFS.

# 4.3. Experimental

## 4.3.1. Catalysts Synthesis

The milled catalysts were prepared by premixing the desired amounts of pre-calcined CuO and $CeO_2$ powders. The CuO was calcined at 650°C for 6 hours. We used two different High Surface Area supports in order to investigate both the effect of the surface area increase and the reproducibility of the synthesis over two different oxides. Specifically, a commercial ceria powder provided by Umicore with an active surface area of 120 $m^2/g$ and one synthesized in our laboratory with a surface area of 307 $m^2/g$ were used. These two supports have been previously calcined at 500°C and 350°C for 6 hours respectively. The amount of cerium oxide in the mixture was varied from 20% to 80% by weight. The homogenized powders were transferred in a 15mL zirconia jar together with a single zirconia ball (10 mm in diameter, 10 g weight). The powders were milled for 10 minutes at a frequency of 15Hz. After the milling step the powders were collected with the help of a brush to remove the powders from the jar. No calcination step was performed later since the two starting CuO and $CeO_2$ powders were already pre-calcined. With this technique the M $CeO_2$ CuO 2080, M $CeO_2$ CuO 4060, M $CeO_2$ CuO 6040 and M $CeO_2$ CuO 8020 catalysts were synthesized. A reference impregnated catalysts (I $CeO_2$ CuO 2080) with a 20% weight of $CeO_2$ was synthesized for comparison. In a 50 ml Becher a proper amount of Cerium nitrate (Treibacher) ($Ce(NO_3)_3 \cdot 6H_2O$) was dissolved in 45 mL of ethanol (Sigma-Aldrich). In this solution the proper amount (750 mg) of CuO was dispersed. The resulting suspension was gently heated until complete evaporation of the solvent. The resulting black powder was dried at 100°C for 12 hours prior to calcination at 400°C for 1 hour. The list of the synthetized samples is provided in Table 1.

**Table 1:** List of the prepared samples, M stands for Milled, I for Impregnated.

| Catalyst | Wt% $CeO_2$ | Wt% CuO | Mole % $CeO_2$ | Mole % CuO |
|---|---|---|---|---|
| I $CeO_2$ CuO 2080 | 20 | 80 | 6 | 94 |
| M $CeO_2$ CuO 2080 | 20 | 80 | 6 | 94 |
| M $CeO_2$ CuO 4060 | 40 | 60 | 14 | 86 |
| M $CeO_2$ CuO 6040 | 60 | 40 | 27 | 73 |
| M $CeO_2$ CuO 8020 | 80 | 20 | 49 | 51 |

The majority of the following experiments were conducted with the catalysts synthesized with the commercial $CeO_2$, unless otherwise specified. The samples prepared with our-self synthesized HSA $CeO_2$ will be distinguished by the HSA label, i.e. M $CeO_2$ CuO 2080 HSA.

### 4.3.2. Catalysts Characterization

Characterization of the materials was carried out by means of Brunauer–Emmett– Teller (BET) surface area measurements, X-ray diffractometry (XRD), temperature-programmed reduction (TPR), *in-situ* DRIFT and *in-operando* NEXAFS. For major details on the operative conditions see the experimental section (chapter 2).

## 4.4. Results and Discussion

### 4.4.1. XRD Analysis

Figure 1 shows XRD profiles of the M $CeO_2$ CuO 2080 sample prepared with the commercial support and the impregnated I $CeO_2$ CuO 2080, together with the single components, namely CuO an $CeO_2$. The analysis revealed the presence of the diffraction patterns of the cubic fluorite $CeO_2$ and of the monoclinic CuO in both catalysts. The CuO presented narrow and sharp peaks indicating a high crystallinity of the support. On the contrary, $CeO_2$, by virtue of its high surface area, presented broad peaks, symptomatic of small-size crystallites. The presence of broader $CeO_2$ peaks in the I $CeO_2$ CuO 2080 compared to the M $CeO_2$ CuO 2080 is likely due to its lower calcination temperature (400°C vs 500°C respectively), and it is symptomatic of smaller $CeO_2$ particles. No shifts in the peaks of $CeO_2$ and CuO were observed, indicating that solid solutions were not formed during milling.

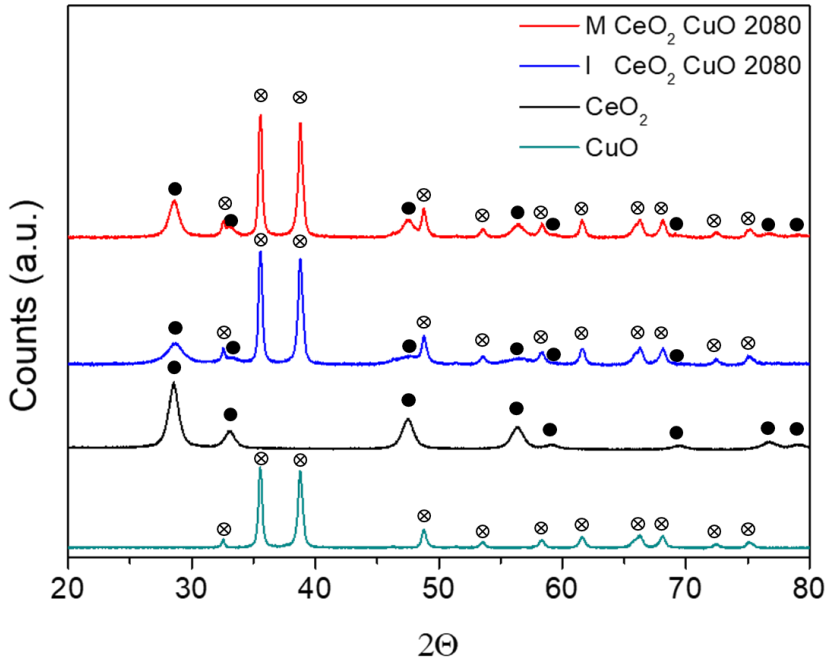


**Fig 1**: XRD analysis of the pure components of the synthesized materials and of the I $CeO_2$ CuO 2080 and M $CeO_2$ CuO 2080. Full circles (●) are related to the $CeO_2$ fluorite phase while the crossed circles (⊗) to the monoclinic phase of CuO.

The comparison of the milled samples with increasing $CeO_2$ content reported in Figure 2 showed a change in the relative intensities of the two components which depended on the composition. Also in this case no shifts in the peaks of $CeO_2$ and CuO were observed.

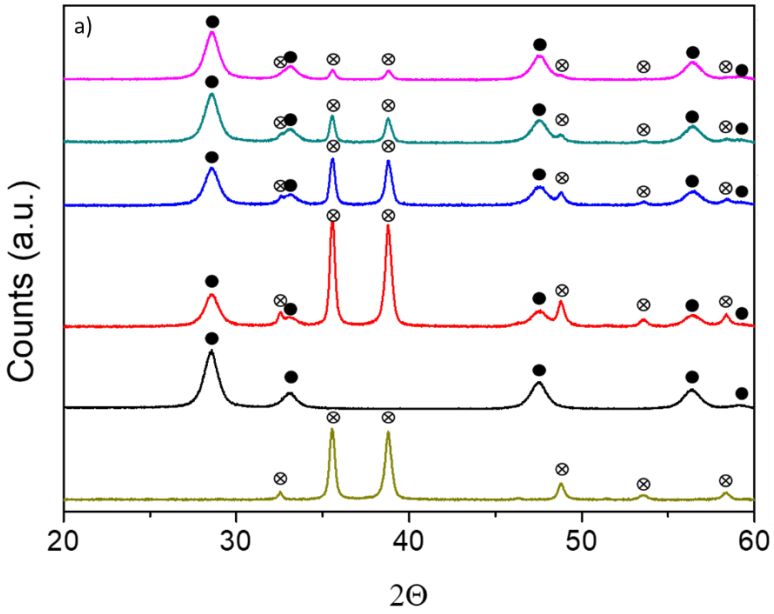


**Fig 2**: XRD analysis of the milled composites with increasing ceria content. Full circles (●) are related to the $CeO_2$ (black spectra) fluorite phase while the crossed circles (⊗) refer to the monoclinic phase of CuO (brown spectra); M $CeO_2$ CuO 2080 (red spectra), M $CeO_2$ CuO 4060 (blue spectra), M $CeO_2$ CuO 6040 (green spectra), M $CeO_2$ CuO 8020 (pink spectra).

Table 1 shows the average crystallites sizes calculated according to Scherrer's[24] from the line broadening of $CeO_2$ (111) and CuO (111) diffraction peaks. The results confirmed the presence of larger CuO particles of approximately 20 nm and smaller $CeO_2$ particle size. This is also affected by the preparation method with the I $CeO_2$ CuO 2080 showing the presence of smaller ceria crystallites of about 6nm while the milled samples, independently from the ceria loading, having crystallites of approximately 9nm. It is worth to notice that in the milled catalysts we did not observe appreciable variations in the crystallite size, suggesting that the adopted conditions for the milling process did not affect the primary structure of the oxides.

**Table 1:** mean particle size of the different precursors and composites calculated according to Scherrer's equation.

| Catalyst | Average CuO Particle Size (nm) | Average $CeO_2$ Particle Size (nm) |
|---|---|---|
| CuO | 19.5 | - |
| I $CeO_2$ CuO 2080 | 19.5 | 6.1 |
| M $CeO_2$ CuO 2080 | 19.9 | 8.6 |
| M $CeO_2$ CuO 4060 | 19.9 | 8.6 |
| M $CeO_2$ CuO 6040 | 20.4 | 8.8 |
| M $CeO_2$ CuO 8020 | 19.9 | 8.7 |
| $CeO_2$ | - | 8.7 |

## 4.4.2. Textural and Morphological properties

Table 2 summarizes the morphological characteristics from the $N_2$ adsorption/desorption experiments by means of BET surface area, average pore diameter and mean pore volume of the starting precursors and the synthesized $CeO_2$/CuO composites. The general trend of the BET surface area and the mean pore volume of the composite milled catalysts consist of an increase of value with the increase of $CeO_2$ content, while the average pore diameter decreases. These trends seem to be closely related with the composition of the catalysts.

**Table 2:** morphological properties of the starting precursors and synthesized catalysts.

| Catalyst | BET Surface Area ($m^2/g$) | Average Pore Diameter (Å) | Mean Pore Volume ($cm^3/g$) |
|---|---|---|---|
| CuO | 10 | 351 | 0.09 |
| I $CeO_2$ CuO 2080 | 20 | 266 | 0.15 |
| M $CeO_2$ CuO 2080 | 30 | 180 | 0.18 |
| M $CeO_2$ CuO 4060 | 50 | 150 | 0.26 |
| M $CeO_2$ CuO 6040 | 71 | 100 | 0.25 |
| M $CeO_2$ CuO 8020 | 92 | 108 | 0.33 |
| $CeO_2$ | 115 | 72 | 0.30 |

## 4.4.3. TPR characterization

Figure 3 shows the $H_2$-TPR profiles of the two I $CeO_2$ CuO 2080 and M $CeO_2$ CuO 2080 catalysts. The profile of the pure CuO support is reported for comparison and it shows three peaks labelled as α, β and γ. The low temperature α peak at 178°C was attributed to the reduction of highly dispersed CuO, while the β and γ peaks at 263°C and 282°C were assigned to the reduction of medium-size CuO and bulk CuO respectively[25–28]. The shift and the profile of our inverse Impregnated catalysts corresponded to the one reported by Avgouropoulos et al. for a classic CuO/$CeO_2$ catalyst (i.e. non inverse) prepared with similar preparation approaches[29].

The two catalysts showed a shift of the lower temperature of the reduction peak of bulk CuO, indicating that the reducibility of copper was slightly promoted due to the strong interaction at the interface between the two materials, independently on the synthetic method[28,30].

No appreciable differences were observed between the two catalysts synthesized from the two different synthetic methods, which showed, at approximately 450°C and 700°C (Figure 3c), the presence of two reduction peaks which were ascribed to the reduction of surface and bulk ceria respectively[31,32]. In the impregnated catalyst the surface reduction peak appeared more intense compared to the corresponding milled composite. This could be explained with the difference in the calcination temperature of $CeO_2$ in the two synthesis: in the case of the I $CeO_2$ CuO 2080 catalysts, after impregnation and drying at 100°C the composite was calcined at 400°C for 1 hour, while the milled catalyst was synthesized which was calcined at 500°C prior to the synthesis.

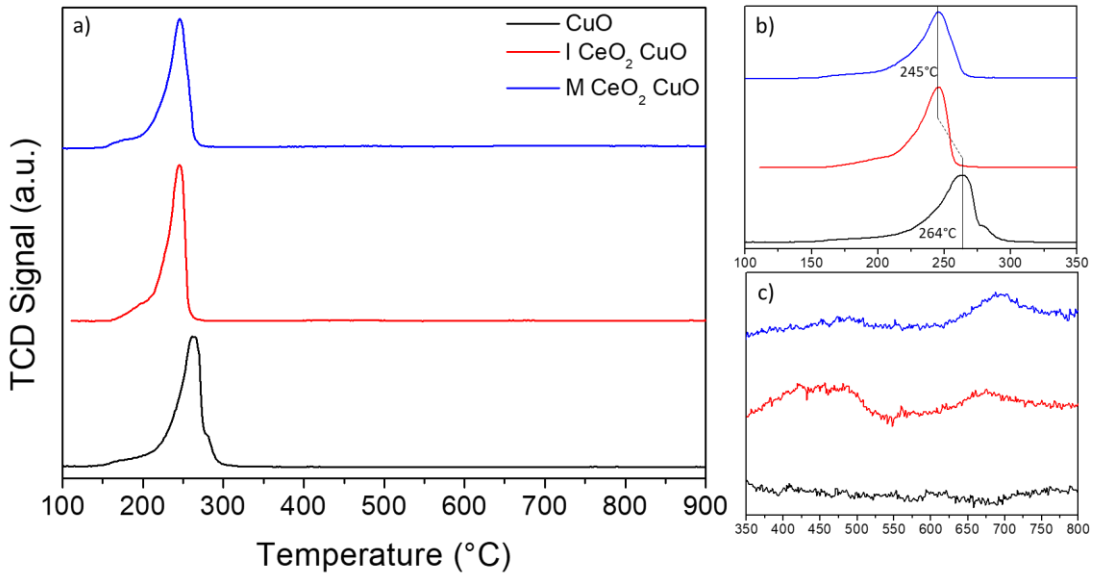


**Figure 3:** $H_2$-TPR profiles of the CuO support and of the I $CeO_2$ CuO 2080 and M $CeO_2$ CuO 2080 catalysts; a) full profile; b) detail of the CuO reduction window; c) detail of the $CeO_2$ reduction window.

In figure 4 the comparison between the milled samples obtained by increasing the $CeO_2$ content by weight is reported. It is possible to observe that the $CeO_2$ loading influenced the reduction of both the CuO and $CeO_2$ phases. The most evident effect is the shift at lower temperature of the main reduction peak of CuO as already observed in the milled sample with 20% wt. ceria compared to pure CuO. By increasing the ceria content, the shift became more significant, as it is possible to observe in figure 4b; the most consistent shift (35°C) was observed between the M $CeO_2$ CuO 6040 and the M $CeO_2$ CuO 8020, while the differences between the other samples were around the 15-20°C. This phenomenon is reasonably explained with the fact that the more the ceria content the more the reduction of CuO is promoted due to the strong interaction between the two materials. In all the milled catalysts the reduction of bulk $CeO_2$ is shifted to lower temperatures compared to pure commercial $CeO_2$.[26] Looking at Fig. 4c it is possible to observe the opposite trend regarding the reduction of bulk $CeO_2$ since an increase in the reduction temperature was observed with the increasing ceria content. A similar trend for classic CuO-$CeO_2$ catalysts with increasing CuO content was reported by Mariño et.al.[25]. It is possible to hypothesize that in the catalysts with lower $CeO_2$ contents (M $CeO_2$ CuO 2080 and M $CeO_2$ CuO 4060) the ceria particles are well in contact and covered with the CuO phase and thus, by maximizing the interfacial surfaces, more prone to reduction

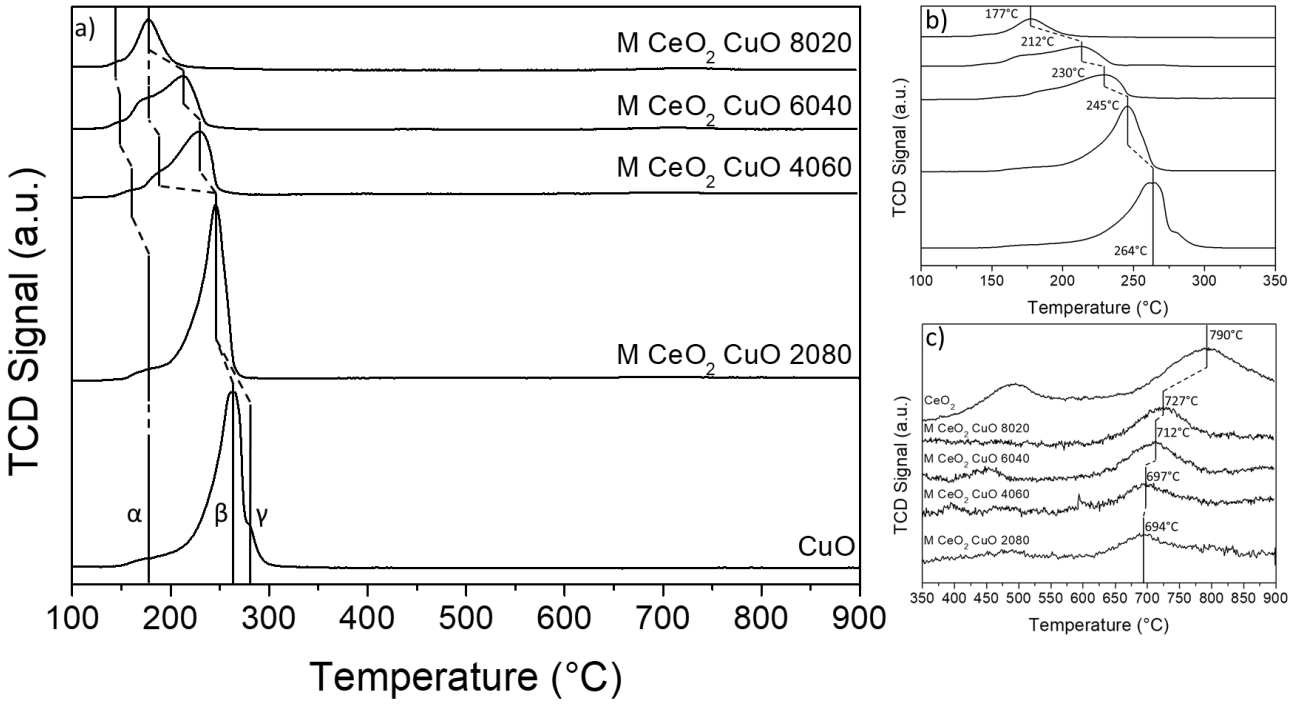


**Figure 4:** $H_2$-TPR profiles of the CuO support and of the and M $CeO_2$ CuO catalysts with increasing cerium oxide contents; a) full profile; b) detail of the CuO reduction window; c) detail of the $CeO_2$ reduction window.

A second analysis on the CuO reduction peak, reported in Fig. 4a, allows us to observe a complexity in the peak structure with the increasing ceria content. It is possible to observe in the M $CeO_2$ CuO 4060 and M $CeO_2$ CuO 6040 the re-appearance of the β peak which shifted more than the γ peak of reduction of bulk CuO in these two samples. In the M $CeO_2$ CuO 8020 the γ peak is shifted consistently due to the high ceria content resulting again overlapped with the β peak. While the nature of alfa and gamma peaks is well established in literature[33], the nature of the β peak is more debated.

Djinović et.al.[34] and Marino et.al.[25] reported a similar complex structure of the low temperature peak in their TPR profile in a series of classic (i.e. non inverse) CuO-$CeO_2$ catalysts synthesized by co-precipitation method. The lower temperature component was assigned to the reduction of finely dispersed CuO species, while for the higher temperature components a contribution of surface $CeO_2$ reduction at the interface of the two materials was established from the quantitative analysis. Interestingly they observed the same major shift to lower temperature for their higher ceria content catalysts.

Avgouropoulos et al.[27,29] attributed the first peak to the reduction of highly dispersed CuO in strong interaction with the ceria surface, while the β and γ peaks to the reduction of larger CuO particles less associated with the ceria.

Zeng et. al. reported a similar trend for these systems synthesized with a surfactant templated method by increasing the Ceria molar content[35] for a series of classic and reverse catalysts, and they attributed the β peak to the presence of CuO in the ceria lattice[33,36].

From the XRD analysis we excluded the formation of a solid solution between the two materials and therefore we assigned the three components described in this paragraph to the reduction of small, medium-sized and bulk CuO. We found that the shift of the total reduction peak of CuO depends more on the cerium content than to the preparation method since, from the comparison of the I $CeO_2$ CuO 2080 and M $CeO_2$ CuO 2080 we observed the same shift.

Given the stoichiometry of reduction of the CuO by $H_2$:

$$CuO + H_2 \rightarrow Cu + H_2O$$

for the reduction of only CuO, we expect a Stoichiometric Ratio ($S_r$)

$$S_r = \frac{Moles\ of\ consumed\ Hydrogen}{Moles\ of\ Copper} = 1$$

The results of the quantitative analysis are reported in table 3. It is possible to observe that we obtained a slightly lower value of $S_r$ for pure CuO. Regarding the synthesized materials we observed an almost identical value for the I $CeO_2$ CuO 2080 catalyst. Regarding the milled catalysts we observed values of $S_r$ which seem to be dependent on the $CeO_2$ loading. For the M $CeO_2$ CuO 2080, M $CeO_2$ CuO 4060 and M $CeO_2$ CuO 6040

we observed slightly lower values of $S_r$ compared to the one of pure CuO. For the M $CeO_2$ CuO 8020 catalysts we observed an higher value of $S_r$ respect to the one of pure CuO, likely because of the major contribution of surface ceria.

**Table 3:** ratio between moles of consumed hydrogen and moles of Copper of the synthesized catalysts.

| Catalyst | $S_r$ First Cycle |
|---|---|
| CuO | 0.90 |
| I $CeO_2$ CuO 2080 | 0.91 |
| M $CeO_2$ CuO 2080 | 0.85 |
| M $CeO_2$ CuO 4060 | 0.83 |
| M $CeO_2$ CuO 6040 | 0.85 |
| M $CeO_2$ CuO 8020 | 0.96 |

## 4.4.4. *In-situ* DRIFT Analysis

### 4.4.4.1. CuO

We started the DRIFT study of our materials with the analysis of the two single components, CuO and $CeO_2$. In figure 5 the reactivity of CuO towards two reaction mixtures is reported. For experimental details see chapter 2.2.9.. The spectra were collected by subtracting the background signal at the temperature of 250°C under pure He. Fig. 5a shows the reactivity of CuO toward methane (10% $CH_4$/He mixture). It is possible to see that the material is inert to this reaction mixture, since the presence of any peak related to the adsorption of methane was detected neither during the exposure of the sample to the methane atmosphere nor to a successive exposure to helium. The marked peaks at 3014 and 1307 $cm^{-1}$, are related to gas phase methane. Figure 5b shows the reactivity of CuO towards a mixture of 10% $CH_4$/5% $O_2$/He. Despite the presence of oxygen in the reactants no differences were detected with respect to the previous case described. However, it is possible to observe a different behavior for the broad bands centered at approximately 1470 and 1120 $cm^{-1}$ . These two bands were positive when the CuO was exposed in $CH_4$ and negative when exposed simultaneously to $CH_4$ and $O_2$.

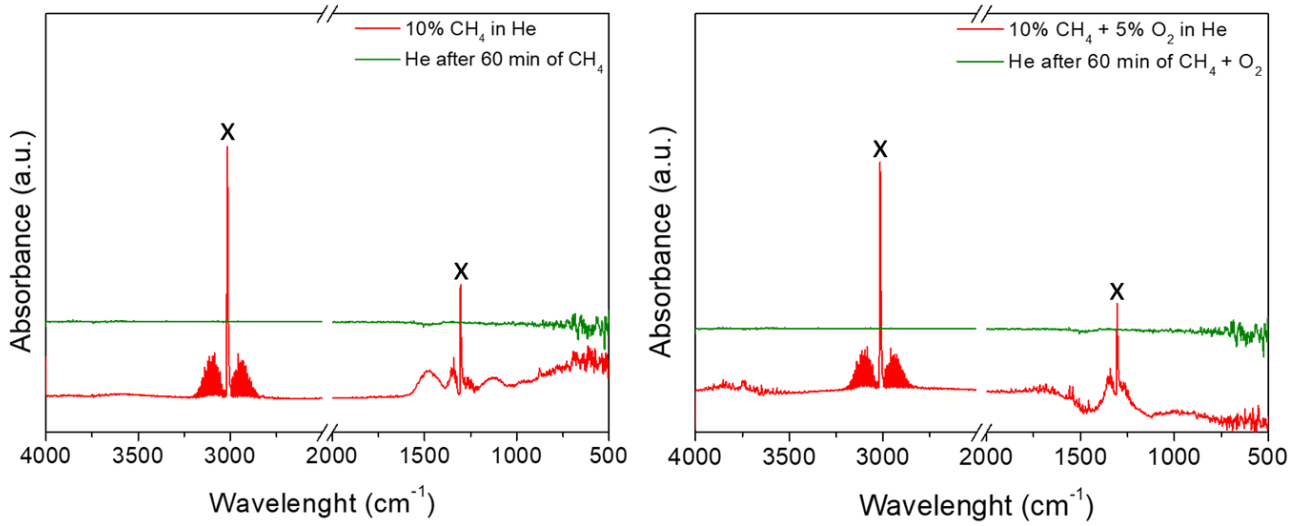


**Figure 5:** In situ DRIFT results of the exposure of CuO in different atmospheres at 250°C: a) exposure in 10% $CH_4$/He (red spectra) and in pure He after 60 minutes of exposure in 10% $CH_4$/He (green spectra); b): exposure in 10% $CH_4$/5% $O_2$/He (red spectra) and in pure He after 60 minutes of exposure in 10% $CH_4$/5% $O_2$/He (green spectra).

In order to understand the nature of the above signals, we performed additional experiments by varying the atmosphere during the pre-treatment step. In Figure 6 the spectra of the sample after 10 minutes of exposure to three different atmospheres at the pre-treatment temperature of 300°C are reported. These spectra were collected by subtracting the background spectrum taken at room temperature. By consequence, the resulting spectra were characteristics of the CuO material. It is possible to see in the figure below that the two bands of interest are present, together with other characteristic bands of CuO, in all the three spectra, with intensities which are dependent on the different atmospheres. This showed that the two bands are characteristics of CuO.

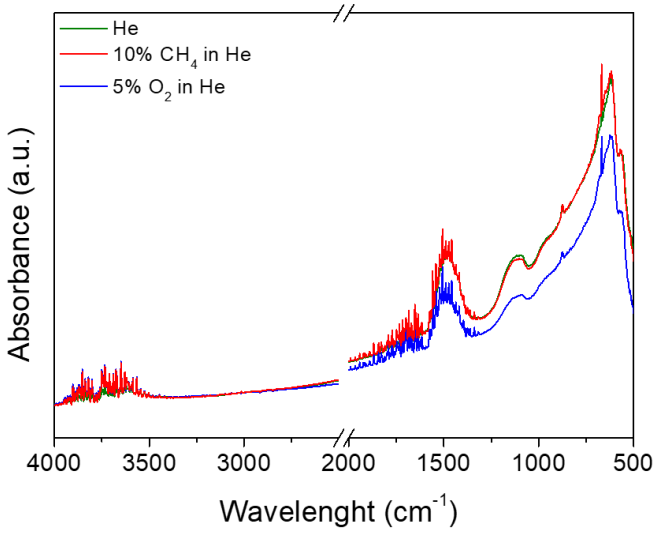


**Figure 6**: Spectra of CuO after 10 minutes of exposure to pure Helium (green spectra), 10% $CH_4$/He (red spectra) and 5% $O_2$/He (blue spectra) at 300°C.

We then performed some experiments at 250°C after subtracting the background of the sample taken in pure He. We observed that the different atmosphere of pre-treatment had an effect in the spectra collected during the subsequent experiments. In figure 7 it is possible to see, concerning the spectra referred to the pre-treatment in pure helium (green spectra), that the behaviour of the two bands was the same observed in figure 5, i.e. the bands were positive during the exposure of the sample in 10% $CH_4$/He and negative during the exposure in 5% $O_2$/He. An almost identical behavior was observed in the sample pre-treated in 10% $CH_4$/He, while major differencies were detected in the case of the 5% $O_2$/He pre-treatment. In this latter case it is possible to see from Figure 7a that the intensity of the bands was enhanced compared to the other pre-treatments, while in the second step of the experiment, i.e. the exposure of the sample in 5% $O_2$/He at 250°C, the two bands were absent.

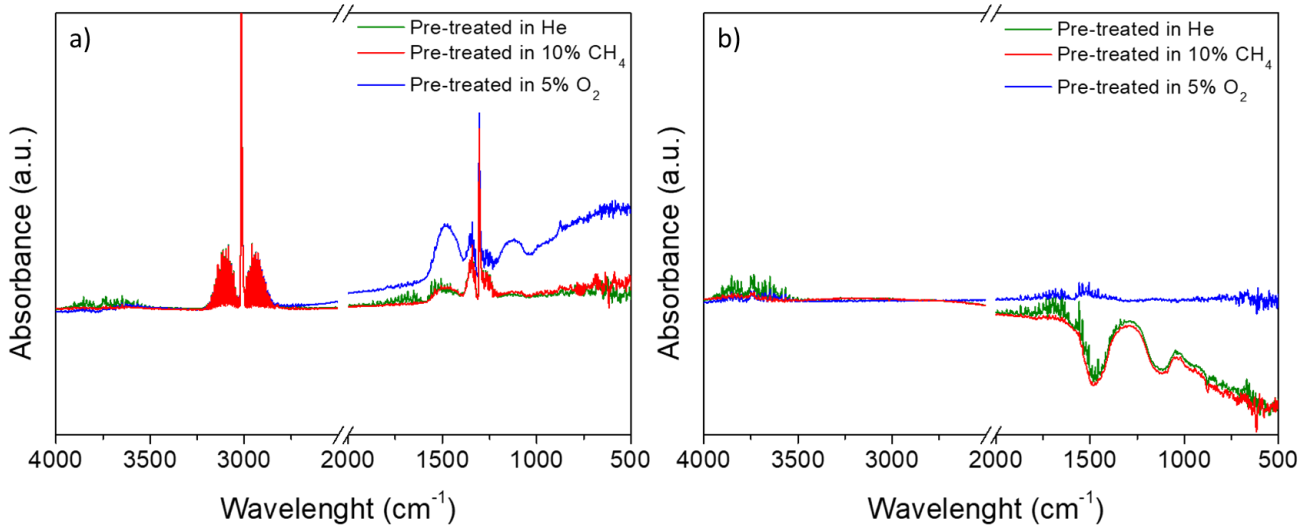


**Figure 7**: effect of the pretreatment atmospheres; a) spectra collected after exposure to 10% $CH_4$/He for 20 minutes at 250°C and b) spectra collected after exposure to 5% $O_2$/He for 20 minutes at 250°C.

The above analysis was limited to the identification of the two bands belonging to CuO. No further analysis was carried out on this matter.

All the spectra that will be discussed in the next paragraphs were collected by subtration of the background taken in He at 250°C after a pre-treatment in pure He at 300°C.

#### 4.4.4.2. $CeO_2$

Thanks to its exceptional oxygen storage/release properties, cerium oxide is extensively investigated for the direct partial oxidation of methane[37,38]. However, the activation and oxidation of methane in the absence of molecular oxygen occurs at higher temperatures than those investigated in our experiments. In Figure 8 the reactivity of pure $CeO_2$ towards two different reaction mixtures is reported. It is possible to see in Figure 8a that, in agreement with our expectations, pure ceria is substantially inert to 10% $CH_4$/He mixture, since no appreciable signals were detected after the removal of the reactant mixture at which the sample was exposed for 60 minutes. However, as we can see in Figure 8b, $CeO_2$ behaves differently when exposed to a mixture of 10% $CH_4$/5% $O_2$/He, since the presence of activated methane was clearly detected afer 60 minutes of exposure to the latter reaction mixture. The fact that these peaks were not detected after exposure of the $CeO_2$ sample in methane only means that lattice oxygen of the pure ceria is not sufficient to activate methane at 250°C, which needs the presence of molecular oxygen in the exposing atmosphere.

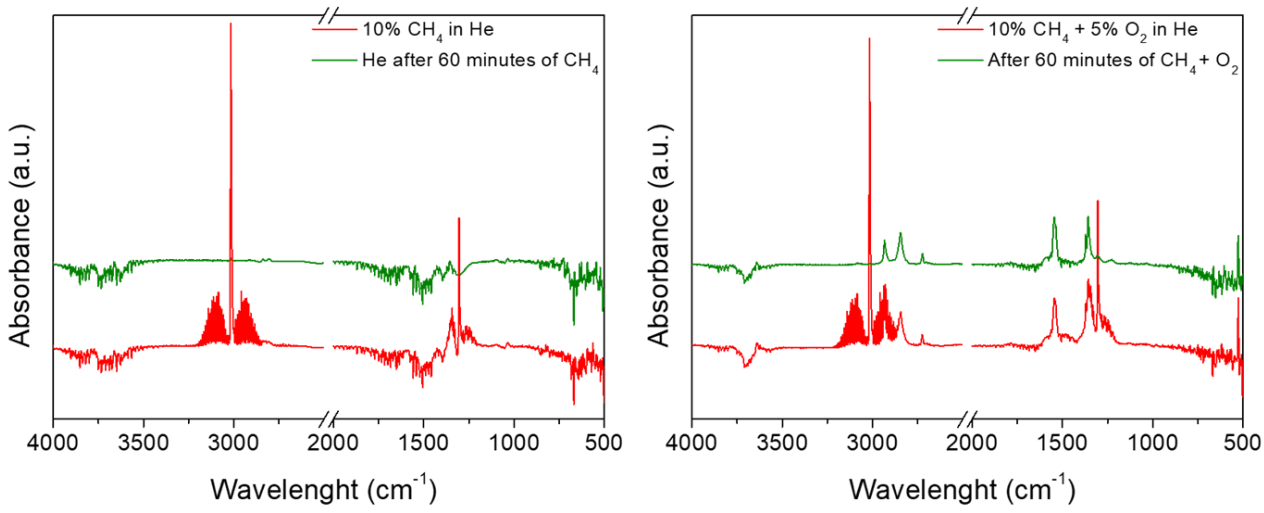


**Figure 8:** In situ DRIFT results of the exposure of $CeO_2$ in different atmospheres at 250°C: a) exposure in 10% $CH_4$/He (red spectra) and in pure He after 60 minutes of exposure in 10% $CH_4$/He (green spectra); b) exposure in 10% $CH_4$/5% $O_2$/He(red spectra) and in pure He after 60 minutes of exposure in 10% $CH_4$/5% $O_2$/He (green spectra).

In Figure 9 the spectra recorded after the exposure of the sample to 10%$CH_4$/5%$O_2$/He is reported along with the corresponding assigned adsorbed species. A punctual assignment of the peaks is reported in Table 4. It is possible to observe that most of the peaks have been assigned to formate and methoxy species which came from the partial oxidation of methane chemisorbed on the ceria surface with oxygen. These species are in agreement with those identified previously after the study of the adsorption of formaldehyde and methanol on cerium oxide[39,40]. Formates are characterized by the peaks at 2931 $cm^{-1}$ (v-CH), 1548 $cm^{-1}$ (v-C=O) and 1359 (bending CH), while methoxy groups are characterized by the peak at 2842 $cm^{-1}$ (v-CH), 1458, 1371 and

1356 $cm^{-1}$ (bending CH)[39–42]. The peaks at 1583 $cm^{-1}$, 1516 $cm^{-1}$, 1308 $cm^{-1}$ , 1225 $cm^{-1}$, and 1031 $cm^{-1}$ have been attributed to adsorbed carbonates and hydroxycarbonates[42–44]. The OH zone was characterized by a negative peak at 3700 $cm^{-1}$ related to the desorption of some residual water from the surface of the material and a sharp peak at 3640 $cm^{-1}$ along with a broad peak at 3519 $cm^{-1}$, which were assigned to the bi- and tri-coordinated hydroxyl groups respectively[45,46].

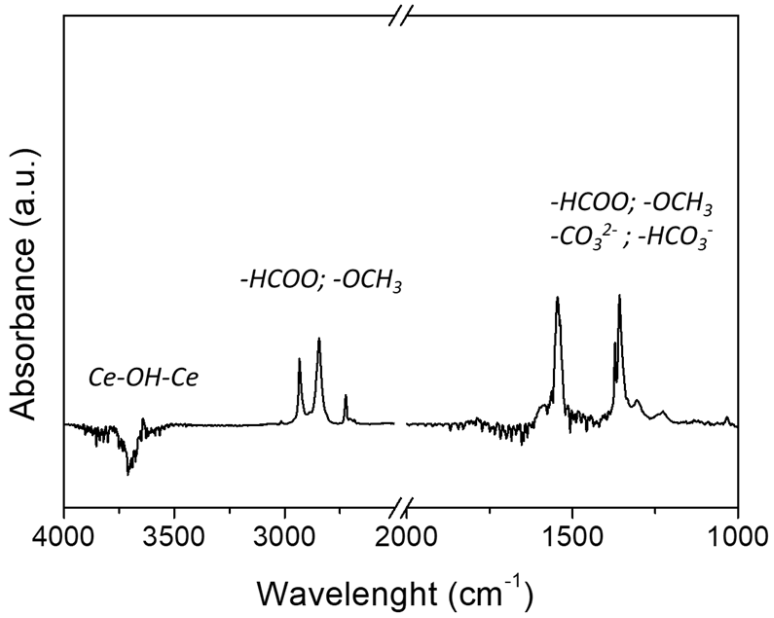


**Figure 9:** spectra of cerium oxide after 60 minutes of exposure to 10% $CH_4$/5% $O_2$/ He atmosphere at 250°C.

**Table 4:** Assignments of the main IR bands observed during methane partial oxidation on pure ceria according to Refs. 39-46.

| | Label | Wavenumber ($cm^{-1}$) | Vibrational mode |
|---|---|---|---|
| Hydroxy | *-OH* | | |
| | | 3640 | Stretching O-H |
| Formate | *-OOCH* | | |
| | | 2931 | Stretching C-H |
| | | 2720 | Stretching C-H |
| | | 1548 | Stretching C-O |
| | | 1359 | Bending C-H |
| Methoxy | *-$OCH_3$* | | |
| | | 2842 | Stretching C-H |
| | | 1458 | Bending C-H |
| | | 1371 | Bending C-H |
| | | 1356 | Bending C-H |
| Bidentate Carbonate | *-$CO_3^{2-}$* | | |
| | | 1458 | Bending C-H |
| | | 1516 | |
| | | 1031 | |
| Hydrogen carbonate | *-$HCO_3^-$* | | Bending C-H |
| | | 1583 | |
| | | 1226 | |
| | | 1308 | |

In Figure 10 a detailed representation of the evolution of the material during the different phases of the experiment is reported. It is possible to observe that during the exposure of the sample in the mixture there was a constant increase in intensity of the peaks described above with the time of exposure. When the reactant mixture was substituted with an inert atmosphere the intensity of the peaks did not change, indicating that the adsorbed species were stable at the reaction temperature of 250°C. We then treated the sample under atmosphere containing only 5% $O_2$/He in order to evaluate the behavior in oxidizing atmosphere. We did not observe any desorption of the described species, indicating that they were stable, even after 70 minutes of exposure.

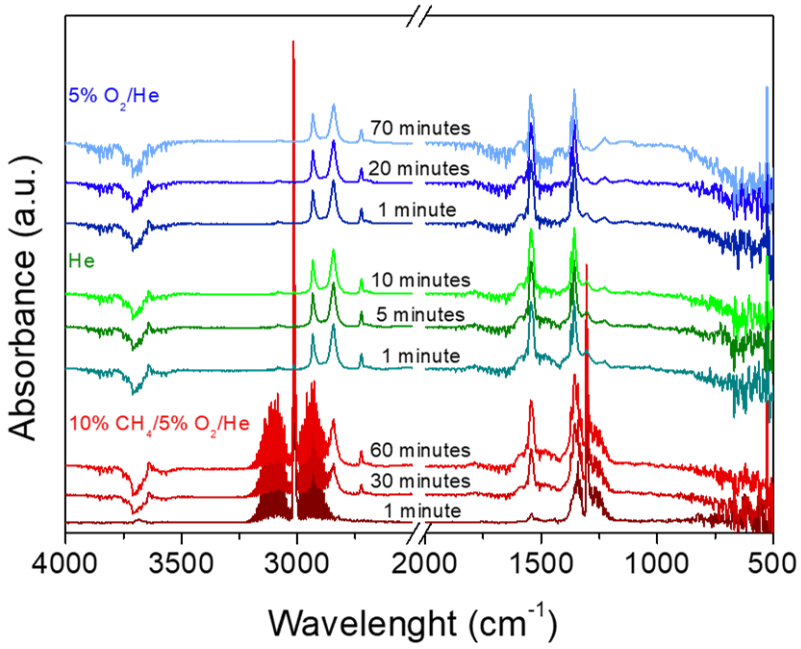


**Figure 10:** detailed representation of the experiment conducted on the pure $CeO_2$ at 250°C: exposure in 10%$CH_4$/5%$O_2$/ He (shades of red), pure He (shades of green), 5%$O_2$, He (shades of blue).

To evaluate the reliability of the results we performed the same experiment on a HSA $CeO_2$ support synthesized in our laboratory with the procedure reported in Chapter 3, with a specific surface area of 307 $m^2/g$. Results reported in Figure 11a indicate that this support shows the same behavior as commercial ceria with adsorption bands that are stable and appears only after exposure to methane and oxygen. In Figure 11b it is possible to see that the peaks were the same in the two supports, which however showed some negligible differences, especially regarding the relative intensities. These differences could be explained with the different surface areas of the support and with the different preparation methods.

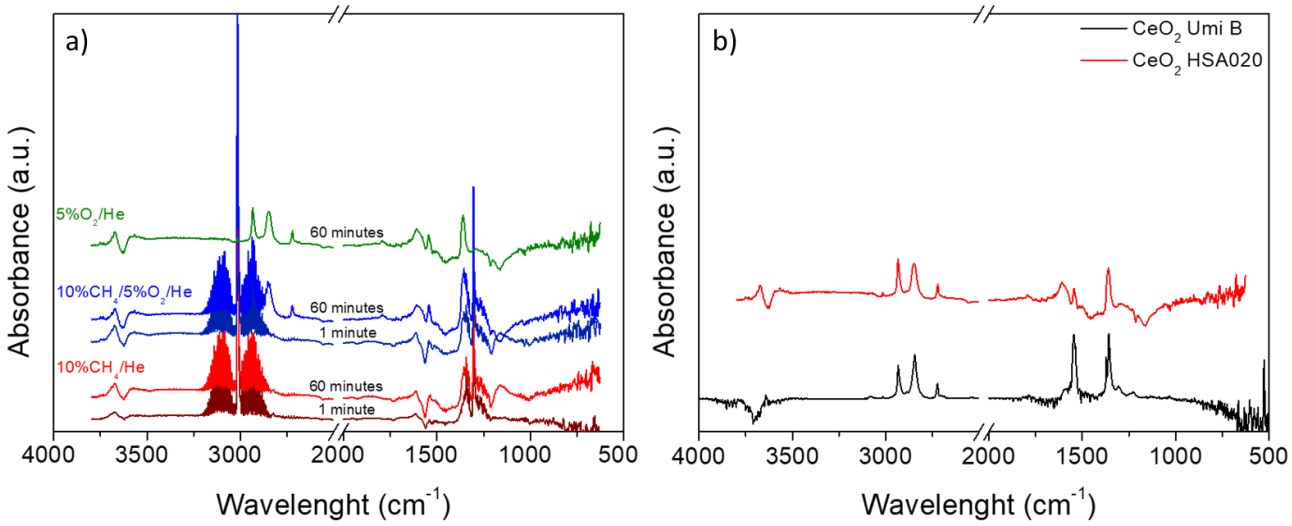


**Figure 11:** a) replica of the above-described experiment on a different support; b) comparison between the two different supports after 60 minutes of exposure to 10% $CH_4$/5%$O_2$/He at 250°C.

## 4.4.4.3. I $CeO_2$ CuO 2080

We started the analysis on the synthesized materials with the impregnated sample which showed no activity towards the two gas mixtures, as observed in Figure 12. Its behavior is similar to the one shown for pure CuO indicating that in the I $CeO_2$ CuO 2080 the presence of the supported $CeO_2$ does not affect the properties of the pure copper oxide.

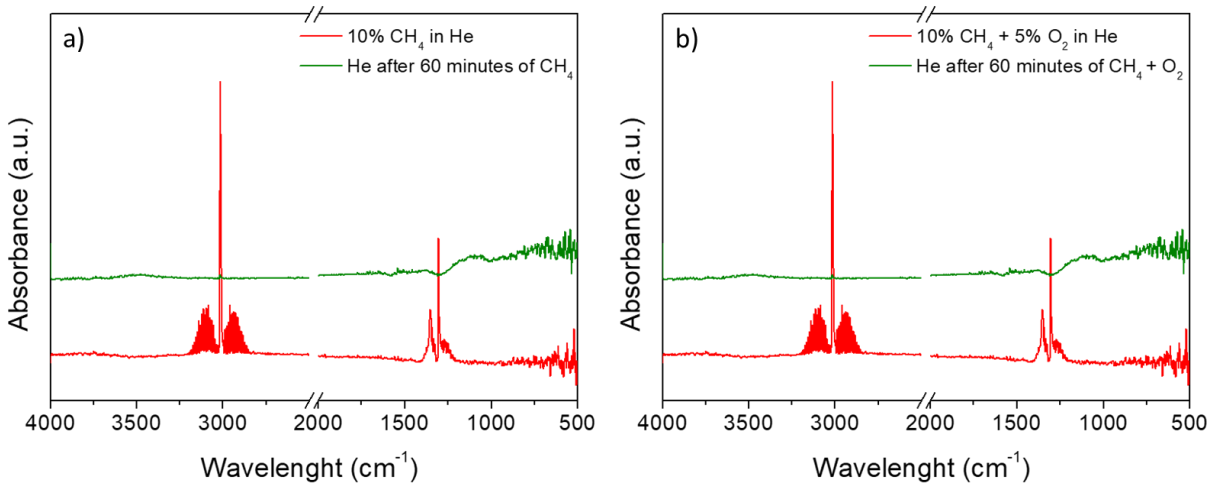


**Figure 12.** In situ DRIFT results of the exposure of the I $CeO_2$ CuO 2080 in different atmospheres at 250°C: a) exposure in 10% $CH_4$/He (red spectra) and in pure He after 60 minutes of exposure in 10% $CH_4$/He (green spectra); b) exposure in 10% $CH_4$/5% $O_2$/He (red spectra) and in pure He after 60 minutes of exposure in 10% $CH_4$/5% $O_2$/He (green spectra).

#### 4.4.4.4. M $CeO_2$ CuO 2080

M $CeO_2$ CuO 2080 showed a peculiar behavior in comparison to that described for the pure oxides and the corresponding impregnated catalyst. In fact, in this sample we observed the appearance of some bands related to the presence of partial oxidized methane intermediates after 60 minutes of exposure to 10% $CH_4$/He at 250°C (Figure 13). The intensity of these peaks is quite low, but this was the only sample that showed an affinity to pure methane. The previous analysis has showed the adsorption of methane on pure ceria, but only in the presence of oxygen.

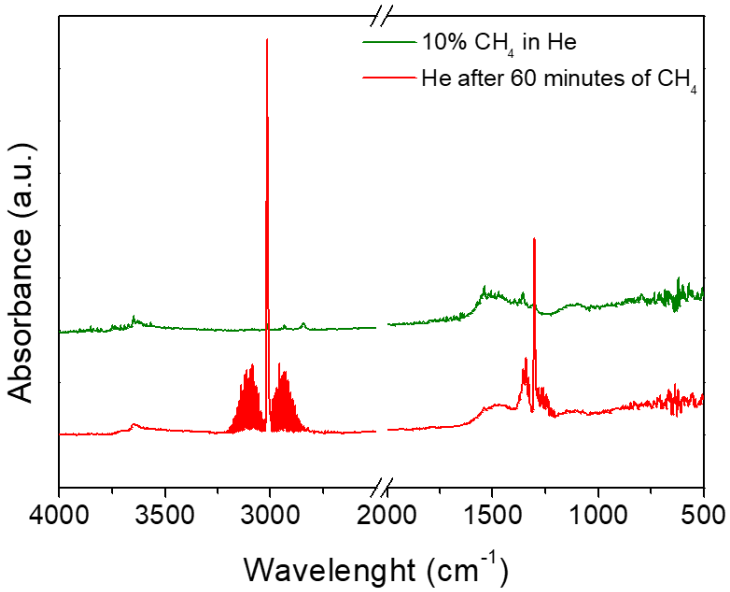


**Figure 13:** In situ DRIFT results of the exposure of the M $CeO_2$ CuO 2080 in 10% $CH_4$/He(red spectra) and in pure He after 60 minutes of exposure in 10% $CH_4$/He (green spectra) at 250°C.

This was a significant difference, and we compared the peaks observed in the M $CeO_2$ CuO 2080 and the peaks observed in the pure $CeO_2$ after 60 minutes of exposure in methane and oxygen (Figs. 8 and 9). In figure 14 it is possible to see that the position of the peaks is the same in the two samples, while the intensity is much lower in the M $CeO_2$ CuO 2080 sample, which, however, has a $CeO_2$ content of 20%. The fact that the peaks position is the same in the two samples implies that the methane species are adsorbed on the ceria surface indicating that the milled composite must possess a peculiar active site responsible for methane activation, since none of the single components showed the same behavior when exposed to methane only. The sites are likely to be formed by a particular interaction of Cu and Ce induced by the adopted mechanochemical approach.

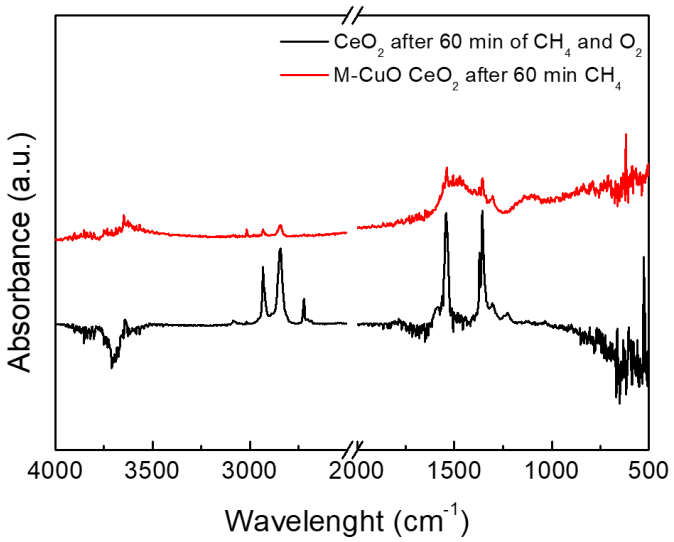


**Figure 14:** Comparison of the in situ DRIFT spectra of the pure $CeO_2$ sample after exposure in 10% $CH_4$/5% $O_2$/He (black spectra) and of the M $CeO_2$ CuO 2080 after exposure in 10% $CH_4$/He (red spectra) at 250°C.

By performing the same experiment on the M $CeO_2$ CuO 2080 HSA, we obtained the same results, as it is possible to see in figure 15; thus confirming the reliability of the synthetic procedure and the reproducibility of the observed phenomenon.

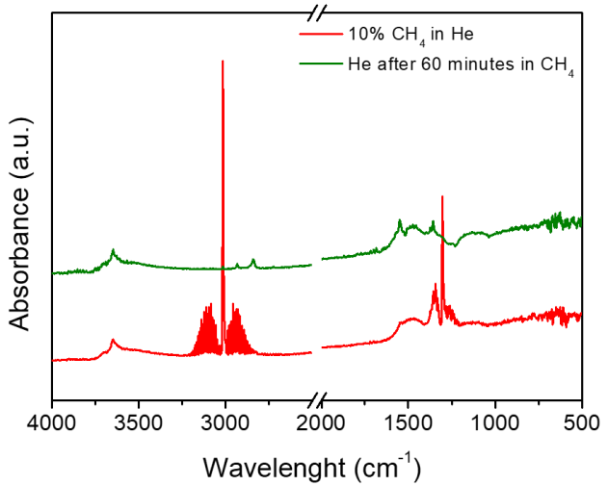


**Figure 15:** In situ DRIFT results of the exposure of the M $CeO_2$ CuO 2080 HSA in 10% $CH_4$/He (red spectra) and in pure He after 60 minutes of exposure in 10% $CH_4$/He (green spectra) at 250°C.

If we look at the comparison between the two milled samples reported in Figure 16 it is possible to see that the peaks are more intense in the sample obtained from the M $CeO_2$ CuO 2080 HSA, suggesting that the specific sites formed where correlated with the specific surface area of cerium oxide. Because of the higher

abundance of $Ce^{3+}$ with the increase of surface area of $CeO_2$, we could hypothesize a specific role of these sites in the formation of the active sites of the composite.

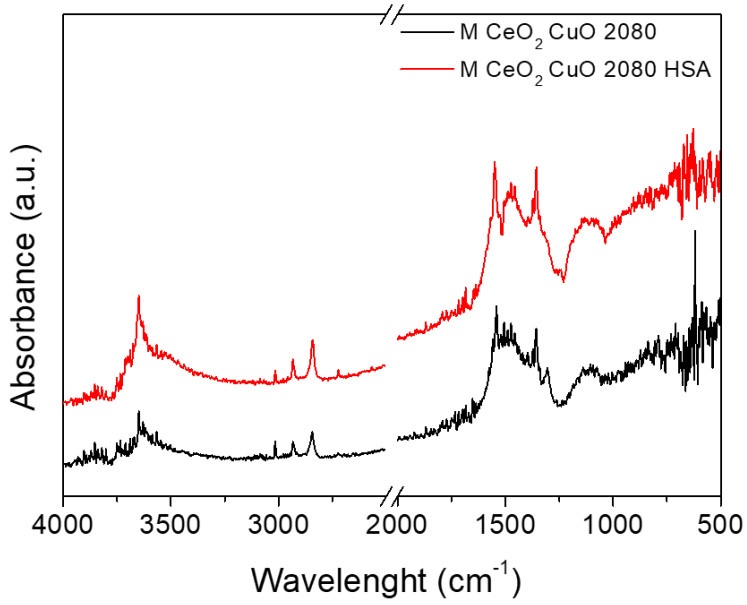


**Figure 16:** comparison between the two M $CeO_2$ CuO 2080 samples after 60 minutes of exposure to 10% $CH_4$/He at 250°C: commercial $CeO_2$ (black spectra) and High Surface Area (HSA) $CeO_2$ (red spectra).

Moreover, considering a dissociative breaking of the C-H bond of the methane prior to its adsorption it is reasonable to find some differences between the pure ceria and the milled composite in the OH stretching zone of the DRIFT spectra. A confirmation of the presence of these peculiar sites in the milled composite derives from the analysis reported in figure 17. We can observe a peak at 3640 $cm^{-1}$ in the pure ceria which is ascribed to the Ce-OH-Ce[45,46] while in the composite this peak is shifted at 3650 $cm^{-1}$. This small shift could be due to a different local environment, which can be likely associated to a Cu-OH-Ce species, which is the active site of interest. The presence of the shoulder at 3700 $cm^{-1}$ was related to the formation of adsorbed water[46].

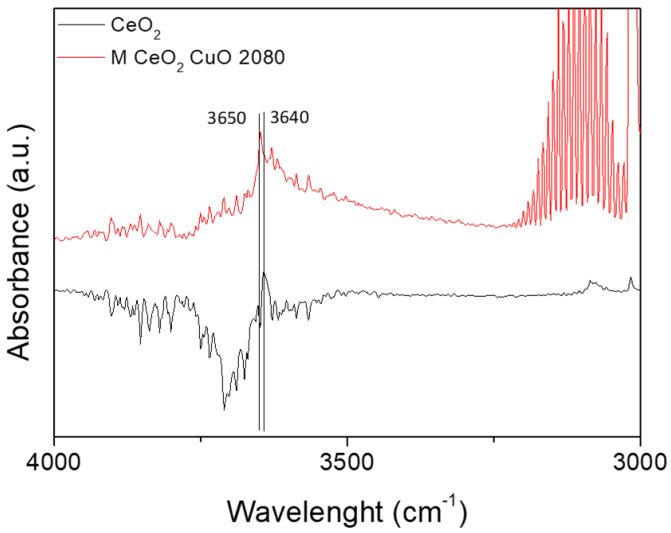


**Figure 17:** detail of the OH stretching zone of the DRIFT spectra collected at 250°C: comparison between pure $CeO_2$ after exposure of 60 minutes in 10%$CH_4$/5%$O_2$/He and M CuO $CeO_2$ after exposure of 60 minutes to 10%$CH_4$/He.

We then evaluated the stability of the adsorbed species in pure helium and in 5% $O_2$/He. The adsorbed species were stable in pure He since no drop in the peak intensity was observed after 10 minutes. After sending 5%$O_2$/He, we observed a fast decrease in intensity and, after 10 minutes, the total disappearance of the peaks, indicative of a desorption of the species (Figure 18).

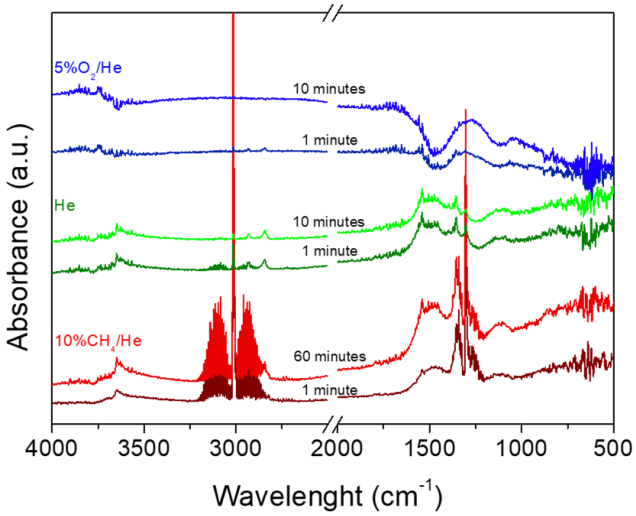


**Figure 18**: detailed representation of the experiment conducted on the M $CeO_2$ CuO 2080 sample at 250°C: exposure in 10%$CH_4$/5%$O_2$,/He (shades of red), pure He (shades of green), 5%$O_2$/ He (shades of blue).

Similar behavior was observed also in the M $CeO_2$ CuO 2080 HSA with a gradual decrease in intensity of the peaks related to the adsorbed species. The complete desorption was observed after 15 minutes, slightly longer to the 10 minutes observed in the same sample synthesized with the commercial $CeO_2$ (120 $m^2/g$). This confirmed the effect of surface area on the reactivity of the materials, which however showed the same general behavior, indicating once again the reproducibility and reliability of the synthesis.

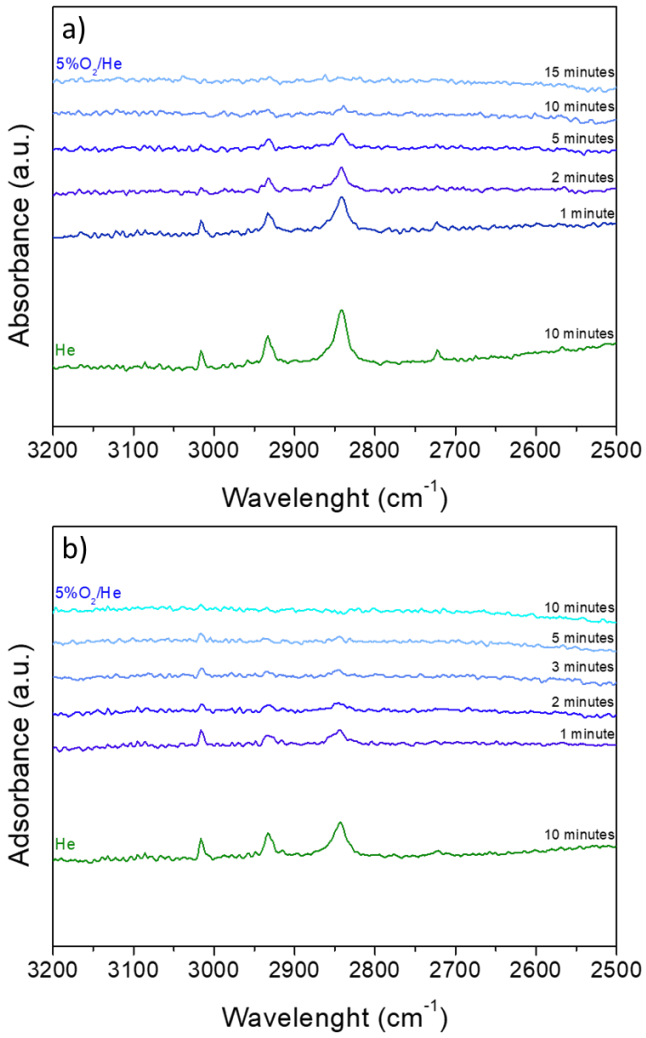


**Figure 19**: detailed representation of the experiment conducted, at the temperature of 250°C, on the M $CeO_2$ CuO 2080 sample synthesized with the HSA (a) and commercial (b) cerium oxide: exposure to pure He after exposure to 10%$CH_4$/He (green), 5%$O_2$/ He (shades of blue). The 3200-2500 $cm^{-1}$ window is representative for all the spectrum.

#### 4.4.4.5. Milled samples with higher $CeO_2$ contents

By increasing the $CeO_2$ content we observed a linear increase in intensity of the peaks related to the adsorbed species (Figure 20).

The adsorbed species in the M $CeO_2$ CuO 4060 sample showed the same behavior observed in the M $CeO_2$ CuO 2080 in 5%$O_2$/He atmosphere, but in this case the complete desorption occurred in approximately 20 minutes, which is the double of the time that occurred to the same sample with $CeO_2$ weight content of 20%. This means that for these two samples there is a linearity between $CeO_2$ content and desorption time. The comparison of the desorption phase in the two samples is reported in Figure 21.

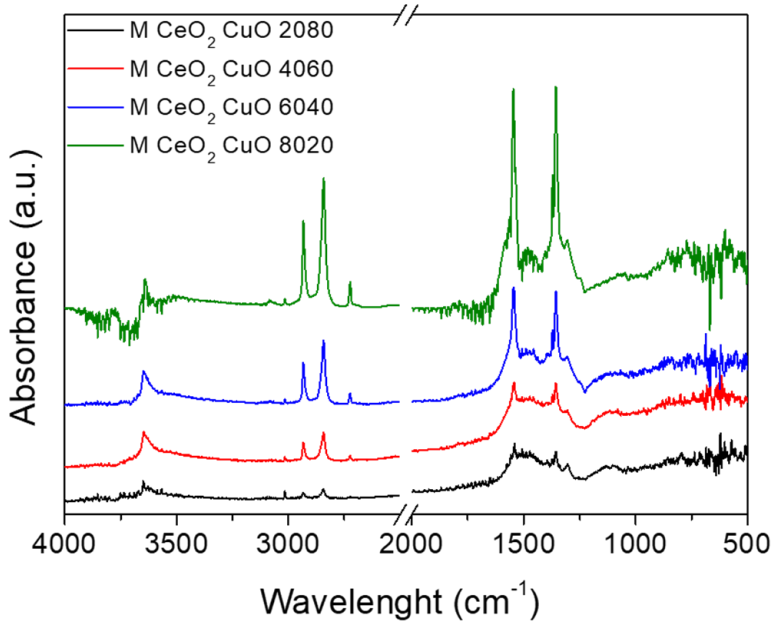


**Figure 20:** comparison of DRIFT spectra of the milled samples obtained by increasing $CeO_2$ content after 60 minutes of exposure to methane at 250°C.

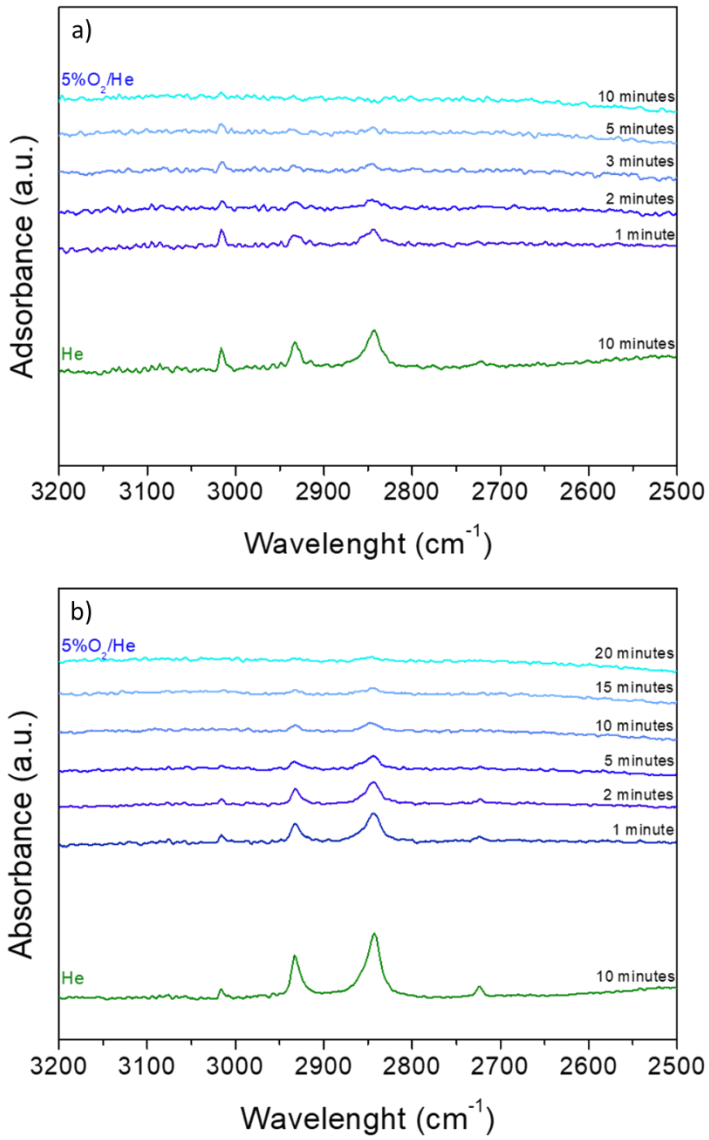


**Figure 21**: detailed representation of the experiment conducted, at the temperature of 250°C, on two M $CeO_2$ CuO samples synthesized with increasing $CeO_2$ contents (a) M $CeO_2$ CuO 2080; (b) M $CeO_2$ CuO 4060: exposure to pure He after exposure to 10%$CH_4$/He (green), 5%$O_2$/ He (shades of blue).

Figure 22 shows the desorption of the adsorbates in all milled samples with increasing $CeO_2$ content. We already observed in Figure 20 that the quantity of adsorbed species increases with the ceria content and that in the 2080 and 4060 samples a complete desorption was achieved in a relatively short time (Figure 21). In Figure 22 it is possible to observe that the desorption of the adsorbates occurs more slowly in the M $CeO_2$ CuO 6040 and M $CeO_2$ CuO 8020, in which it is possible to observe the presence of the peaks after 120 and 240 minutes respectively. It must be also noticed that in these samples, contrarily to the M $CeO_2$ CuO 2080 and M $CeO_2$ CuO 4060, the appearance of three peaks at 1030, 1228 and 1516 $cm^{-1}$ is detected. These peaks are likely due to the transformation of the adsorbed species into carbonates which are stable in the ceria surface, as it was observed in the pure ceria sample after exposure to 10%$CH_4$/5%$O_2$/He. This behavior

suggests that the increasing $CeO_2$ content reflects a more similar behavior compared to pure ceria, in which the adsorbates resulted stable during the exposure under oxidizing atmosphere.

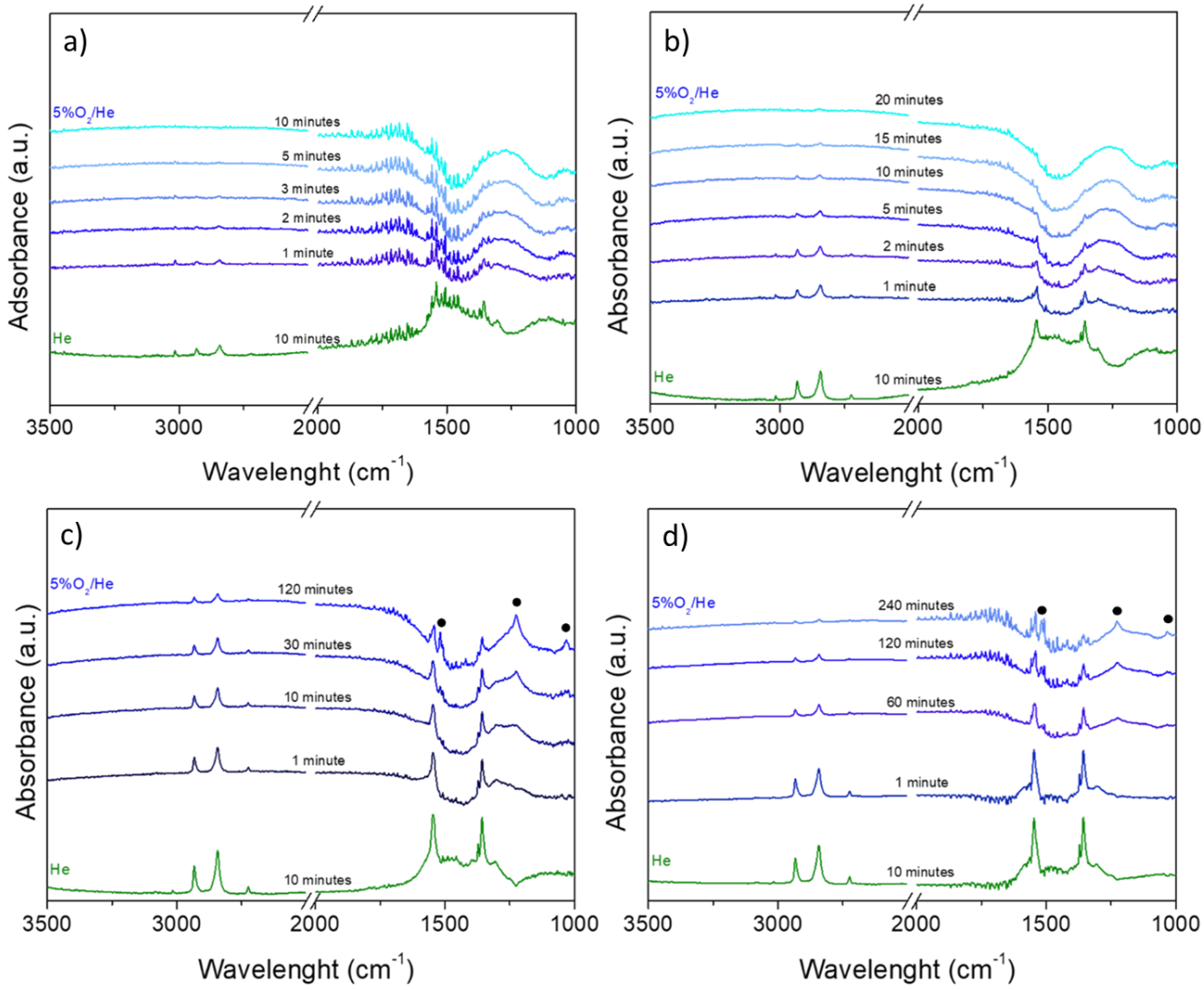


**Figure 22**: detailed representation of the desorption experiment conducted at 250°C on the a) M CuO $CeO_2$ 2080; b) M CuO $CeO_2$ 4060; c) M CuO $CeO_2$ 6040; d) M CuO $CeO_2$ 8020; sample synthesized with the commercial cerium oxide support: exposure pure He after exposure to methane (green), 5%$O_2$, He (shades of blue).

From these experiments it was possible to assume that there is an optimal composition for the production of partially oxidized products. A similar conclusion was reached by Senanajake et al, where they found that a maximum in the methanol production was obtained at a composition of 40%[17], expressed as a fraction of $Cu_2O$ covered by $CeO_2$. Regarding $CeO_2$ composites at higher loadings it is inferred that they could be more prone to deactivation because of the irreversible transformation of the partially oxidized species into stable carbonates.

Figure 23 summarizes the DRIFT results described so far. The M $CeO_2$ CuO catalysts demonstrated, contrarily to the single constituent components and the impregnated analogue, the ability to activate methane at 250°C. In particular, the adsorbed species observed trough the above mentioned experiments were the same observed in pure ceria after exposure to 10%$CH_4$/5%$O_2$/He mixture. Pure ceria did not show any adsorbates after exposure in 10%$CH_4$/He. Also the behavior of the adsorbates in 5%$O_2$/He was different in the two materials, since they demonstrated to be stable in pure ceria while they desorbed in the M $CeO_2$ CuO 2080 milled catalyst.

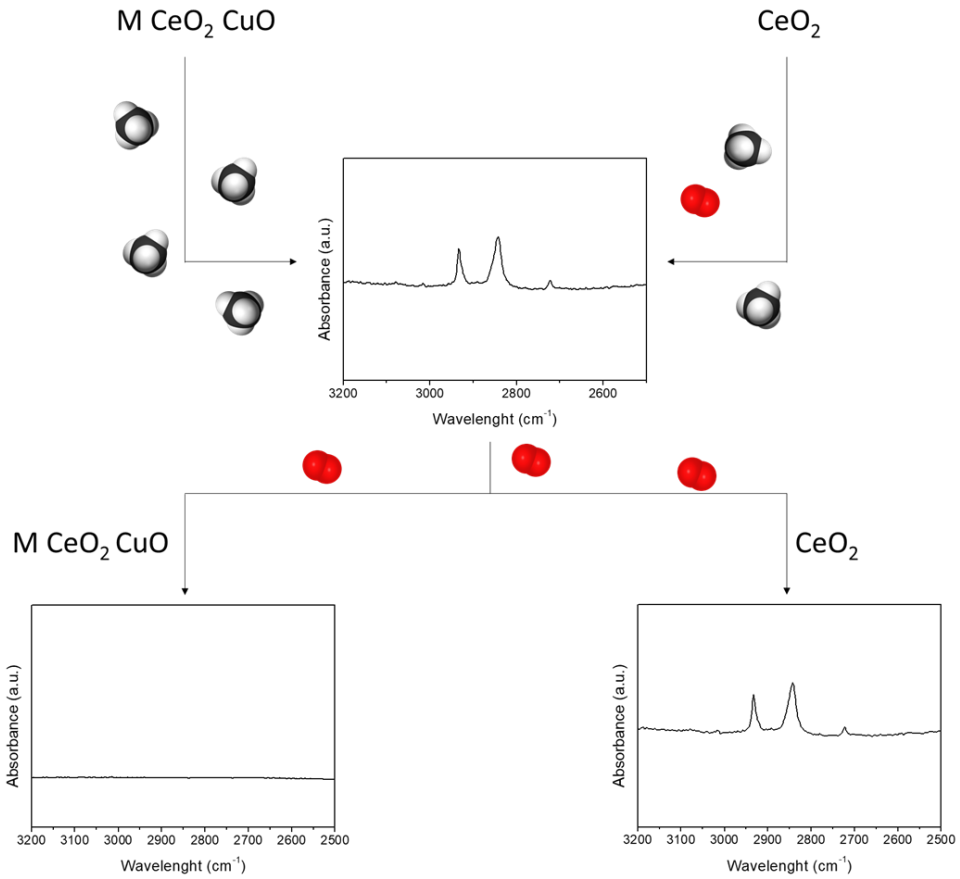


**Figure 23**: schematic representation of the comparison between the DRIFT results obtained from the experiments conducted on the pure cerium oxide and the milled M $CeO_2$ CuO composite. The 3200 – 2500 $cm^{-1}$ window is representative of the entire spectrum.

## 4.5. *in-operando* NEXAFS characterization

Figure 24 shows the Ce $M_5$ edge analysis of the pure $CeO_2$ and of the composite oxide M $CeO_2$ CuO 2080. The analysis of this edge easily allows to identify the presence of $Ce^{3+}$ and $Ce^{4+}$ sites, as we can observe in the bottom part of the figure, where references spectra of pure $CeO_2$ and $Ce_2O_3$ are reported. In particular, structures A and B are related to $Ce^{3+}$ while C and D to $Ce^{4+}$ [47–49]. In order to consider the different $CeO_2$ contents in the two experiments, the spectra were normalized to the C peak. This analysis allowed us to detect the presence of the $Ce^{3+}$ sites before (pure ceria) and after (composite oxide) the mechanochemical action provided by the mild energy ball milling synthetic technique. From Figure 25 it is possible to see in the spectra of pure ceria the presence of the A and B shoulders characteristics of the $Ce^{3+}$; their presence was expected and is related to the high surface area of the ceria sample utilized in the study (120$m^2$/g). In the composite material we observed a consistent reduction of the intensity of these two features, coherently with our expectations of a charge transfer between the $Ce^{3+}$ sites and $Cu^{2+}$ to form the redox couple $Cu^{+}/Ce^{4+}$.

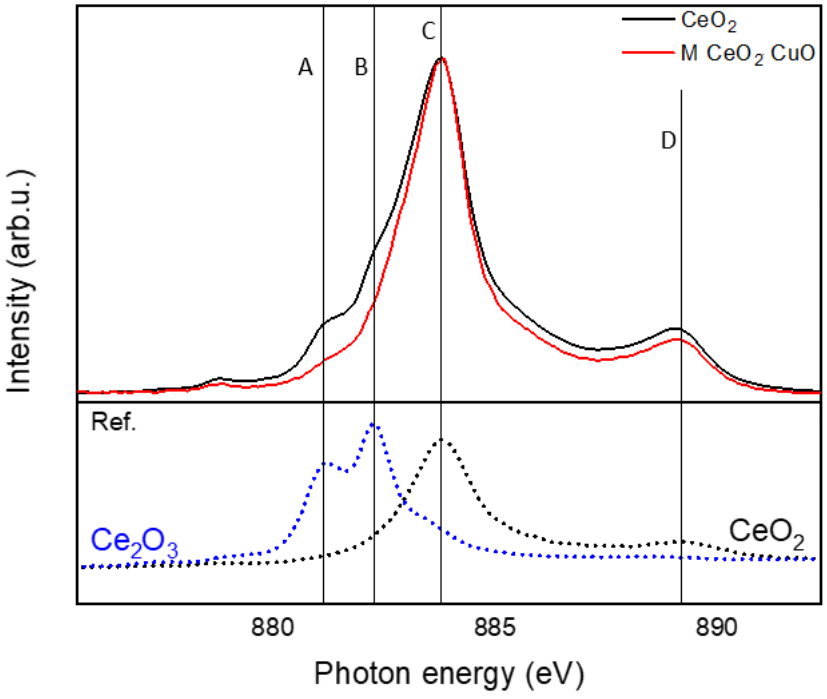


**Figure 24:** Top panel: Ce $M_5$ edge of the pure $CeO_2$ (black spectra) (prior to milling) and of the M $CeO_2$ CuO 2080 milled composite (red spectra) (after milling); bottom panel: references: $Ce_2O_3$ (blue dotted spectra) and $CeO_2$ (black dotted spectra), acquired on APE-HE beamline at RT.

Figure 25 shows the comparison between the cerium $M_5$ and $M_4$ edges and copper $L_3$ edge during the activation of the sample performed prior to the catalytic test. The activation consisted of a heating of the sample in He atmosphere from room temperature to 300°C. We can clearly see at 300°C the appearance of a peak at approximately 935 eV relative to the Cu(I) formation, while on the Ce $M_5$ edge it is possible to observe a small reduction in intensity of the A and B features related to the $Ce^{3+}$ sites. The parallel formation of $Cu^{+}$ and disappearance of $Ce^{3+}$ sites can be originated from a redox reaction between $Ce^{3+}$ sites and $Cu^{2+}$ to give $Ce^{4+}$ and $Cu^{+}$.

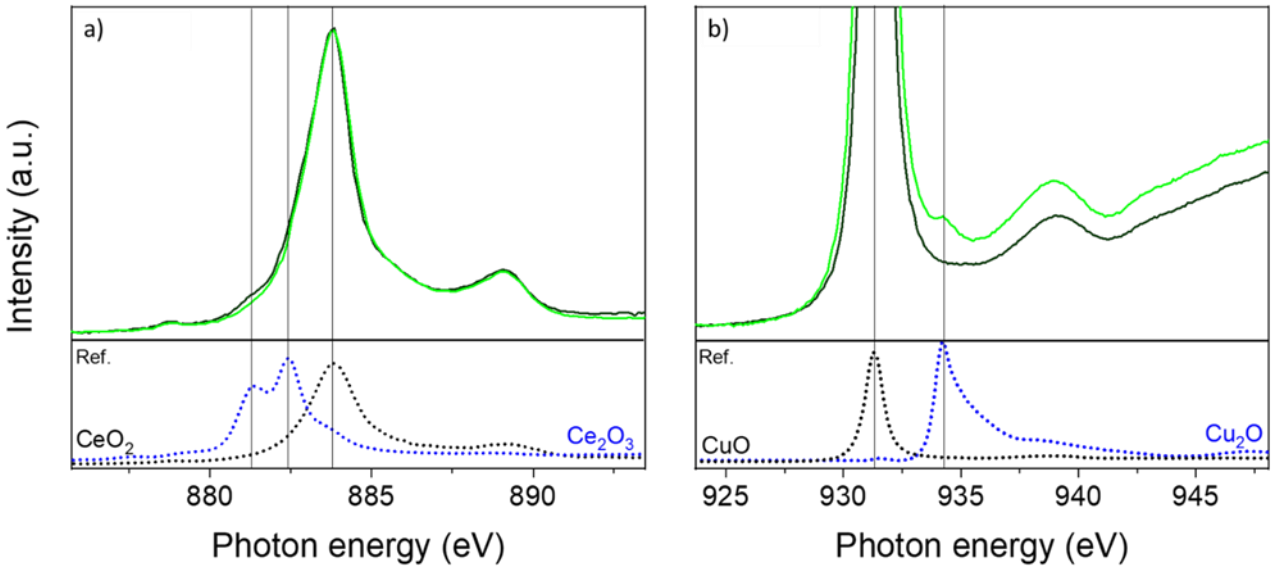


**Figure 25:** evolution of the Ce $M_5$ edge (a) and Cu $L_3$ edge (b) during the activation of the sample performed in pure He heating the sample from RT (black curve) to 300°C (green curve). The bottom panels of the figure report the reference spectra of $CeO_2$, $Ce_2O_3$, CuO and $Cu_2O$ acquired on the APE-HE beamline.

These two experiments confirmed that the predicted mechanochemical-induced reaction between the $Ce^{3+}$ and $Cu^{2+}$ effectively occurred since a major drop in intensity of the $Ce^{3+}$ features respect to the pure ceria was observed in the $M_5$ edge analysis soon after the milling process. Moreover, during the thermal treatment in He up to 300°C we observed a second slight decrease of the $Ce^{3+}$ together with the appearance of a structure attributed to $Cu^{+}$ in the copper $L_3$ edge[50] (see Figure 26).

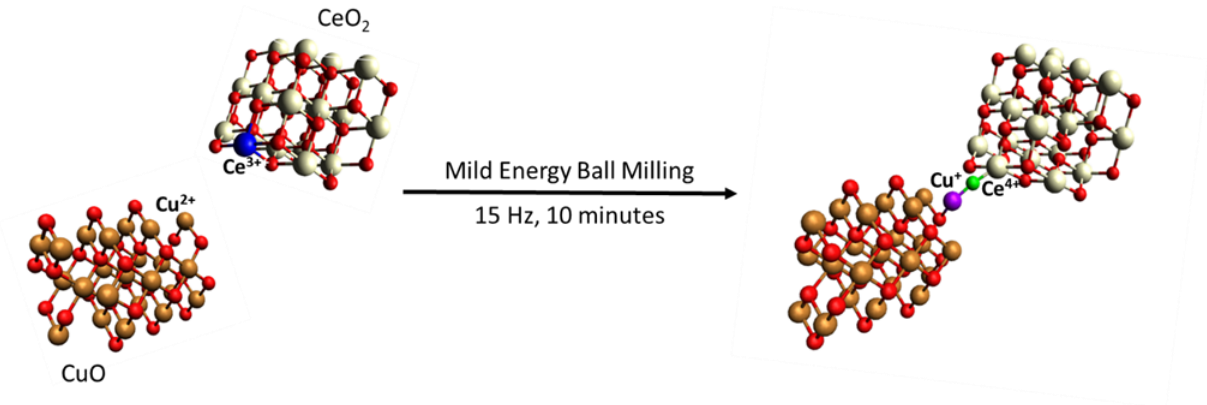


**Figure 26:** representative illustration of the mechanochemical-induced charge transfer between the $Cu^{2+}$ and $Ce^{3+}$ sites of the two oxides and formation of the interfacial $Cu^{+}$-O-$Ce^{4+}$ site.

After the activation we performed the same experimental procedure described in the DRIFT section, thus dropping the temperature to 250°C and treating the sample with a 10%$CH_4$/He mixture for 1 hour. Figure 27 shows the evolution of the copper $L_3$ edge during the exposure of the M $CeO_2$ CuO sample to the reactant atmosphere. As it is possible to see, a clear and consistent increase of the $Cu^{+}$ peak occurred simultaneously with the exposure to $CH_4$.

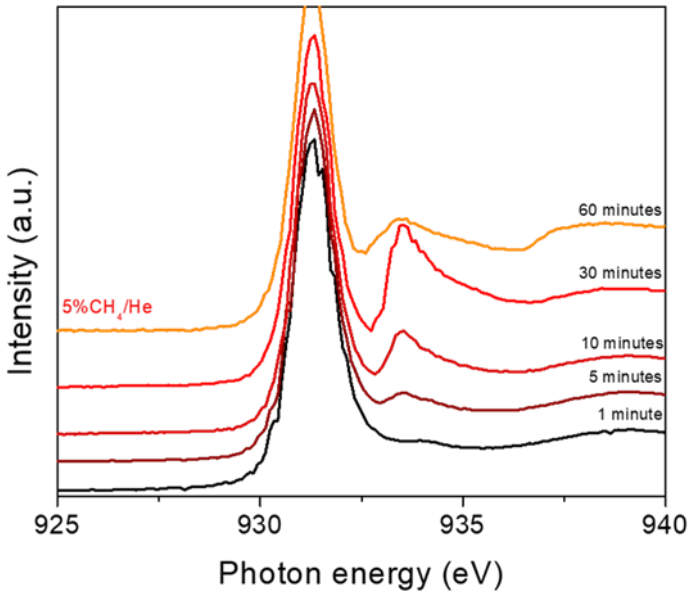


**Figure 27:** Cu $L_3$ absorption edge evolution over the M $CeO_2$ CuO 2080 sample during the exposure to 10% $CH_4$/He mixture at 250°C.

In Figure 28 a first comparison between *in-situ* DRIFT and *operando* NEXAFS analysis of the M $CeO_2$ CuO 2080 catalyst during the exposure to 10% $CH_4$/He mixture is reported. It is possible to see the simultaneous increase of the $Cu^{+}$ peak in the NEXAFS spectra together with the increase of the peaks related to the adsorbed species in the DRIFT spectra, indicating that the activation of methane and the subsequent

adsorption of species resulting from methane activation was related to the $Cu^{+}$ formation. This experiment also demonstrated the importance of the $Cu^{+}$-O-$Ce^{4+}$ site in the reactivity of the material.

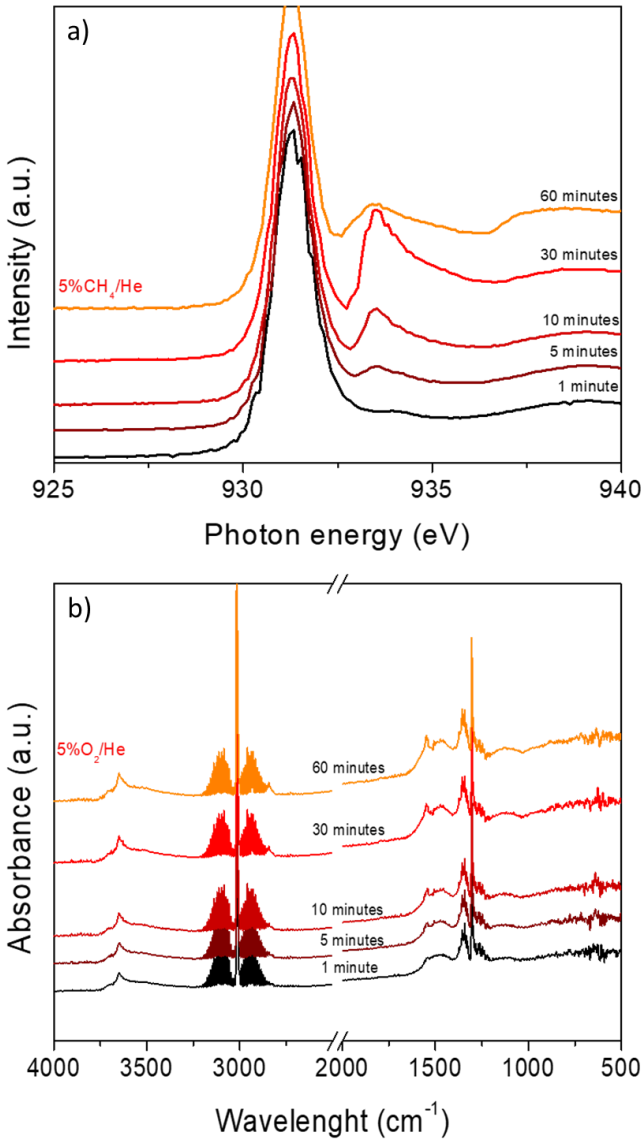


**Figure 28:** comparison between the in-operando NEXAFS (a) and in-situ DRIFT (b) results during the exposure of the M $CeO_2$ CuO 2080 catalyst. Both the experiments were conducted at 250°C.

We discussed in relation to Figure 17 that the presence of the peak at 3650 $cm^{-1}$ could have been ascribed to the formation of an OH group between a Ce and a Cu (we hypothesized a Cu-OH-Ce species) derived from the dissociative breaking of the C-H bond, forming an OH between the $Cu^{+}$ and a $Ce^{4+}$ and an adsorbed methoxy in the ceria surface. The result of this experiment supports that assumption showing the pivotal role of the $Cu^{+}/Ce^{4+}$ site in methane activation. Furthermore, the presence of a broad band between 3750 and 3250 $cm^{-1}$ may be related to the formation of water during the exposure of the material to the 10%$CH_4$/He atmosphere[46]. The gas chromatographic analysis of the products during the *in-operando* NEXAFS experiment (Figure 29b) showed a peak attributed to water approximately at a retention time of 32 seconds. Besides the

$H_2O$ peak we observed an increase in the formation of $CO_2$, likely due to the total oxidation of methane. It is not excluded a contribution due to the desorption of some carbonates present on the ceria surface since the $CO_2$ peak is present also when the sample was exposed to pure He prior to exposure to $CH_4$.

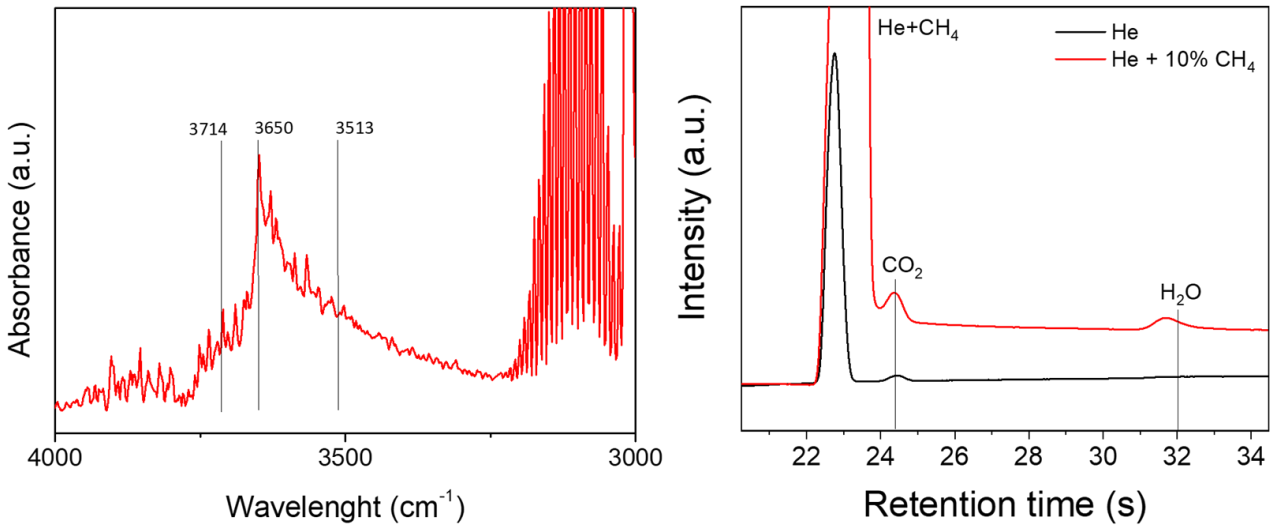


**Figure 29:** a) detail of the OH stretching zone of the DRIFT spectra of the M $CeO_2$ CuO 2080 after exposure of 60 minutes to 10%$CH_4$/He. b) gas chromatographic analysis of the *in-operando* NEXAFS experiment during exposure of the M $CeO_2$ CuO 2080 catalyst in pure He (black spectra) and 10%$CH_4$/He (red spectra)

Following the same experimental procedure reported for the DRIFT experiment, we then removed the 10%$CH_4$/He atmosphere in order to evaluate the stability of the $Cu^+$ peak and then we exposed the sample to 5%$O_2$/He. The results of the NEXAFS experiment are reported, together with the comparison with the DRIFT experiment, in Figure 30. We can see that the $Cu^+$ spectra remained unaltered when the methane flow was stopped and they remained stable for the time (10 minutes) in which the sample was exposed to the inert He atmosphere. The same stability was observed for the peaks related to the adsorbed methane. When the sample is exposed to 5%$O_2$/He, the $Cu^+$ peak disappears, which is consistent with the low stability of $Cu^+$ sites in oxidative atmosphere[51–54]. The comparison with the corresponding DRIFT results, depicted in Figure 30, shows that the disappearance of the $Cu^+$ peak is accompanied with the gradual desorption of the adsorbed species.

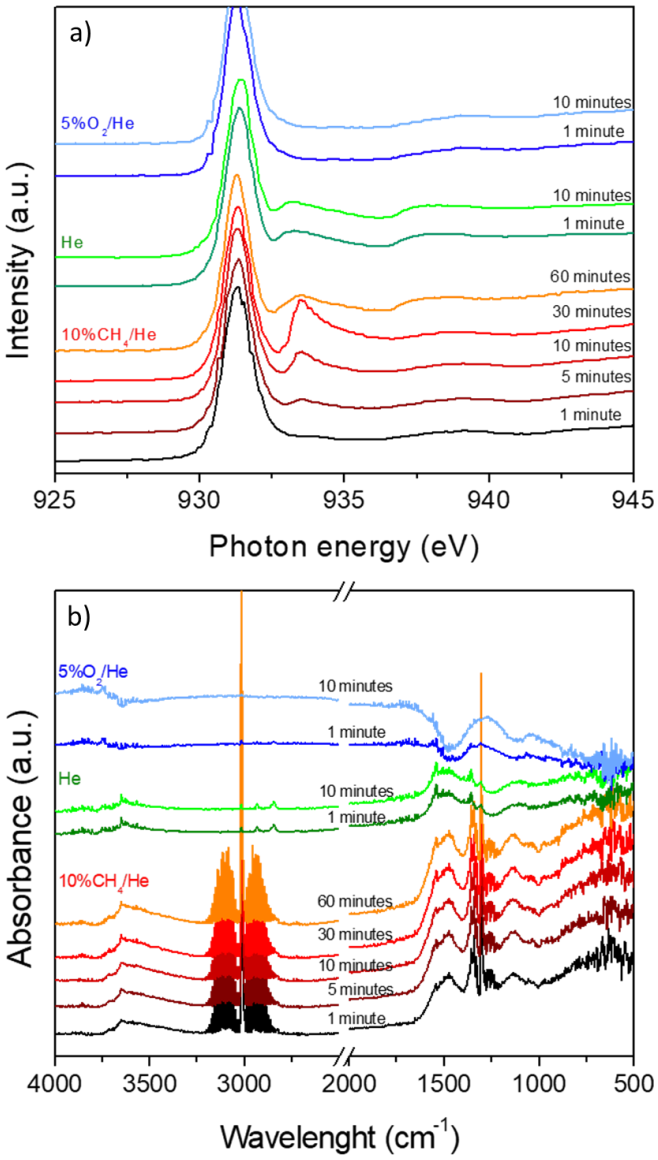


**Figure 30:** detailed representation of the results obtained with the operando NEXAFS (left panel) and DRIFT (right panel) spectroscopies performed over the M $CeO_2$ CuO 2080 sample: from the bottom to the top, 1°step: exposition to 10%$CH_4$/5%$O_2$/He mixture (red tones), 2° step: pure He (green tones), 3° step: 5%$O_2$/He (blue tones).

Concerning the Ce $M_{4,5}$ edge, reported in Figure 31, we did not observe any modifications during the various phases of the experiments.

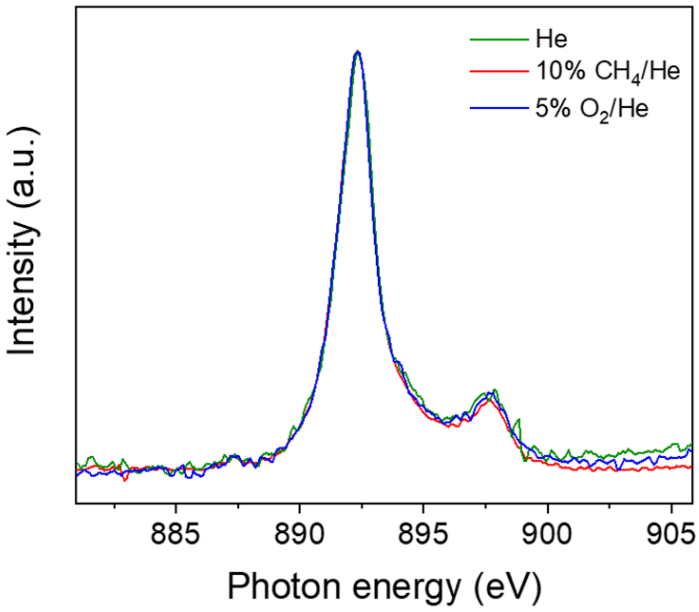


**Figure 31:** evolution of the Ce $M_5$ edge of the M $CeO_2$ CuO 2080 sample during the exposure to the different reactive mixtures at 250°C.

Contrarily to the model catalysts reported by Senanayake[17,55], we did not observe a reduction of $Ce^{4+}$ to $Ce^{3+}$ during the exposure to $CH_4$ at high temperatures. This difference could be explained by the difference in the preparation method and starting materials. Their model catalysts was prepared by depositing via PVD $CeO_2$ in a Cu(111) and after annealing at 327°C the $CeO_2/Cu_2O/Cu(111)$. In our case we supported $CeO_2$ in powder form over CuO. Moreover, we observed an increase in intensity of the $Cu^+$ peak during the exposure to 10% $CH_4$/He at 250°C. Since we observed the presence of $Cu^+$ sites in the as-prepared sample after thermal activation, it is possible to hypothesize a progressive reduction of the $Cu^{2+}$ sites near the starting $Cu^+$ sites.

Thanks to the micro-GC directly connected to the output of the reaction chamber of the operando NEXAFS reaction cell we were able to analyze the products of reaction during the exposure of the M $CeO_2$ CuO 2080 sample to the different atmospheres (Figure 32). It is possible to observe that during the sample exposition to the 5%$O_2$/He mixture, thus in combination with the desorption of the species detected with the DRIFT, the presence of traces of formaldehyde and methanol was clearly shown, together with the total oxidation products, $CO_2$ and $H_2O$ (not reported in this figure).

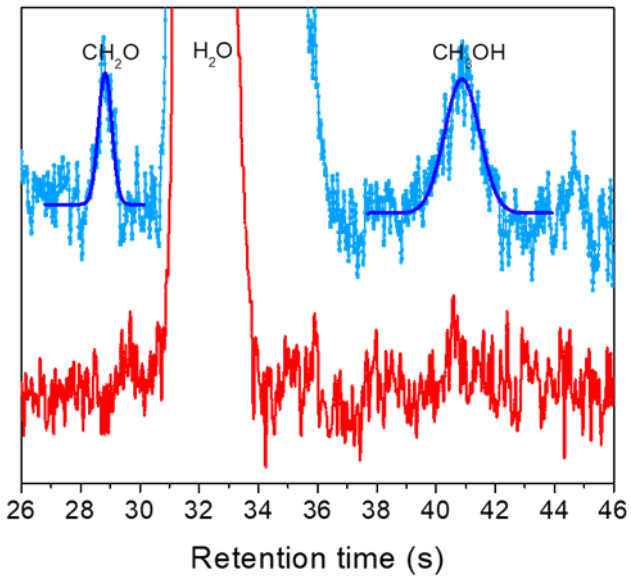


**Figure 32:** gas chromatograms acquired during the operando NEXAFS experiment on the M $CeO_2$ CuO 2080 sample after 30 minutes of exposition to 10%$CH_4$/He mixture (red) and after 5 minutes in 5%$O_2$/He atmosphere (blue).

Another interesting result was the reversible behavior the material showed when re-exposed to the 10%$CH_4$/He atmosphere. The $Cu^+$ peaks re-formed in the same way described in Figure 28 and then oxidized again to $Cu^{2+}$ when exposed to the 5% $O_2$/He mixture. This fully reversible behavior was observed for several $CH_4/O_2$ cycles as sumarized in the scheme of Figure 33.

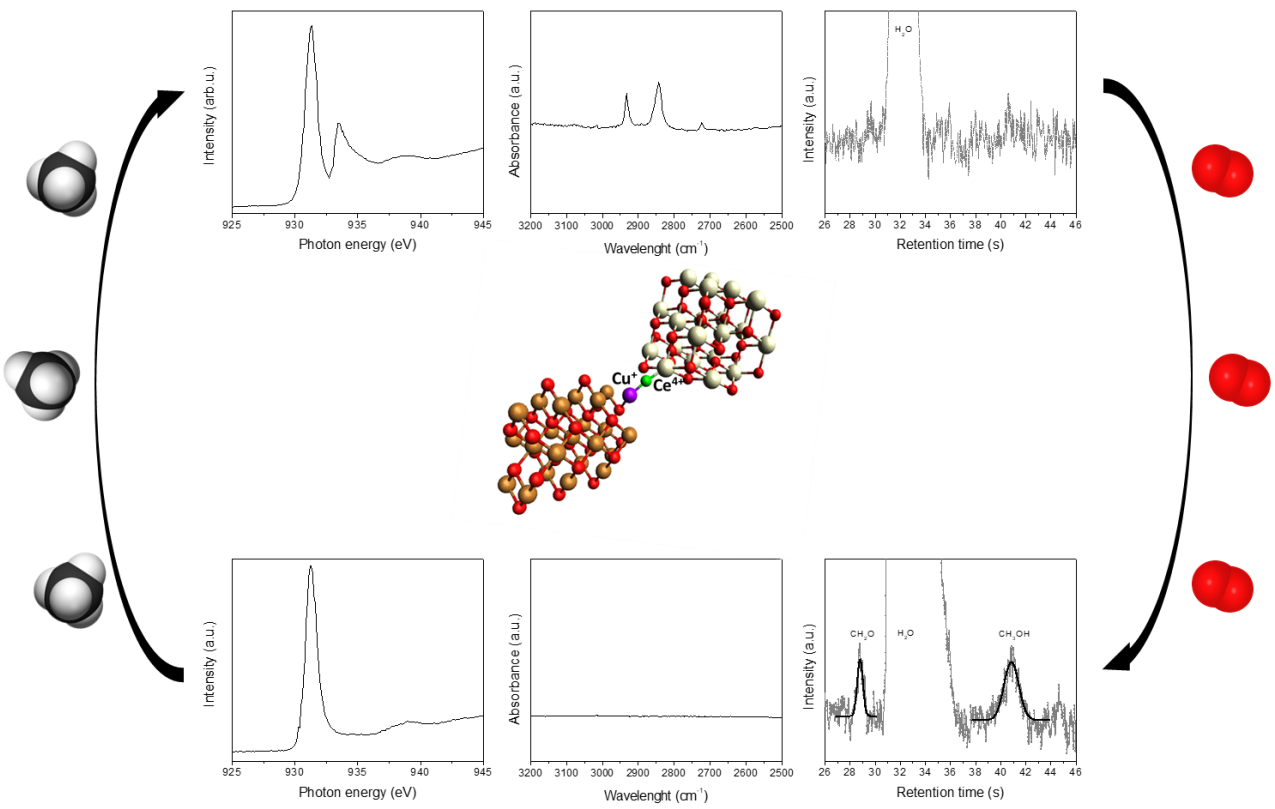


**Figure 33:** schematic representation of the reactivity of the M $CeO_2$ CuO catalyst towards 10%$CH_4$/He (left arrow) and 5%$O_2$/He (right arrow).

Overall, the multi-technique approach described in this section demonstrated to be a very useful and powerful tool to obtain important insights for the understanding of the behavior of the synthesized M $CeO_2$ CuO 2080.

# 4.6. Conclusions

A series of inverse $CeO_2$-CuO catalysts synthesized via mild energy ball milling technique and employed for methane activation is reported. In-situ DRIFT analysis demonstrated that the milled catalyst, contrarily to a reference impregnated sample, was able to activate methane at 250°C giving rise to the adsorption of the activated methane in the form of methoxy and formates, which are important intermediates for the production of methane partial oxidation products. The in-operando NEXAFS analysis conducted on the 20% $CeO_2$ CuO catalyst revealed the presence of a stable and reversible $Cu^{+}/Ce^{4+}$ redox couple responsible for the activation of the methane and the formation of traces of formaldehyde and methanol. The multi analytical approach used in this work has shown to give precious insights that can be useful for the development of materials based on the interaction between transition metal oxides and High Surface Area ceria and more in general for ceria based materials. We observed that the cerium oxide amount had an important effect on the desorption of the products. The low content ceria materials showed a faster desorption of the species contrarily to the ones with higher ceria contents. Parameters such as the time of exposure in methane atmosphere could be adjusted in order to favor the complete desorption of the adsorbed species in shorter times, which should favor the formation of methane partial oxidation products. The reversible redox behavior of these materials makes them interesting candidates also to chemical looping processes.

# 4.7. References


1. D. Gesser, H., R. Hunter, N. & B. Prakash, C. The direct conversion of methane to methanol by controlled oxidation. *Chem. Rev.* **85**, 235–244 (2002).

2. Zakaria, Z. & Kamarudin, S. K. Direct conversion technologies of methane to methanol : An overview. *Renew. Sustain. Energy Rev.* **65**, 250–261 (2016).

3. Latimer, A. A., Kakekhani, A., R. Kulkarni, A. & K. Nørskov, J. Direct Methane to Methanol: The Selectivity–Conversion Limit and Design Strategies. *ACS Catal.* **8**, 6894–6907 (2018).

4. Sharma, R., Poelman, H., Marin, G. B. & Galvita, V. V. Approaches for selective oxidation of methane to methanol. *Catalysts* **10**, (2020).

5. Brunetti, A., Migliori, M., Cozza, D., Catizzone, E., Giordano, G., Barbieri, G. Methanol Conversion to Dimethyl Ether in Catalytic Zeolite Membrane Reactors. *ACS Sustain. Chem. & Eng.* **8**, 10471–10479 (2020).

6. An, W., Chuang, K. T. & Sanger, A. R. *Dehydration of Methanol to Dimethyl Ether by Catalytic Distillation*. *The Canadian Journal of Chemical Engineering* vol. 82 (2004).

7. Wasmus, S. & Küver, A. Methanol oxidation and direct methanol fuel cells: a selective review. *J. Electroanal. Chem.* **461**, 14–31 (1999).

8. Garg, N., Sarkar, A. & Sundararaju, B. Recent developments on methanol as liquid organic hydrogen carrier in transfer hydrogenation reactions. *Coord. Chem. Rev.* **433**, 213728 (2021).

9. Ravi, M., Ranocchiari, M. & Van Bokhoven, J. A. The Direct Catalytic Oxidation of Methane to Methanol-A Critical Assessment. *Angew. Chemie - Int. Ed.* **56**, 6464–16483 (2017).

10. Osadchii, D.Y., I. Olivos-Suarez, A., Szécsényi, Á., Li, G., A. Nasalevich, M., A. Dugulan, I., Serra Crespo, P., J. M. Hensen, E., L. Veber, S., V. Fedin, M., Sankar, G. A., Pidko, E. & Gascon, J. Isolated Fe Sites in Metal Organic Frameworks Catalyze the Direct Conversion of Methane to Methanol. *ACS Catal.* **8**, 5542–5548 (2018).

11. Dinh, K.T., M. Sullivan, M., Serna, P., J. Meyer, R., Dincă, M., Román-Leshkov, Y. Viewpoint on the Partial Oxidation of Methane to Methanol Using Cu- and Fe-Exchanged Zeolites. *ACS Catal.* **8**, 8306–8313 (2018).

12. Szécsényi, Á., Khramenkova, E., Y. Chernyshov, I., Li, G., Gascon, J., A. Pidko, E. Breaking Linear Scaling Relationships with Secondary Interactions in Confined Space: A Case Study of Methane Oxidation by Fe/ZSM-5 Zeolite. *ACS Catal.* **9**, 9276–9284 (2019).

13. Grundner, S., Markovits, M.A.C., Li, G., Tromp, M., Pidko, E.A., Hensen, E.J.M., Jentys, A., Sanchez-Sanchez, M., Lercher, J. A. Single-site trinuclear copper oxygen clusters in mordenite for selective conversion of methane to methanol. *Nat. Commun.* (2015) doi:10.1038/ncomms8546.

14. I. Chan, S. & S.-F. Yu, S. Controlled Oxidation of Hydrocarbons by the Membrane-Bound Methane Monooxygenase: The Case for a Tricopper Cluster. *Acc. Chem. Res.* **41**, 969–979 (2008).

15. Culpepper, M. A. & Rosenzweig, A. C. Architecture and active site of particulate methane monooxygenase. *Crit. Rev. Biochem. Mol. Biol.* **47**, 483–492 (2012).

16. D. Senanayake, S., A. Rodriguez, J. & F. Weaver, J. Low Temperature Activation of Methane on Metal-Oxides and Complex Interfaces: Insights from Surface Science. *Acc. Chem. Res.* **53**, 1488–1497 (2020).

17. Zuo, Z., J. Ramírez, P., D. Senanayake, S., Liu, P. & A. Rodriguez, J. Low-Temperature Conversion of Methane to Methanol on CeOx/Cu2O Catalysts: Water Controlled Activation of the C–H Bond. *J. Am. Chem. Soc.* **138**, 13810–13813 (2016).

18. D. Senanayake, S., Stacchiola, D. & A. Rodriguez, J. Unique Properties of Ceria Nanoparticles Supported on Metals: Novel Inverse Ceria/Copper Catalysts for CO Oxidation and the Water-Gas Shift Reaction. *Acc. Chem. Res.* **46**, 1702–1711 (2013).

19. Gamarra, D., Belver, C., Fernández-García, M. & Martínez-Arias, A. Selective CO Oxidation in Excess H2 over Copper−Ceria Catalysts: Identification of Active Entities/Species. *J. Am. Chem. Soc.* **129**, 12064–12065 (2007).

20. Gunawardana, P. V. D. S., Lee, H. C. & Kim, D. H. Performance of copper–ceria catalysts for water gas shift reaction in medium temperature range. *Int. J. Hydrogen Energy* **34**, 1336–1341 (2009).

21. Konsolakis, M. Recent Advances on Nitrous Oxide (N2O) Decomposition over Non-Noble-Metal Oxide Catalysts: Catalytic Performance, Mechanistic Considerations, and Surface Chemistry Aspects. *ACS Catal.* **5**, 6397–6421 (2015).

22. Konsolakis, M. The role of Copper–Ceria interactions in catalysis science: Recent theoretical and experimental advances. *Appl. Catal. B Environ.* **198**, 49–66 (2016).

23. Cargnello, M., Fornasiero, P. & Gorte, R. J. Opportunities for tailoring catalytic properties through metal-support interactions. *Catal. Letters* **142**, 1043–1048 (2012).

24. Jenkins Ron, S. R. L. *X-Ray Powder Diffractometry*. (Wiley, 2012).

25. Mariño, F., Schönbrod, B., Moreno, M., Jobbágy, M., Baronetti, G., Laborde, M. CO preferential

oxidation over CuO–CeO2 catalysts synthesized by the urea thermal decomposition method. *Catal. Today* **133**–**135**, 735–742 (2008).

26. MacIel, C. G., Silva, T. D. F., Hirooka, M. I., Belgacem, M. N. & Assaf, J. M. Effect of nature of ceria support in CuO/CeO2 catalyst for PROX-CO reaction. *Fuel* **97**, 245–252 (2012).

27. Avgouropoulos, G. & Ioannides, T. Effect of synthesis parameters on catalytic properties of CuO-CeO2. *Appl. Catal. B Environ.* **67**, 1–11 (2006).

28. Yin, Y., Liu, K., Gao, M., Zhang, L., Su, H., Zeng, S. Influence of the structure and morphology of CuO supports on the amount and properties of copper–cerium interfacial sites in inverse CeO2/CuO catalysts. *J. Mol. Catal. A Chem.* **404**–**405**, 193–203 (2015).

29. Avgouropoulos, G., Ioannides, T. & Matralis, H. Influence of the preparation method on the performance of CuO–CeO2 catalysts for the selective oxidation of CO. *Appl. Catal. B Environ.* **56**, 87–93 (2005).

30. Zhou, K., Xu, R., Sun, X., Chen, H., Tian, Q., Shen, D., Li, Y. Favorable synergetic effects between CuO and the reactive planes of ceria nanorods. *Catal. Letters* **101**, 169–173 (2005).

31. Beckers, J. & Rothenberg, G. Redox properties of doped and supported copper-ceria catalysts. *Dalt. Trans.* 6573–6578 (2008) doi:10.1039/b809769k.

32. Giordano, F., Trovarelli, A., De Leitenburg, C. & Giona, M. A Model for the Temperature-Programmed Reduction of Low and High Surface Area Ceria. *J. Catal.* **193**, 273–282 (2000).

33. Zeng, Y., Haw, K.G., Wang, Z., Wang, Y., Zhang, S., Hongmanorom, P., Zhong, Q., Kawi, S. Double redox process to synthesize CuO–CeO2 catalysts with strong Cu–Ce interaction for efficient toluene oxidation. *J. Hazard. Mater.* **404**, 124088 (2021).

34. Djinović, P., Batista, J. & Pintar, A. Calcination temperature and CuO loading dependence on CuO-CeO2 catalyst activity for water-gas shift reaction. *Appl. Catal. A Gen.* **347**, 23–33 (2008).

35. Zeng, S., Wang, Y., Ding, S., Sattler, J.H.B., Borodina, E., Zhang, L., Weckhuysen, B.M., Su, H. Active sites over CuO/CeO2 and inverse CeO2/CuO catalysts for preferential CO oxidation. *J. Power Sources* **256**, 301–311 (2014).

36. Zeng, S., Zhang, W., Śliwa, M. & Su, H. Comparative study of CeO2/CuO and CuO/CeO2 catalysts on catalytic performance for preferential CO oxidation. *Int. J. Hydrogen Energy* **38**, 3597–3605 (2013).

37. Otsuka, K., Wang, Y., Sunada, E. & Yamanaka, I. Direct partial oxidation of methane to synthesis gas by cerium oxide. *J. Catal.* **175**, 152–160 (1998).

38. Warren, K. J. & Scheffe, J. R. Kinetic insights into the reduction of ceria facilitated via the partial oxidation of methane. *Mater. Today Energy* **9**, 39–48 (2018).

39. Chrzan, M., Chlebda, D., Jodłowski, P., Salomon, E., Kołodziej, A., Gancarczyk, A., Sitarz, M., Łojewska, J. Towards Methane Combustion Mechanism on Metal Oxides Supported Catalysts: Ceria Supported Palladium Catalysts. *Top. Catal.* **62**, 403–412 (2019).

40. Li, C., Domen, K., Maruya, K. ichi & Onishi, T. Spectroscopic identification of adsorbed species derived from adsorption and decomposition of formic acid, methanol, and formaldehyde on cerium oxide. *J. Catal.* **125**, 445–455 (1990).

41. G. Lustemberg, P., V. Bosco, M., Bonivardi, A., F. Busnengo, H. & V. Ganduglia-Pirovano, M. Insights into the Nature of Formate Species in the Decomposition and Reaction of Methanol over Cerium Oxide Surfaces: A Combined Infrared Spectroscopy and Density Functional Theory Study. *J. Phys. Chem. C* **119**, 21452–21464 (2015).

42. Li, C., Sakata, Y., Arai, T., Domen, K., Maruya, K.-I., Onishi, T. Adsorption of Carbon Monoxide and Carbon Dioxide on Cerium Oxide studied by Fourier-transform Infrared Spectroscopy Part 2.-Formation of Formate Species on Partially Reduced CeO, at Room Temperature. *J. Chem. Soc., Faraday Trans. I* **85**, 1451–1461 (1989).

43. Yoshikawa, K., Sato, H., Kaneeda, M. & Kondo, J. N. Synthesis and analysis of CO2 adsorbents based on cerium oxide. *J. CO2 Util.* **8**, 34–38 (2014).

44. Binet, C., Daturi, M. & Lavalley, J. C. IR study of polycrystalline ceria properties in oxidised and reduced states. *Catal. Today* **50**, 207–225 (1999).

45. Badri, A., Binet, C. & Lavalley, J.-C. An FTIR study of surface ceria hydroxy groups during a redox process with H2. *J. Chem. Soc., Faraday Trans. I* **92**, 4669–4673 (1996).

46. M. Natile, M., Boccaletti, G. & Glisenti, A. Properties and Reactivity of Nanostructured CeO2 Powders: Comparison among Two Synthesis Procedures. *Chem. Mater.* **17**, 6272–6286 (2005).

47. Hayakawa, T., Arakawa, M., Sarugaku, S., Kota, A., Kenichirou, T., Kiyomura, Y., Kawano, T., A. T. Characterization of Cerium and Oxygen Atoms in Free Clusters of Cerium Oxide by X-ray Absorption Spectroscopy. *Top. Catal.* **61**, 119–125 (2018).

48. Turner, S., Lazar, S., Freitag, B., Egoavil, R., Verbeeck, J., Put, S., Strauven, Y., Van Tendeloo, G. High resolution mapping of surface reduction in ceria nanoparticles. *Nanoscale* **3**, 3385–3390 (2011).

49. Yagci, O. The M4,5 photo-absorption spectra of cerium in CeO2 and oxidation of metallic cerium. *J. Phys. C Solid State Phys.* **19**, 3487–3495 (1986).

50. Gurevich, A. B., Bent, B. E., Teplyakov, A. V. & Chen, J. G. A NEXAFS investigation of the formation and decomposition of CuO and Cu2O thin films on Cu(100). *Surf. Sci.* **442**, L971–L976 (1999).

51. Tahir, D. & Tougaard, S. Electronic and optical properties of Cu, CuO and Cu 2O studied by electron spectroscopy. *J. Phys. Condens. Matter* **24**, (2012).

52. Poulston, S., Parlett, P. M. & Stone, P. Surface Oxidation and Reduction of CuO and CuzO Studied Using XPS and XAES. *Surf. Interface Anal.* **24**, 811–820 (1996).

53. Spitzer, A. & Lüth, H. The adsorption of oxygen on copper surfaces: II. Cu(111). *Surf. Sci.* **118**, 136–144 (1982).

54. Rodriguez, J. J., Kim, J. Y., Hanson, J. C., Pe´rezpe´rez, M. & Frenkel, A. I. Reduction of CuO in H 2 : in situ time-resolved XRD studies. *Catal. Letters* **85**, 247–254 (2003).

55. Liu, Z., Huang, E., Orozco, I., Liao, W., Palomino, R.M., Rui, N., Nem, S., Grinter, D.C., Mahapatra, M., Liu, P. Water-promoted interfacial pathways in methane oxidation to methanol on a CeO 2 -Cu 2 O catalyst. *Science (80-. ).* **517**, 513–517 (2020).

# 5. Conclusions and Future Perspectives

The motivation for this PhD dissertation stemmed from the significant results previously obtained in our laboratory for the methane oxidation when $Pd/CeO_2$ catalysts were made by Mild-Energy Ball Milling. This is a new synthesis method to prepare metal supported catalysts, which simultaneously reduces solvent, energy and time consumption and can lead to outstanding performance improvements compared to conventional impregnation techniques.

We adopted this approach to prepare two catalytic systems based on high surface area cerium oxide and cheap, non-precious transition metals. The catalysts investigated were $Ni/CeO_2$ and an inverse $CeO_2/CuO$. and they were studied in methane activation reactions (dry-reforming and partial oxidation) with the aim to understand the role of milling in promoting the catalytic activity.

The main results are summarized below:

Two series of $Ni/CeO_2$ were obtained from two inexpensive and commercially available Nickel hydrated salts, by varying the milling time. For comparison each series included also a reference catalyst prepared via Incipient wetness Impregnation. The nitrate precursors resulted in a better distribution of the active phase on the support, which enabled enhanced catalytic performance regardless of the preparation method. Both milled-catalysts series were tested under DRM conditions and resulted more active than the impregnated catalysts. The best catalytic performance, in terms of activity and stability, was obtained for a short or medium period of milling (10-20 min), while catalysts milled for longer times showed a minor catalytic activity. In the samples milled for short time, HRTEM and XPS analyses revealed the presence of a peculiar $Ni_xCeO_{2-x}$ phase characterized by a cerium in a different oxidized valence state compared to the usual (4+) encountered in the $CeO_2$ and the incorporation of reduced Ni atoms in the defective sites of the support, i.e. oxygen vacancies. These Ni, O, Ce arrangements were located very much on the surface and are probably due to the soft shear-stresses provided by the gentle milling action of this synthesis approach.

Therefore, we may conclude that ball milling energy implied in this method of preparation was able to promote a particular electronic interaction between metal and support associated with a surface structural arrangement of cerium oxide, which enhanced the catalytic performances. These mechanochemical-induced modifications revealed to be localized on the surface when low-medium milling times of 10-20 minutes were used, while a prolonged milling time cause the incorporation of this phase into the crystallite bulk, thus compromising catalytic activity. The results are in agreement with those previously obtained for the $Pd/CeO_2$ and $Pd\text{-}Pt/CeO_2$ systems.

Encouraging results also emerged from the adoption of this synthesis method for the preparation of inverse catalysts, in which high-surface cerium oxide was supported on copper oxide. Several inverse catalysts were synthesized increasing the ceria content from 20% to 80% by weight, with a milling time of 10 minutes. These milled composites, contrarily to a reference impregnated catalyst and to the alone CuO and $CeO_2$, demonstrated to activate methane at the relatively low temperature of 250°C. A detailed spectroscopic characterization, obtained by coupling *in-situ* DRIFT and *in-operando* NEXAFS revealed the presence of the $Cu^{+}/Ce^{4+}$ redox couple that demonstrated to have a pivotal role in the activation of methane to produce, under oxidizing conditions, not only CO and $CO_2$ but also traces of other oxygenate products (formaldehyde and methanol). The formation of these sites is due to mechanochemical-induced charge transfer between the $Ce^{3+}$ sites of the supported oxide and the $Cu^{2+}$ sites of the support. They were observed previously in a model $CeO_2/Cu_2O/Cu(111)$ catalyst prepared *via* Physical Vapor Deposition synthesis, and this study demonstrated the chance to obtain similar results with a rapid, solventless and more industrially favorable synthesis. It was also proved that a thoughtful use of advanced *in-situ* and *in-operando* spectroscopic techniques is important for the deep understanding of the interaction occurring at the nanoscale of catalytic materials, even at the preliminary stages of the catalyst design.

From these and our previous results it is possible to conclude that medium-energy ball milling is a valid approach for changing the energy state of active sites in the first surface/interface layers of ceria-based catalysts and could be an easy way to design new catalysts. The observation in both the studied systems that the mechanical energy involved in the process can induce charge transfer between the defective sites of cerium oxide and the involved transition- metal atoms represents an important outcome. It is conceivable to lever the reactive surface $Ce^{3+}$ sites as “reducing agents” for other metal cations giving rise to the formation of interfacial sites which could possess unusual catalytic activities and selectivity. This would pave the way for the design of a wide class of ceria-based composites with metal oxides, ranging from simple transition metal oxides to more complex oxides such as perovskites or spinels, which possess different metal cations with different valence states.

The main disadvantage of synthesizing catalysts with medium-energy ball milling is the stochastic nature of the results. With this dissertation, we have elucidated some of the processes that can take place during milling, thus taking a step forward in understanding the parameters that can influence the final properties of catalysts and in helping the scale up of this innovative synthesis on an industrial scale.

In near future, it will be interesting to unveil the role of other variables in this kind of synthesis such as the effect of precursors’ crystalline water. It will also be interesting to develop some bi-metallic formulation, e.g. Ni-Co or Ni-Cu, which could further enhance the stability of Ni based catalysts or test the system $CeO_2$-CuO

in the hydrogenation of $CO_2$. Moreover, considering there is a direct correlation between surface area and $Ce^{3+}$ sites, it will be important to optimize the synthetic procedure described in chapter 2.1.1. to have a accurate control of surface defects by, for instance, preparing ceria-based solid solutions.